FACULTY OF MATHEMATICS AND PHYSICS
Charles University

DOCTORAL THESIS

Helena Cibulková

Distribution functions of asteroid physical properties

Astronomical Institute of Charles University

Supervisor of the doctoral thesis: Mgr. Josef Ďurech, Ph.D.

Study programme: Physics

Study branch: Theoretical physics, astronomy and astrophysics

Prague 2017

I declare that I carried out this doctoral thesis independently, and only with the cited sources, literature and other professional sources.

I understand that my work relates to the rights and obligations under the Act No. 121/2000 Sb., the Copyright Act, as amended, in particular the fact that the Charles University has the right to conclude a license agreement on the use of this work as a school work pursuant to Section 60 subsection 1 of the Copyright Act.

In Prague July 11, 2017   ....

Title: Distribution functions of asteroid physical properties

Author: Helena Cibulková

Institute: Astronomical Institute of Charles University

Supervisor: Mgr. Josef Ďurech, Ph.D., Astronomical Institute of Charles University

Abstract: In this thesis, I utilize photometric data sparse in time produced by all-sky surveys and investigate physical properties of large asteroid populations. In principle, the individual approach to asteroid modeling cannot compass all objects because new asteroids are continually discovered and we do not have enough data for them. Therefore, in this work I present an essentially different, statistical approach. In a series of papers, we developed two independent methods which use a triaxial-ellipsoid approximation, and we test their applicability and limits. We prove they can be used to the photometric databases like Lowell Observatory database or Pan-STARRS. The output quantities are distributions of the spin axis directions and shape elongations for asteroid populations, and using the Kolmogorov-Smirnov test we search for differences among them. The main result of my work is that the distribution of ecliptical longitudes of spin axes is nonuniform. Moreover, this nonuniformity is more significant for asteroids with low orbital inclinations and the distribution is dependent on the shape elongation. We ran a number of simulations and tests, but we did not find a clear explanation of this enigmatic result. We found that small asteroids ($D < 25\,\mathrm{km}$) are on average more elongated than large ones. We also constructed distributions for 13 main-belt families; as to the distributions of spin axes latitudes, we found that Gefion family is significantly different from its background and when studying distributions of elongations, we found that Massalia and Phocaea have more elongated members than corresponding backgrounds.

Keywords: asteroids; sparse photometry; distributions; statistics

Contents

Preface

Our knowledge of asteroids improved significantly during the last ∼15 years thanks to the growing amount of data from space satellites and ground-based telescopes and development of new techniques to utilize them. The physical properties of asteroids such as rotational states, shapes and sizes are generally important for our understanding of the collisional history of the Solar System, since they evolved during the evolution of the main asteroid belt due to the non-gravitational forces and the mutual collisions between asteroids.

A rich source of information about asteroid physical properties is photometry. The amount of photometric data of asteroids has been growing rapidly in recent years mainly thanks to the all-sky surveys such as Catalina (Drake et al., 2012), Panoramic Survey Telescope & Rapid Response System (Pan-STARRS) (Hodapp et al., 2004; Tonry et al., 2012) or Lowell Observatory Near-Earth Object Search (LONEOS) (Bowell et al., 1995). The brightness of an asteroid as a function of time is called the lightcurve. Typically, if the lightcurve is dense enough, i.e., contains enough measurements during the time interval comparable with the asteroid rotational period, it is used for the determination of the convex shape and rotational state using the lightcurve inversion method (Kaasalainen and Torppa, 2001; Kaasalainen et al., 2001). Data from sky surveys are, however, sparse in time and their systematic uncertainty is often worse than ∼0.1 mag, which usually makes impossible to find a unique rotational period of an asteroid.

One of the goals of this work is to fully utilize sparse photometry for the determination of distribution functions of asteroid spin axis orientations and shape elongations and to develop a reliable method applicable on the more accurate photometric data that shall be provided in the future by the Large Synoptic Survey Telescope (LSST) (Callahan et al., 2016). We were inspired by the work of Bowell et al. (2014), who first found the nonuniform distribution of spin axes longitudes when analyzing the photometric data from the Lowell Observatory database. However, they were not able to find any explanation for such result, which motivated us to study this problem in detail.

The backbone of this thesis is the paper Cibulková et al. (2016), where we developed a new method that provides pole positions and shape elongations of asteroids. The paper is included after the List of papers and is labeled as Paper 2. We model asteroids as geometrically scattering triaxial ellipsoids. The model compares observed values of mean brightness and the dispersion of brightness with computed values obtained from the parameters of the model: ecliptical longitude λ and latitude β of the pole and the ratios a/b, b/c of axes of the ellipsoid. These parameters are optimized to get the best agreement with the observation. The model is described in Chapter 3, where we also test its reliability on synthetic data and then we apply our model to photometric data from Lowell Observatory database, analyze the results and compare distributions of model parameters for various asteroid populations, such as asteroid families, taxonomic classes or asteroids located in different parts of the main belt. Our motivation is to find if these groups, different within one classification, will have also different distributions of our studied parameters.

A different approach was used in the papers Nortunen et al. (2017) and Cibulková et al. (2017). In the former, we mainly studied the validity and accuracy of the method, that is based on the inversion of distribution functions, and practical applicability on astronomical databases; in the latter, we applied the model to photometric data from Pan-STARRS1 survey and performed an analysis focusing on various asteroid populations. This is the content of Chapter 4, where we also compare results with those from Chapter 3. The advantage of this method is that it can be used even if only a few points and one apparition are available for an asteroid.

The main results of this thesis are summarized in Conclusions. One of the benefits of this work is that our results can be used in other investigations of asteroid populations, e.g., to constrain theoretical evolution models of asteroid families or for an independent comparison of distributions of spin axes and shapes. That was done in the paper Hanuš et al. (2017a), where 16 new shape models of the members of Eos family were derived. In total, they showed spin directions of 56 Eos members and compared them with our distributions of spin longitudes and latitudes for Eos family. Both results were in the mutual agreement.

Finally, after the List of papers, we included the paper Cibulková et al. (2014) (labeled as Paper 1) that deals with the long-term collisional evolution of the main belt. This issue is naturally connected with the main topic of this thesis, since all asteroids have been influenced by mutual collisions (catastrophic or cratering events) that changed the orientation of their spin axes and also their sizes and shapes. In this paper, we divided the whole main belt into six parts since we realized they have different size-frequency distributions, collision probabilities and impact velocities. To simulate the mutual collisions of asteroids, we used a modified version of the Boulder code (Morbidelli et al., 2009). We accounted also for the material characteristics by creating two models, one for monolithic objects and one for rubble-pile bodies. We found that for the monoliths, the match between observational data (we compared the size-frequency distributions and number of asteroid families in individual parts of the main belt) and the results of our simulations is significantly better than for the rubble-piles. This work was not one of the main topics of this thesis and thus it is included in the form of attached paper.

During my investigation, I collaborated also with colleagues whose contributions have to be mentioned. The author of the mathematical background of both photometric models is Mikko Kaasalainen; the code used in Chapter 4 was written by Hari Nortunen; the photometric data from the Lowell Observatory were provided by Dagmara Oszkiewicz; and the data from Pan-STARRS1 survey were provided by Peter Vereš.

1. Introduction

Small Solar System Bodies are the most numerous group of objects in our Solar System that compasses asteroids, centaurs, Neptune trojans, transneptunian objects and comets. In this work, we focus on asteroids, specifically main-belt asteroids (MBAs) located between the secular resonance ν_6 with Saturn and the 2:1 mean motion resonance with Jupiter. The largest body in the main belt, (1) Ceres, with a diameter $\sim$850 km, belongs to the dwarf planets since 2006, together with Pluto and some other objects. Nevertheless, as a rule we do not exclude Ceres from our sample.

1.1 Main belt

In the main belt, we can notice several prominent gaps at certain semimajor axes. They were discovered in 1866 by Daniel Kirkwood and are called Kirkwood gaps. They are located at those semimajor axes where the mean motion of an asteroid and the mean motion of Jupiter are related by a ratio of two small integers. Positions of some strongest low-order resonances are shown in Fig. 1.1. The mechanism that can deliver asteroids with diameter $D < 20$ km in the main belt to resonance is the Yarkovsky drift (e.g., Bottke et al., 2002) – a non-gravitational force caused by the anisotropic emission of thermal photons from a rotating body. The most powerful resonances that cause a large increase of the asteroid eccentricity and consecutive transport of bodies (with a contribution of close encounters)
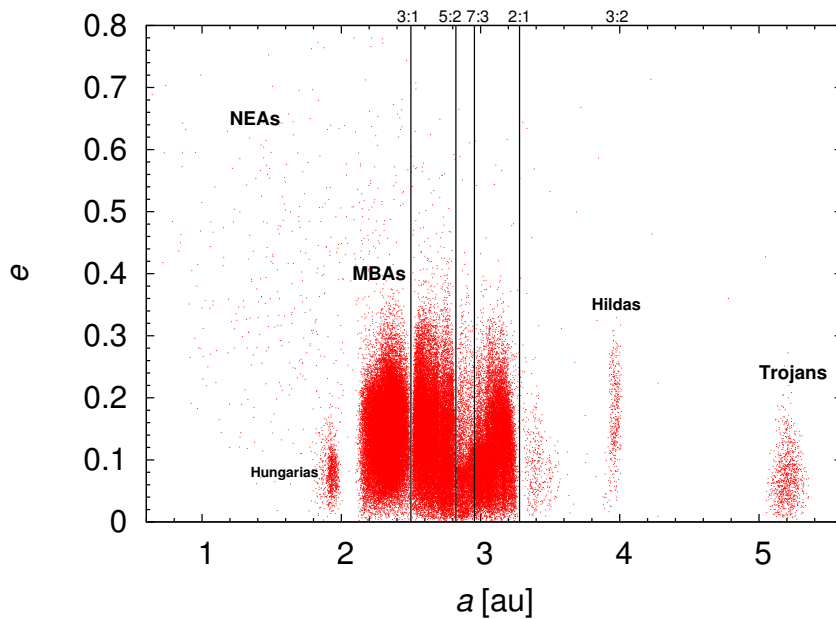

Figure 1.1: Osculating orbits of 100,000 asteroids in the plane of semimajor axes a and eccentricity e. Data were taken from the Asteroid Orbital Elements Database updated on March 21, 2017.

to Mars-, Earth-, and Venus-crossing orbits are ν_6 secular resonance[1], 3:1 and 5:2 mean motion resonances (MMRs) with Jupiter (e.g., Morbidelli et al., 2002). The situation in the 2:1 MMR is more complicated. The dynamical lifetime in the center of the resonance is comparable to the age of the Solar System, while the regions close to the borders of the resonance are unstable, but it still takes several million years to achieve the Earth-crossing orbit (Moons et al., 1998). Such behaviour is caused by the three-body resonances (between an asteroid and two planets, mainly Jupiter and Saturn, Nesvorný and Morbidelli, 1998) that force asteroids to have strongly chaotic orbits but stable on long time intervals (Milani et al., 1997). The example of a stable resonance is the 3:2 MMR with Jupiter, where Hildas can be found (see Fig. 1.1). Some of the asteroids ejected from the main belt can also fall into the Sun. Gladman et al. (1997) showed that $25-30\%$ of resonant bodies from the 3:1 MMR go into the Sun.

The clumps of asteroids are the second important pattern of the main belt. They are called Hirayama families (Hirayama, 1918) and were created by a mutual collision of asteroids. The objects that belong to the same family have similar orbits, colours, spectra and albedos. Nesvorný et al. (2015) discussed family memberships for 122 families using the Hierarchical Clustering Method (Zappala et al., 1990). This method is very sensitive to the chosen cutoff distance and to identify the family members it is necessary to account also for colours and spectra. In this work, we focus on 13 most important, large families (with parent body larger than $100\,\mathrm{km}$) created by catastrophic disruptions, which means that the mass of the largest fragment is smaller than 0.5 of the mass of the parent body.

The total mass of asteroids in the current main belt is $M_{\mathrm{MB}} \sim 13.5 \times 10^{-10}\,M_\odot$ (Kuchynka and Folkner, 2013). However, the primordial (post-accretion) belt contained more than 100 times more mass that was removed during its evolution. The evolution of the main belt towards the current state can be described in three steps (Morbidelli et al., 2015): (i) an early strong dynamical excitation ~ 4.5 Gyr ago that caused the formerly circular ($e, \sin I \lesssim 0.001$) orbits of asteroids to have wide range of values of eccentricity and inclination together with asteroid removal that left about four times the current asteroid population; (ii) a temporary late instability of giant planets which caused a second excitation ~ 4.1 Gy ago and the asteroid belt lost $\sim 50\%$ of bodies; (iii) during the following 100 My, another 50% of asteroids was lost due to the sweeping resonances (mean motion and secular) with the giant planets. The main belt is now in a quasi-steady state, where collisional rate is approximately constant and where non-gravitational forces such as Yarkovsky effect and Yarkovsky-O'Keefe-Radzievskii-Paddack (YORP) effect influence the orbits and rotations of asteroids, together with gravitational perturbations, close encounters and other phenomena.

1.2 Basic physical properties of asteroids

Up to now, we know orbits of $\sim 720\,000$ asteroids. The parameters describing osculating orbits (semimajor axis a, eccentricity e, inclination I, longitude of

---

[1]Secular resonance occurs when the precession rate of the asteroid orbit is equal to one of the fundamental frequencies of the precession of the planets orbits. ν_6 is a linear secular resonance between an asteroid and Saturn.

ascending node Ω and argument of perihelion ω) as well as absolute magnitude H can be found in the Asteroid Orbital Elements Database (AstOrb[2]) or Minor Planet Center Orbit (MPCORB) Database[3]. The proper values are stored in Asteroid Dynamic Site (AstDyS) catalog (Knežević and Milani, 2003).

For $\sim$19 000 asteroids, the rotational periods are stored in The Asteroid Lightcurve Database (LCDB[4]) (Warner et al., 2009). In Fig. 1.2, we plot the dependence of rotation rate ω on diameter D for the LCDB data. We can notice that (i) among the asteroids larger than $\sim$10 km, there are not fast rotators ($\omega \gtrsim 10$ rev/day); (ii) there is a group of very fast small rotators ($D \lesssim 0.1$ km) and (iii) there is also a group of slow small rotators. The source of such extreme rotators, fast and slow, is probably the YORP effect. The limit diameter D_{YORP} for YORP-driven evolution of spin for the timescale of $\tau = 4.5$ Gyr is

$$D_{\mathrm{YORP}} = \left(\frac{\tau}{\tau_0} c_{\mathrm{YORP}} \left(\frac{a}{a_0} \right)^{-2} \left(\frac{\rho}{\rho_0} \right)^{-1} \right)^{\frac{1}{2}} D_0 \,, \qquad (1.1)$$

where $\tau_0 = 11.9$ Myr, $a_0 = 2.5$ au, $D_0 = 2$ km, $\rho_0 = 2500$ kg m^{-3} (Čapek and Vokrouhlický, 2004). The appropriate D_{YORP} is shown in Fig. 1.2. We also plotted two limit frequencies (both for the timescale $\tau = 4.5$ Gyr): (i) the limit frequency for the collisional reorientation

$$\omega_{\mathrm{reor}} = \left(\frac{\tau}{B} \left(\frac{D}{D_0} \right)^{-\beta_2} \right)^{\frac{1}{\beta_1}} \omega_0 \,, \qquad (1.2)$$

where $B = 84.5$ kyr, $\omega_0 = 2\pi/P_0$, $P_0 = 5$ h, $\beta_1 = 5/6$, and $\beta_2 = 4/3$ (Farinella et al., 1998); and (ii) the limit frequency for the damping of non-principal-axis rotation (Hestroffer and Tanga, 2006)

$$\omega_{\mathrm{damp}} = \left(\frac{\mu Q}{\tau \rho K_1^2 (D/2)^2} \right)^{\frac{1}{3}} \,, \qquad (1.3)$$

where $\rho = 2500$ kg m^{-3}, $K_1^2 \simeq 0.1$, and the value $\mu Q = 5 \times 10^{12}$ Pa. Finally, we plotted the critical rotation rate (Pravec and Harris, 2000)

$$\omega_{\mathrm{crit}} = \sqrt{(4/3)\pi G \rho} \,, \qquad (1.4)$$

where G is the gravitational constant.

For $\sim$1000 asteroids, the rotation periods derived from the lightcurve inversion method are also stored in the Database of Asteroid Models from Inversion Techniques (DAMIT[5] Ďurech et al., 2010) (see also Fig. 1.2). Besides the rotational period, three-dimensional convex asteroid models are available in DAMIT. More informations about asteroid shapes and models will be given in Sec. 2.2.

According to their visual and infrared reflectance spectra, we can divide asteroids into taxonomic classes that represents also different chemical compositions. For $\sim 60,000$ asteroids we have an information about spectral type thanks to

---
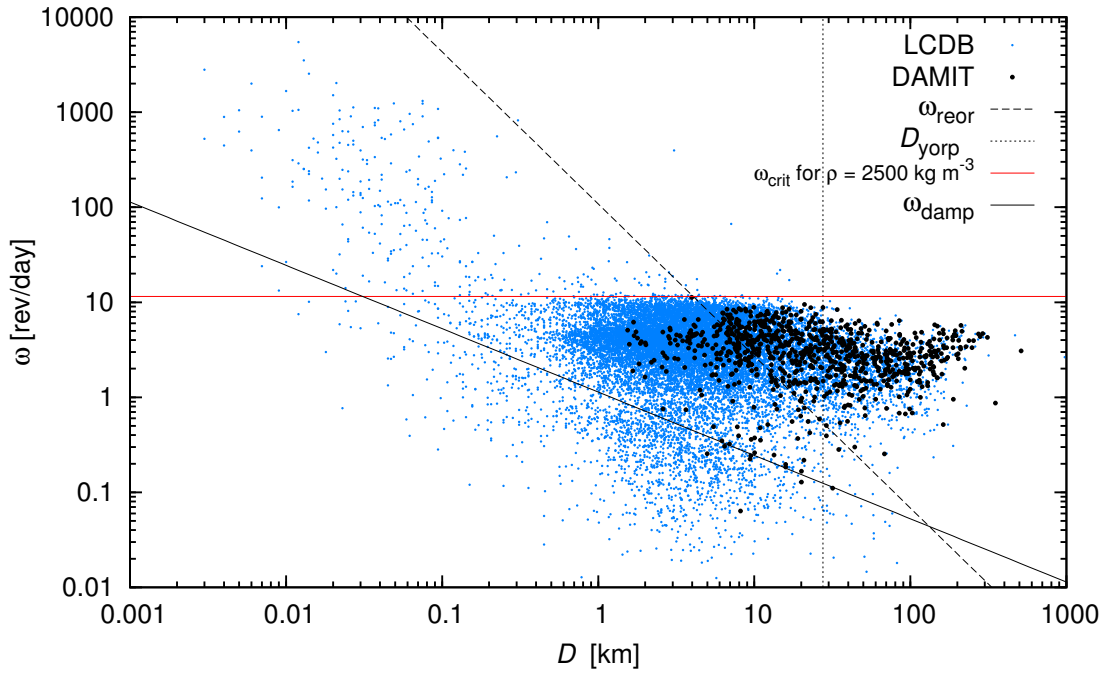
Figure 1.2: The rotation rate ω as a function of diameter D for $\sim$19 000 asteroids from the LCDB database (Warner et al., 2009, blue points) and for $\sim$1000 asteroids from DAMIT database (Ďurech et al., 2010, black points). We also plotted the limit frequency for the collisional reorientation of the spin ω_{reor} on the timescale of $\tau = 4.5\,\mathrm{Gyr}$, the limit frequency for damping of the excited rotation to the lowest energy state of principal-axis rotation ω_{damp} (again for $\tau = 4.5\,\mathrm{Gyr}$), the limit diameter for YORP-driven evolution of spin axis D_{yorp} ($\tau = 4.5\,\mathrm{Gyr}$) and the critical rotation rate ω_{crit}.

the Sloan Digital Sky Survey (SDSS). Data are available on Planetary Data System[6], Asteroid Taxonomy V6_0 (Carvano et al., 2010). Besides spectra, SDSS provides also asteroid color in five filters: u, g, r, i, z. An overview of the progress concerning the compositional structure of the main belt can be found in DeMeo et al. (2015). Here, we include only basic information. The three main taxonomic complexes that group together classes with similar characteristics are following:

- S-complex (silicaceous bodies) with spectra showing strong absorptions at 1 and 2 μm (olivine, pyroxene) and the slope of a spectrum high;

- C-complex (carbonaceous objects) with spectra showing small or no features and the slope of a spectrum low or medium;

- X-complex (multiple composition) also displays either small or no features and has a medium or high slope of spectrum.

Besides these main complexes, there are other, less common, classes that can be distinguished: V, R, O, Q, A, K, L, D, T, B. DeMeo et al. (2009) defined in total 24 taxonomic classes using the Principal Component Analysis; their spectra are shown in Fig. 1.3. Although the different taxonomic complexes clearly dominate in different parts of the main belt, they are also partly mixed as a result of the dynamical evolution of the main belt and we can see all types of asteroids in every region of the main belt. More than a half of the mass of S-types is located outside the inner belt. Also with decreasing size of asteroids in the inner belt, the contribution of C-types increases. A detailed compositional mass distribution of taxonomic classes can be found in DeMeo and Carry (2014).

The spectra and colors of asteroids can also help us to determine the membership to dynamical families (Nesvorný et al., 2015). Since all members were originally a part of one object, they should belong to the same taxonomic class. Nevertheless, it is not a definite rule, because we have to take into account that large parent body could be differentiated, therefore, it is possible that fragments will be of different taxonomic classes. Another process that has to be mentioned is space weathering that affect the physical and optical properties of the surface. Nesvorný et al. (2005) studied color variations between young and old asteroid families and found that colors of asteroids changed over time: the S-types become redder and their spectral slope increases; for the C-types they suggested behavior opposite to the S-types.

For size and albedo determinations, the infrared observations are useful. The infrared catalogue[7] based on the AKARI All-Sky Survey (Shibai, 2007) was published on 2010 March. AKARI observed in the wavelength range from 1.7μm (near-infrared) to 180μm (far-infrared) and provides the sizes and albedos for 5120 asteroids (Usui et al., 2011). Thanks to the Wide-field Infrared Survey Explorer (WISE), we have the albedo informations and sizes for more than one hundred thousand asteroids (Masiero et al., 2011; Mainzer et al., 2011a). In four infrared wavelengths, 3.4, 4.6, 12, and 22 μm, WISE has observed nearly two orders of magnitude more minor planets than the Infrared Astronomical Satellite (IRAS, Tedesco et al., 1988). The minimum relative diameter and albedo errors are ~10% and ~20%, respectively (Mainzer et al., 2011b).

---

[6]https://sbn.psi.edu/pds/resource/sdsstax.html
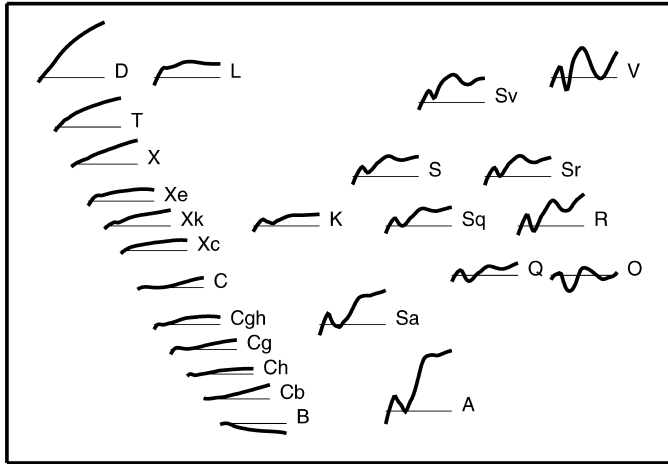[7]http://darts.isas.jaxa.jp/ir/akari

Figure 1.3: The average spectra for 24 taxonomic classes defined over 0.45–2.45 μm with constant horizontal and vertical scaling. Figure is taken from DeMeo et al. (2009).

Density ρ is a basic property for understanding of compositions of asteroids and their internal structure. Carry (2012) compiled densities for 287 small bodies, out of which 230 were main-belt asteroids. He provided average density for each of 24 taxonomic classes defined in DeMeo et al. (2009). With the level of accuracy 20% (caused by mass and diameter estimates discussed in the paper in detail), he found for the C-complex ρ from 1.25 ± 0.21 to $1.41 \pm 0.29\,\mathrm{g/cm^3}$, for S-complex 2.72 ± 0.54 to $3.43 \pm 0.20\,\mathrm{g/cm^3}$. Both complexes show a trend of increasing density with mass. For X-types, the interval of ρ is wide: from 1.85 ± 0.81 to $4.86 \pm 0.81\,\mathrm{g/cm^3}$, which suggests that in the X-complex, multiple compositions are present. With the level of accuracy 50% the intervals are wider. For details see Figure 7 or Table 3 in the respective paper.

In this Chapter, we introduced some of the asteroid properties, according to which we can divide asteroids into different groups (e.g., taxonomic classes, dynamical families, fast vs. slow rotators, asteroids with different sizes and others). We were interested if the groups different within a certain classification will differ also in spin or shape distributions. We studied this problem in two different ways. First, we derived the spin longitudes and latitudes and shape elongations for individual asteroids and constructed distributions for selected groups that we wanted to compare (Chapter 3). Next, we considered the whole asteroid populations right at the beginning and derived directly the distributions of studied parameters (Chapter 4).

2. Spin states and models of asteroids

The information about asteroid rotational state and shape elongation can be obtained from photometry. A significant progress of this problem began with the development of the lightcurve inversion method (Kaasalainen and Torppa, 2001; Kaasalainen et al., 2001) discussed in Sec. 2.2.4. The photometric data can be obtained in two different modes of observation: (i) data dense in time consists typically of tens to hundreds of measurements during few hours and thus sample well the rotational period P (these data are suitable for lightcurve inversion); (ii) data sparse in time are produced by all-sky surveys and consists typically of few measurements per night over a timescale $\sim$10 years.

2.1 Asteroid rotation

The time evolution of the brightness L of an asteroid observed near opposition, the lightcurve, is typically a double sinusoidal curve. The rotation of an irregular asteroid causes changes in asteroid brightness together with different geometry of individual measurements and scattering effects. With the phase angle α (the angle between the direction to the Sun and to the Earth) approaching zero, the asteroid brightness grows, since the illuminated part of the surface is maximal for $\alpha = 0°$. Moreover, a significant growth of the asteroid brightness for small α (known as the opposition effect) is caused by the coherent backscattering and the lack of shadowing. The light reflection from the element on the asteroid surface is described by the scattering law $S = S(\mu, \mu_0, \varpi, \alpha)$, where $\mu = \mathbf{e} \cdot \mathbf{n}$, $\mu_0 = \mathbf{s} \cdot \mathbf{n}$ and ϖ denotes albedo, $\mathbf{n}$ denotes the unit surface normal, $\mathbf{e}$ and $\mathbf{s}$ are the unit vectors pointing to the Earth and to the Sun. The most often used scattering laws are: (i) Hapke model (Hapke, 1981, 1993); (ii) Lumme-Bowell model (Lumme and Bowell, 1981); (iii) Lommel-Seeliger law or (iv) Lambert law and also a combination of (iii) and (iv). A special case when the reflected brightness depends only on the projected area ($S = \mu$) is the geometric scattering. Such approximation can be used for analyzing data obtained from observations with small phase angle. An overview about the advances concerning asteroid scattering can be found in Muinonen et al. (2002) or Li et al. (2015).

2.1.1 The previous statistical studies of spin states of asteroids

The first statistical study of pole orientation of asteroids was done by Magnusson (1986) on a sample of 20 asteroids, with 17 of them larger than 100 km. To determine the pole position (ecliptical longitude λ and latitude β), he used two different methods: amplitude-magnitude method and the epoch method that uses the variations in the observed synodic period of rotation. His main result was that spin axes seem isotropically distributed. He found a flat distribution of longitudes and a slight (statistically insignificant) majority of prograde rotators.

From the simulations of the collisional evolution of asteroids, Davis et al. (1989) also suggested an isotropic distribution of rotational axes.

On a sample of 83 asteroids, Pravec et al. (2002) realized that there is a lack of poles close to the ecliptic plane. This was also confirmed by, e.g., Skoglöv and Erikson (2002) on a sample of 73 main-belt asteroids. Moreover, they suggested a possibility that the observed depopulation of spin axes could be caused by a correlation with the inclination of orbit I. For $I > 10°$ they found the relevant depopulation, while asteroids with $I < 10°$ have a more regular spin vector distribution. They explain this behaviour as due to the different dynamical evolution of the spin axes of asteroids with different orbit inclinations. Pravec et al. (2002) also studied the distribution of rotational periods P and found that for asteroids larger than $\sim 40\,\mathrm{km}$, the distribution is close to Maxwellian, while small asteroids, with $0.15 < D < 10\,\mathrm{km}$, show significant excesses of both fast and slow rotators. Small asteroids ($D < 15\,\mathrm{km}$) were studied in detail in Pravec et al. (2008), who found that their spin rates appear heavily evolved by the YORP effect and processes at the fast spin barrier (11 rev/day Pravec et al., 2007).

Kryszczyńska et al. (2007) performed a statistic study for 92 MBAs and 21 NEAs and found there is clear excess of retrograde rotators among NEAs. This was already discussed in La Spina et al. (2004) and it is in agreement with the theoretical predictions of the Yarkovsky model. The main source of NEAs are the resonances 3:1 and ν_6. Since only the objects with retrograde spins can enter the ν_6 resonance through the Yarkovsky effect, it is more probable for the retrograde rotators to become NEAs. Kryszczyńska et al. (2007) also tested the correlation of MBAs' β distribution with inclination of orbit suggested by Skoglöv and Erikson (2002), however, they did not find the correlation to be significant. The constructed distribution of pole longitudes λ for both MBAs and NEAs did not show any statistically significant clustering.

With the growing number of asteroids for which pole orientation have been determined, a reliable statistics could be achieved. Hanuš et al. (2011), using a sample of 206 main belt asteroids, found the dependence of the latitudes distribution on the diameter D. For $D > 60\,\mathrm{km}$ they found nearly isotropic distribution of β value lower than $11°$ and evident excess of prograde rotators ($\beta > 11°$). For $D \lesssim 30\,\mathrm{km}$, the distribution of β value was found to have a strong preference for either low or high values indicating pole orientation near the pole of the ecliptic. The lack of poles near the ecliptic plane is due to the YORP effect, which can alter the direction of the spin axes of asteroids smaller than $\approx 40\,\mathrm{km}$ on a timescale shorter than their collisional lifetime (e.g., Pravec and Harris, 2000; Rubincam, 2000). The distribution of ecliptical longitudes λ seemed uniform as in the previous works. Nevertheless, their data sample was probably too small to indicate meaningful nonuniformities.

Considering the λ distribution, Slivan (2002) and Slivan et al. (2003) revealed, on the contrary to the aforementioned papers, a nonuniform distribution of λ for nine members of the Koronis family with diameters from ~ 20 to $\sim 40\,\mathrm{km}$. In particular, the prograde-rotating asteroids all had pole latitude λ between $24°$ and $73°$. This conundrum was resolved by Vokrouhlický et al. (2003), who showed that these objects underwent a $2 - 3$ Gy long dynamical evolution during which the YORP effect tilted their spin axis towards the ecliptic pole. Since YORP continued to decrease the rotation frequency in their dynamical model, the spin

state was captured in the Cassini resonance between the pole precession owing to solar torque and orbit precession from Jupiter-Saturn perturbations. The stationary point of this particular spin-orbit resonance is currently at $\lambda \simeq 35°$. Consequently all bodies whose spin axes librate about this point must have λ near this value.

More recently, Bowell et al. (2014) estimated the ecliptical longitudes λ for more than 350 000 asteroids of the main belt using the magnitude method (Magnusson, 1986), based on the variation of brightness with the ecliptical longitude: the maximum of brightness corresponds to the spin axis pointing either toward or opposite from the Earth. Surprisingly, the resulting λ distribution is clearly nonuniform with an excess of asteroids with λ from 30° to 110° and with a minimum from 120° to 160°, which have not been yet explained.

In this thesis, we continue in these statistical studies having a new method and extensive photometric data and we focus on MBAs altogether as well as on smaller selected asteroid populations.

2.2   Shape models of asteroids

Besides the spin orientation, in this thesis, we are focused on the elongation of asteroids defined by the axes ratio a/b which is the simplest description of the asteroid shape. Thus, in this section, we will describe the most important sources of information about asteroid shapes and also some methods for the determination of two- and three-dimensional models of asteroids. Our motivation is to provide an overview, what can be found about these objects, how detailed structures can be identified and also to emphasize that these achievements cover only a small fraction of the whole population of asteroids.

2.2.1   Space probe flybys

The first asteroid approached by a space probe was (951) Gaspra in 1991 by the Galileo spacecraft (Belton et al., 1992; Veverka et al., 1994) (see Fig. 2.1 on the left) that revealed it to be an irregular body ($19 \times 12 \times 11$ km) with many craters. The first asteroid orbited by a spacecraft was the near-Earth asteroid (433) Eros (Veverka et al., 2001) (the spacecraft NEAR Shoemaker landed in 2001). Till today, we have in situ observations from space probe flybys for 11 minor planets: (4) Vesta, (21) Lutetia, (243) Ida, (253) Mathilde, (433) Eros, (951) Gaspra, (2867) Šteins, (4179) Toutatis, (5535) Annefrank, (9969) Braille and (25143) Itokawa; and dwarf planets Ceres and Pluto. During a single flyby, a part of the body remains unseen. The reconstruction of the dark side can be done using the procedure described in Kaasalainen and Viikinkoski (2012).

2.2.2   Stellar occultations

A two-dimensional shape projection of an asteroid can be obtained from a stellar occultation. From the duration of the disappearance of a star behind the asteroid, we can determine a chord – a length on the disk of the asteroid. With a combination of chords, obtained from different locations on the Earth, we can construct a projection of the shape of an asteroid. An example of shape projection
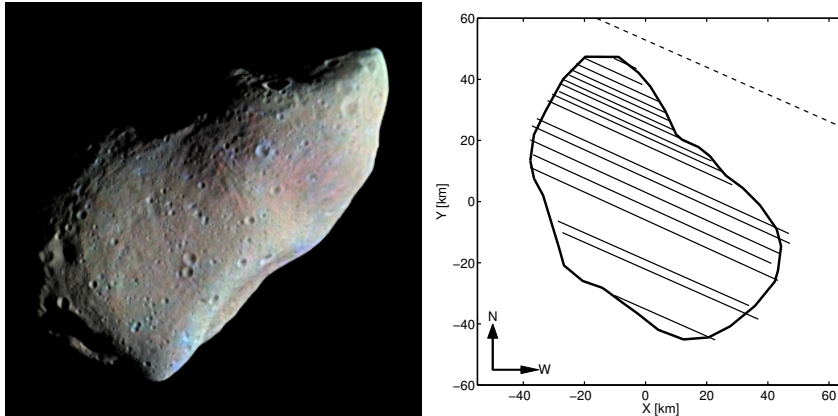
Figure 2.1: Left: A picture of (951) Gaspra. A mosaic of two images taken by the Galileo spacecraft, NASA. Right: The shape projection of asteroid (135) Hertha based on stellar occultations (Timerson et al., 2009).

of asteroid (135) Hertha is shown in Fig. 2.1 on the right. Dunham et al. (2014) compiled data for 2102 occultations (annually, there is a new compilation), from which ∼ 40 are good enough for a reconstruction of asteroid's shape projection. The remaining ones can be used for determination of asteroid sizes or at least for a scaling of three-dimensional models (Ďurech et al., 2011; Hanuš et al., 2017b).

2.2.3   Radar observations

The two-dimensional images can be obtained by radar techniques based on delay-Doppler imaging. In this method, we measure the Doppler frequency and echo power in time delay and with adequate orientation coverage, such images can be used to construct detailed three-dimensional models and define the rotation state precisely. The two most sensitive facilities are Arecibo Observatory in Puerto Rico and Goldstone Solar System Radar at the NASA's Goldstone Deep Space Communications Complex. The details about the radar technique can be found in Ostro et al. (2002), here we only point out the main benefits and new findings of radar observations.

Since the echo power steeply decreases with the distance to the object, the main-belt asteroids are not suitable for detailed imaging, nevertheless, some of them were already imaged, e.g., (4) Vesta, (5) Astraea, (7) Iris, (216) Kleopatra (see Fig. 2.2). The situation is better for near-Earth asteroids as almost 100 objects are observed with radar annually (Benner et al., 2015).

Using the radar technique, it is possible to detect the Yarkovsky drift. The first direct detection was on (6489) Golevka (Chesley et al., 2003). Recently, the attention is focused on Yarkovsky drift on NEAs (Farnocchia et al., 2013a,b; Chesley et al., 2015). A combination with optical observation revealed the evidence of the YORP effect (asteroid later logically named as (54509) YORP) (Lowry et al., 2007; Taylor et al., 2007). At the same time, the evidence of the YORP effect was also obtained from photometric lightcurves of asteroid (1862) Apollo (Kaasalainen et al., 2007). Radar observations also revealed binaries, contact binaries and triple systems. For many rapidly rotating NEAs, equatorial bulges
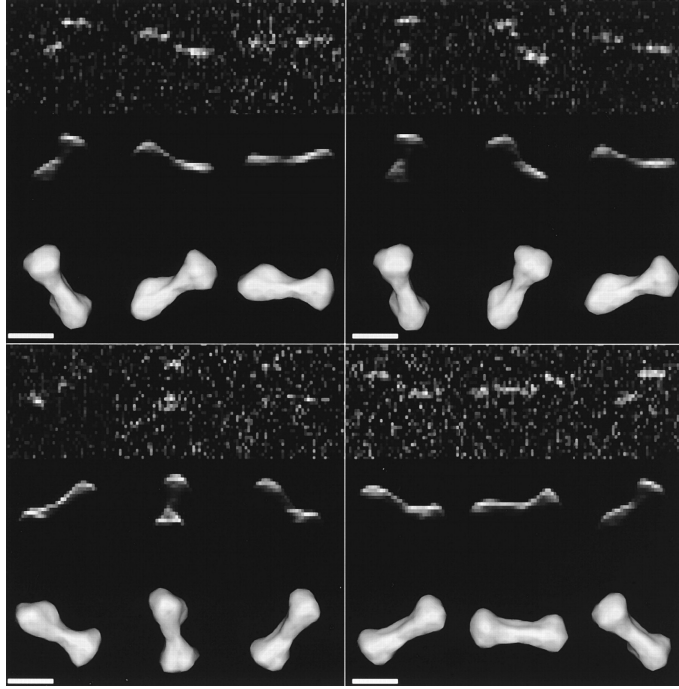
Figure 2.2: Arecibo radar images of asteroid (216) Kleopatra (top rows) and results of shape reconstruction (bottom rows). The figure is taken from Ostro et al. (2000).

were found in radar images (e.g., (66391) 1999 KW4, Scheeres et al., 2006); on the surface of NEAs, even small impact craters and boulders can be found.

A new technique developed by Busch et al. (2010) that enables to estimate the spin vectors is speckle tracking. Due to the interference of reflections from different parts of the asteroid's surface a radar echo contains a characteristic pattern of speckles that moves as the asteroid rotates. By tracking the motion of the pattern it is possible to determine the pole direction of the asteroid.

2.2.4 Lightcurve inversion

Nevertheless, the main method for determination of shapes and spin states of asteroids is the inversion of lightcurves, which was developed by Kaasalainen and Torppa (2001) and Kaasalainen et al. (2001). Most of the convex shape models obtained with this method are stored in the DAMIT database (Ďurech et al., 2010). These models are a good approximation of the whole asteroid, but are not able to reveal craters and other small-scale and non-convex structures on the surface.

To solve the inverse problem means to express the asteroid observed brightness as a function of free parameters describing asteroid shape, rotational state, geometry of observation, surface scattering properties and time. These parameters are fitted and the unique sidereal rotational period P has to be determined. In the case of dense photometric data, we can substantially reduce the computational time necessary for the determination of P by only searching the interval around the value estimated from dense light curves. The relative accuracy of the period determined from lightcurves is 10^{-5} or better and depends mainly on

the time distribution of observations (Ďurech et al., 2015a). For sparse data, we usually do not have any estimate of P and we have to search the interval of all possible values, which is time consuming. Moreover, for the majority of asteroids we currently do not have sparse data that is accurate enough to derive a unique rotational period. Kaasalainen (2004), Ďurech et al. (2005), and Ďurech et al. (2007) showed that it is possible to get the solution of the inverse problem from sparse photometry if the data noise is $\lesssim 5\%$. Using the distributed computing project Asteroids@home (Ďurech et al., 2015b), which significantly reduces the computational time of the period search, Ďurech et al. (2016) derived 328 new models from the analysis of sparse Lowell photometric data. New asteroid models were also derived with a combination of dense and sparse photometry (Ďurech et al., 2009; Hanuš et al., 2011, 2013, 2016).

All the described methods work with individual objects and although the number of models is growing and in a few next years we will have thousands of models (e.g., thanks to the Gaia satellite), it is essentially impossible to get models for all asteroids. A different statistical approach was used by Nortunen et al. (2017), where they described physical parameters for selected populations of asteroids with distribution functions. They constructed cumulative distribution functions (CDFs) of variation of brightness for selected groups of asteroids and studied the inverse problem. A similar approach was used by Szabó and Kiss (2008) or McNeill et al. (2016). In this work, we created a new model that works with individual asteroids, but we interpret the results in a statistical sense.

3. Analysis of the photometric data from the Lowell Observatory database

In this Chapter, we introduce a new model that determines the orientation of spin axes and elongation of asteroids. As mentioned in the previous section, the sparse photometric data are a rich source of information about asteroids, nevertheless the quality of the data is often not good enough for a unique solution of the lightcurve inversion. Therefore, we developed a new method that was published in Cibulková et al. (2016) and the author of its mathematical background is Mikko Kaasalainen, one of the coauthors of the paper. First, we describe the model and test its reliability on synthetic data. Then, we apply it on the photometric data from the Lowell Observatory database and analyze the results.

3.1 Description of the model

Asteroids are modeled as geometrically scattering triaxial ellipsoids ($a \geq b \geq c = 1$) rotating about the shortest axis of the inertia tensor. The model has four free parameters: the ecliptic longitude λ and latitude β of the pole and the ratios of axes a/b and b/c of the ellipsoid. The advantage of this model is that the brightness L, which is proportional to the projected area of the illuminated and visible part of the surface, can be computed analytically (Connelly and Ostro, 1984) as follows:

$$L \propto \frac{\pi abc}{2} \left(\sqrt{\mathbf{e}^{\mathrm{T}} M \mathbf{e}} + \frac{\mathbf{e}^{\mathrm{T}} M \mathbf{s}}{\sqrt{\mathbf{s}^{\mathrm{T}} M \mathbf{s}}} \right) , \tag{3.1}$$

where $\mathbf{e}$, $\mathbf{s}$ denote unit vectors defining the position of the Earth and the Sun in the asteroid coordinate system of principal axes of the inertia tensor, and

$$M = \begin{pmatrix} 1/a^2 & 0 & 0 \\ 0 & 1/b^2 & 0 \\ 0 & 0 & 1/c^2 \end{pmatrix} . \tag{3.2}$$

In a special case of opposition $\mathbf{e} = \mathbf{s}$, Eq. (3.1) simplifies to

$$L \propto \pi abc \sqrt{\mathbf{e}^{\mathrm{T}} M \mathbf{e}} . \tag{3.3}$$

The direction toward the Earth can be described by the rotational angle ϕ and the aspect angle θ (i.e., the angle between $\mathbf{e}$ and the spin axis direction),

$$\mathbf{e} = [\sin \theta \cos \phi, \sin \theta \sin \phi, \cos \theta]^{\mathrm{T}} . \tag{3.4}$$

Having set $c = 1$, the squared brightness L^2 normalized by the maximal possible value πab is

$$L^2 = \frac{\sin^2 \theta \cos^2 \phi}{a^2} + \frac{\sin^2 \theta \sin^2 \phi}{b^2} + \cos^2 \theta . \tag{3.5}$$

The mean quadratic brightness over one rotational period is then

$$\langle L^2 \rangle = \frac{1}{2\pi} \int_0^{2\pi} L^2 \mathrm{d}\phi = 1 + \frac{1}{2}\sin^2\theta \left(\frac{1}{a^2} + \frac{1}{b^2} - 2 \right) , \qquad (3.6)$$

and the normalized dispersion of squared brightness is

$$\eta = \frac{\sqrt{\mathrm{var}(L^2)}}{\langle L^2 \rangle} = \frac{\sqrt{\langle (L^2 - \langle L^2 \rangle)^2 \rangle}}{\langle L^2 \rangle} =$$

$$= \frac{a^2 - b^2}{\sqrt{8}} \left[\frac{a^2 b^2}{\sin^2\theta} + \frac{1}{2}(a^2 + b^2 - 2a^2 b^2) \right]^{-1} . \qquad (3.7)$$

We used Eqs. (3.6) and (3.7) to compute $\langle L^2_{\mathrm{model}} \rangle$ and η_{model} for each asteroid and for each of its apparitions; we defined apparitions as sets of observations with the gap between sets of at least 100 days. We note that in combining equations (3.6) and (3.7) we obtain, for a given asteroid, the relation between $\langle L^2 \rangle$ and η,

$$\eta = \frac{1}{\sqrt{2}} \frac{a^2 - b^2}{a^2 + b^2 - 2a^2 b^2} \left[1 - \frac{1}{\langle L^2 \rangle} \right] . \qquad (3.8)$$

This implies that for large $\langle L^2 \rangle$ the model predicts small dispersion η. This is in accord with the intuition that a large brightness corresponds to the pole-on geometry of view (i.e., small aspect angle θ).

For the observational data, we used the following procedure. First, we removed the dependence on solar phase angle, because not only rotation, but also the different geometry of observations changes the asteroid brightness. In the model, we assume the case of opposition, which means the solar phase angle $\alpha = 0$. For the observational data, we fitted the dependence of the brightness on α by a linear–exponential dependence similar to Hanuš et al. (2011) (see Fig. 3.1), i.e.,

$$g \left(h \exp^{-\alpha/d} - k\alpha + 1 \right) \frac{1 + \cos\alpha}{2} , \qquad (3.9)$$

where g, h, d and k are four additional free parameters fitted for each asteroid. We simply divided the observed brightness by this function. As an example, the corrected data for asteroid (511) Davida are shown in Fig. 3.2. Next, we required that there were enough data for each asteroid, specifically, at least 20 points in each apparition and at least five apparitions for one asteroid (in Fig. 3.2 there are data from ten apparitions that can be used).

We compared computed theoretical values of the mean brightness $\langle L^2 \rangle$ and of the dispersion of the brightness η with observations by means of χ^2 that we defined as

$$\chi^2 = \chi^2_\eta + w\chi^2_{L^2} = \sum_{\mathrm{apparitions}} \frac{(\eta_{\mathrm{model}} - \eta_{\mathrm{obs}})^2}{\sigma^2_\eta} +$$

$$+ w \sum_{\mathrm{apparitions}} \frac{(\langle L^2_{\mathrm{model}} \rangle / \overline{\langle L^2_{\mathrm{model}} \rangle} - \langle L^2_{\mathrm{obs}} \rangle / \overline{\langle L^2_{\mathrm{obs}} \rangle})^2}{\sigma^2_{L^2}} , \qquad (3.10)$$

where σ denotes the standard deviation and w denotes the weight for $\chi^2_{L^2}$ of squared brightness. To normalize values of calculated and observed mean squared
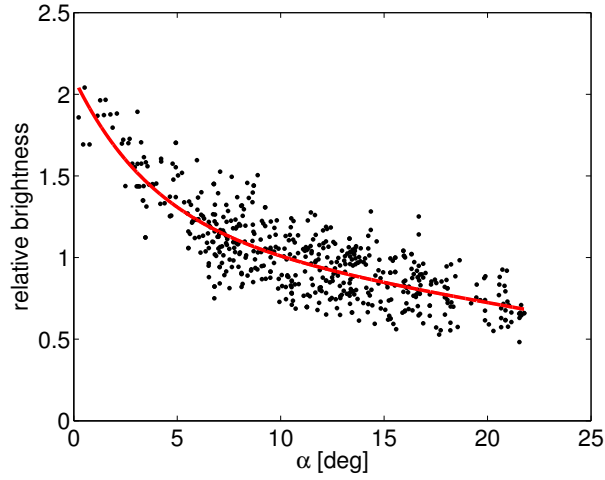
Figure 3.1: The dependence of the brightness L on the phase angle α for asteroid (511) Davida. The red line represents the fitted linear–exponential function (Eq. 3.9). The appropriate free parameters are: $g = 1.144$, $h = 0.836$, $d = 0.0686$, $k = -1.00988$.
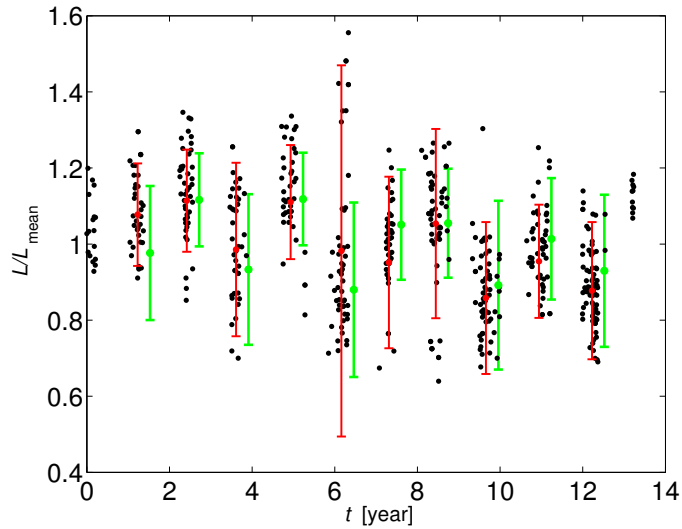
Figure 3.2: Photometric data from the Lowell Observatory database of asteroid (511) Davida corrected by the influence of the solar phase angle (black points). Red points with vertical lines denote the observed mean brightness and its dispersion in individual apparitions, green colour denotes the same but calculated quantities for the best-fit model. To normalize L, we divided each value by the mean value L_{mean} calculated over all apparitions. There are 10 apparitions with sufficient number of measurements.

19

brightness, we divided them by the mean values calculated over all apparitions, $\overline{\langle L^2_{\mathrm{model}} \rangle}$ and $\overline{\langle L^2_{\mathrm{obs}} \rangle}$, respectively. The value of w is not set in advance and has to be found by testing on known data. Since $\langle L^2 \rangle$ and η are not Gaussian random variables, the χ^2 in relation (3.10) is not χ^2 distributed. Nevertheless, we use this χ^2 formalism to define the best solution, which has the minimum χ^2.

To find a model with the best agreement (the lowest χ^2) between the calculated values and the observation, we computed model values on a grid in parameter space: the ecliptical longitude λ of the pole from $0°$ to $360°$; the latitude β from $0°$ to $90°$, both with a $5°$ step, and the axes a and b, from 1.1 to 4 and from 1 to a, respectively, both with a 0.1 step (an elongation larger than $4:1$ is considered unrealistic). As mentioned above, we corrected the observed brightness to the solar phase angle $\alpha = 0$. However, we used the real unchanged geometry of measurements and the aspect angle θ, which appears in Eqs. (3.6) and (3.7), was calculated as a mean value for each apparition as follows:

$$\cos \theta_{\mathrm{mean}} = \mathbf{v} \cdot \mathbf{e}_{\mathrm{mean}} \,, \tag{3.11}$$

where $\mathbf{v} = [\cos \beta \cos \lambda, \cos \beta \sin \lambda, \sin \beta]^{\mathrm{T}}$ is the vector defining the direction of the spin axis and $\mathbf{e}_{\mathrm{mean}}$ is the mean vector defining the position of the Earth during one apparition. From the relation (3.11) we can see that we obtain the same aspect angle for λ, β and $\lambda \pm 180°$, $-\beta$. This is the reason why we test β only in the interval from $0°$ to $90°$ (instead of the full interval $-90°$ to $90°$). Relation (3.11) also indicates that, for most asteroids, there is only a slightly worse second minimum of χ^2 for $\lambda \pm 180°$. For zero inclination of the orbit ($e_z = 0$), the aspect angle would be the same for λ and $\lambda \pm 180°$. Because of this ambiguity in λ, we constructed distributions of λ only in the interval $0°$ to $180°$ and for $\lambda > 180°$ we used modulo $180°$.

3.2   Tests on synthetic data

We tested the reliability of the model on synthetic data created as follows. We computed the brightness of asteroids using the shape models from DAMIT database and the Hapke scattering model (Hapke, 1981, 1993) with parameters w, g, h, B_0 and θ randomly chosen from distributions uniform on intervals $[0.02, 0.4]$ for w, $[-0.45, -0.2]$ for g, $[0.05, 0.5]$ for h, $[0.8, 1.8]$ for B_0 and $[0°, 40°]$ for θ. These new (synthetic) values were assigned to asteroids contained in the Lowell database (to the time of observation and the appropriate geometry). The distribution of poles for this synthetic data was created isotropic. Next, we added the Gaussian noise, specifically, we tested noise $\sigma_L = 0.15$ and 0.2. The noise was then subtracted according the relation

$$\eta_{\mathrm{obs}} = \sqrt{\eta^2 - \sigma^2_{L^2}} = \sqrt{\eta^2 - 4\sigma^2_L} \tag{3.12}$$

if $\eta^2 \geq 2\sigma_L$, else $\eta_{\mathrm{obs}} = 0$. We also tested synthetic data without any noise ($\sigma_L = 0$).

After applying our model to these synthetic data, we should obtain uniform distribution of the ecliptical longitudes λ and latitudes $\sin \beta$. This was indeed satisfied for the resulting distribution of λ as shown in Fig. 3.3, however, the
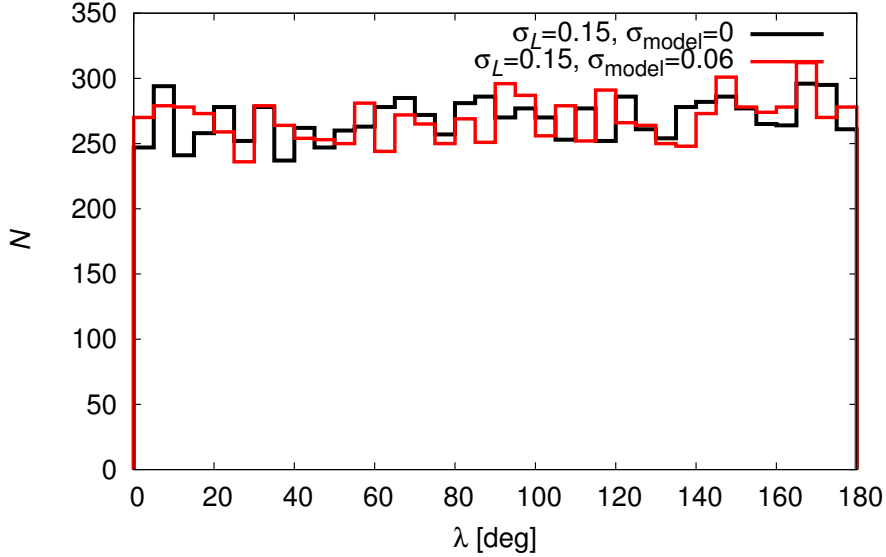
Figure 3.3: Distributions of pole longitudes λ calculated from synthetic data with noise $\sigma_L = 0.15$. The black line denotes test without model noise $\sigma_{\mathrm{model}} = 0$, the red line denote test with model noise $\sigma_{\mathrm{model}} = 0.06$.

distribution of $\sin\beta$ showed a preference for high β. The possible explanation of this result is that we did not include the uncertainties arising from the assumption of triaxial ellipsoids and also from the Hapke model. That means, for example, that for data without any noise and for an asteroid with $\beta = 0$, there are still some changes in brightness that our model interprets as nonzero β. Therefore, to correct this problem, we added a new parameter that we called model noise σ_{model}. Then the equation (3.12) had to be changed to

$$\eta_{\mathrm{obs}} = \sqrt{\eta^2 - 4\sigma_L^2 - \sigma_{\mathrm{model}}^2} \qquad (3.13)$$

if $\eta \geq \sqrt{4\sigma_L^2 + \sigma_{\mathrm{model}}^2}$, else $\eta_{\mathrm{obs}} = 0$.

We tested values $\sigma_{\mathrm{model}} = 0.05$, 0.06, 0.07 and 0.1. The resulting distributions of λ were uniform independently on σ_{model}. This is probably because λ is principally determined from the mean brightness $\langle L^2 \rangle$, which is comparatively more stable than the dispersion of brightness η from which β is determined. The distributions of $\sin\beta$ for the two best values of σ_{model} and for zero data noise $\sigma_L = 0$ are shown in the left panel of Fig. 3.4. The distributions are clearly nonuniform, nevertheless this is the best result we obtained. When we added noise to the synthetic data, we found that there is no significant difference between distributions of $\sin\beta$ for $\sigma_{\mathrm{model}} = 0.06$ and 0.07 (see Fig. 3.4 on the right) and we decided to use the value 0.06 for the real data.

The takeaway message from our tests is that (i) the determination of λ is reliable in a statistical sense, while (ii) determination of β is subject to systematic bias that needs to be corrected before interpreting the results. Therefore, we divided each distribution of $\sin\beta$ in Sec. 3.5 by the synthetic distribution with noise 0.15 and model noise 0.06 (the black curve on Fig. 3.4 on the right).
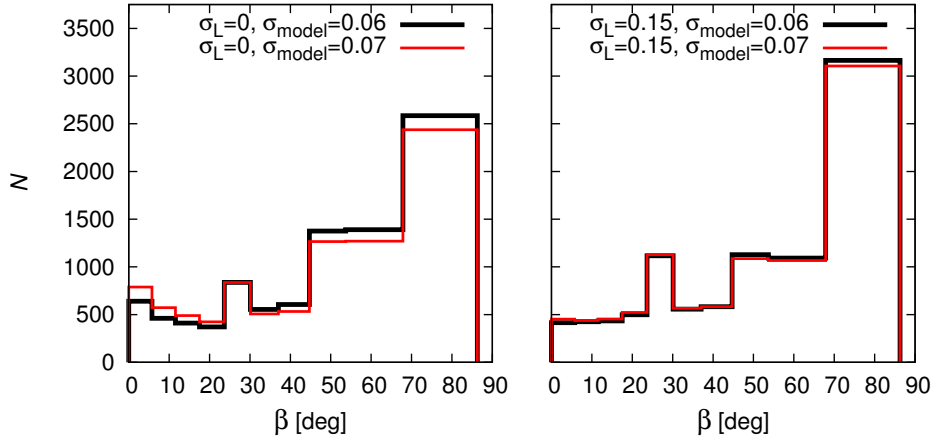
Figure 3.4: Distributions of pole latitudes β calculated from synthetic data without noise $\sigma_L = 0$ (left) and with noise $\sigma_L = 0.15$ (right) for two best values of σ_{model}. Bins are equidistant in $\sin\beta$ so an isotropic distribution would be uniform in this plot.

3.3   Tests on real data

Having tested our approach and calibrated its parameters, we applied our model on the real data from the Lowell Observatory photometric database (Bowell et al., 2014). For a detailed information about the data reduction and calibration, see Oszkiewicz et al. (2011).

3.3.1   Data description

The Lowell database contains data from 11 observatories (most of them located in the Northern Hemisphere), each having different random and systematic errors, sometimes time variable. It combines photometric data stored in the Minor Planet Center (the majority of the data pertain to MBAs and Jupiter trojans) with the orbital data from the Lowell Observatory orbital data file maintained by E. Bowell and L. H. Wasserman. Most of the photometric data are rounded to 0.1 mag. The typical rms magnitude uncertainties are 0.2 to 0.3 mag. The data were calibrated using the broadband accurate photometry of the Sloan Digital Sky Survey converted to the V band. Data for the asteroids whose brightness does not fall within the range of the SDSS (bright and very faint ones) are less reliable. In total, we had photometric data for 326 266 asteroids. For 69 053 asteroids, there were enough apparitions and data points to calculate pole longitude λ and latitude β; the vast majority of these asteroids belong to the first 100 000 numbered asteroids. For one asteroid, we could utilize 7 apparitions and 324 measurements on average.

3.3.2   A comparison with DAMIT

First, we applied the model to the data for 765 asteroids, which are also included in DAMIT database, specifically, these were asteroids selected from the first 10 000 numbered asteroids that satisfy the conditions on the number of apparitions and

the number of measurements in one apparition. We tried different values of noise level σ_L (0.08, 0.1, 0.12, 0.15) and weight w (1, 5, 25); the value of model noise was $\sigma_{\text{model}} = 0.06$. To find which is the best value of σ_L and w, we compared the calculated λ and β with λ_{DAMIT} (values from DAMIT derived with the lightcurve inversion) and β_{DAMIT}, respectively. From the distributions of $\Delta\lambda = |\lambda - \lambda_{\text{DAMIT}}|$, we found the best value of weight as $w = 5$ and from the distributions of $\Delta\beta$ we found the best value of noise level as $\sigma_L = 0.08$.

Nevertheless, we also revealed that with this assumed data noise, the model produces hardly any spheroidal asteroids $a/b \sim 1$. This is because the photometric data for less bright asteroids have higher noise level than for brighter asteroids. When considering only asteroids from DAMIT, we did not reveal this problem, because these asteroids are preferentially bright, but for less bright asteroids, the noise level $\sigma_L = 0.08$ is underestimated.

To estimate the $\sigma_L(L)$ dependence we used the magnitude amplitudes A_{mag} of lightcurves stored in the LCDB database compiled by Warner et al. (2009). For A_{mag} we can write

$$A_{\text{mag}} = 2.5 \log \frac{L_{\text{max}}}{L_{\text{min}}} = 2.5 \log \frac{L|_{\phi=0}}{L|_{\phi=\pi/2}} \,, \tag{3.14}$$

where L is given by Eq. (3.5). The normalized dispersion of brightness η, defined by Eq. (3.7), is then related to the amplitude A as

$$\eta_A = \frac{1}{\sqrt{8}} \left(\frac{1}{1 - A^2} - \frac{1}{2} \right)^{-1} \,, \tag{3.15}$$

where $A = L_{\text{min}}/L_{\text{max}} = 10^{-0.4 A_{\text{mag}}}$. For 9698 asteroids included in LCDB, we calculated η_A according to Eq. (3.15) and then the appropriate noise level in data for each asteroid is written as

$$\sigma_L = \frac{1}{2} \sqrt{\eta^2 - \eta_A^2 - \sigma_{\text{model}}^2} \tag{3.16}$$

if $\eta > \sqrt{\eta_A^2 + \sigma_{\text{model}}^2}$, else $\sigma_L = 0$. We calculated the running mean (over 500 bodies) of σ_L to get the dependence of $\sigma_L(L_{\text{mean}})$. The resulting dependence is shown in Fig. 3.5, together with the standard deviation of σ_L among corresponding 500 bodies.

This dependence was applied in our model as follows: We assumed the noise level $\sigma_L = 0.07$ for asteroids with $L_{\text{mean}} > 80$; the brightness here is a dimensionless quantity calculated from magnitude M as $L = 10^{-0.4(M-15)}$. For asteroids less bright than 80, we calculated the noise level according to the equation of the best-fit parabola,

$$\sigma_L = 0.07 + \frac{(L_{\text{mean}} - 80)^2}{110\,000} \,. \tag{3.17}$$

The corresponding curve is shown in Fig. 3.5 (red line). We can see it does not fit the data perfectly, nevertheless, considering the standard deviation of σ_L (gray lines), such difference seems insignificant.
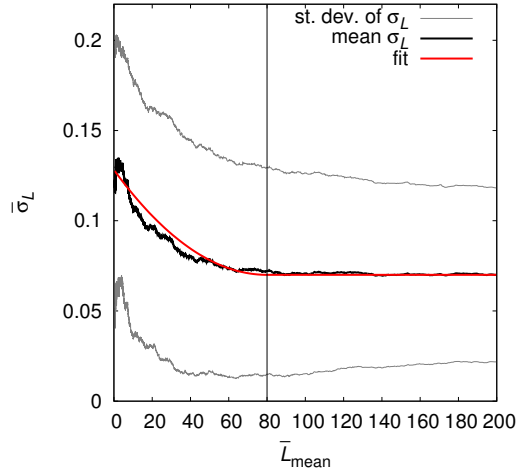
Figure 3.5: Dependence of the mean value of noise level σ_L on the mean value of L_{mean}, where L_{mean} is mean brightness over all apparitions. Each mean value was calculated from a sample of 500 asteroids (as described in the main text). Gray lines denote the standard deviation of σ_L among corresponding 500 bodies. The red line denotes the fit that was applied in the model.

3.3.3 The bootstrap method

Formally, it is always possible to obtain the best pole longitude λ, latitude β and shape elongation a/b, i.e., the lowest χ^2. However, if the minimum is flat, the parameters are not well determined. To estimate the parameter uncertainties, we applied the bootstrap method (Davison and Hinkley, 1997) on a set of measurements for each asteroid. We used the first $10\,000$ numbered asteroids[1] from the Lowell database, of which 9774 have enough data points. From the set of measurements for each asteroid we randomly selected data to get the same total number of measurements, but some of them were chosen more than once and some of them were missing. We repeated this ten times, therefore, we obtained ten modified sets of measurements and thus ten possible values of λ, β and a/b for each asteroid. We considered the parameter well enough determined when the maximum difference among ten obtained values was: $\leq 50°$ for λ; $\leq 30°$ for β; ≤ 0.25 for a/b. This was satisfied for 3930 asteroids in case of λ, for 4215 asteroids in a case of β and for 3819 asteroids in a case of a/b. For these asteroids (with well-determined parameters) we calculated the mean values of the largest differences. These are different from the maximal allowed differences, because for some asteroids the maximum difference among ten values could be better. For λ, the mean value is $30°$, for β it is $16°$ and for a/b it is 0.18. In next sections of this chapter, we consider these values as the uncertainties of derived parameters for individual asteroids. Even though the uncertainties are large, working with asteroid populations should smear them and the results should hold in a statistical sense.

---

[1]We did not use data for all asteroids, because it would be very time-consuming.
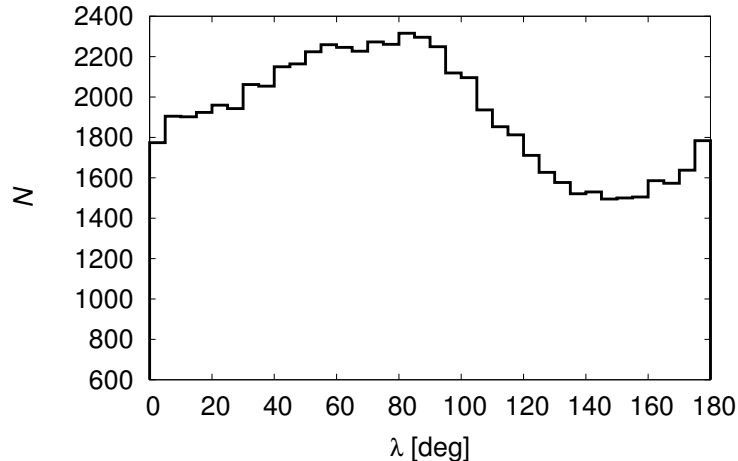
Figure 3.6: Distribution of pole longitudes λ derived for 69 053 asteroids from the Lowell Observatory photometric database with model noise $\sigma_{\mathrm{model}} = 0.06$ and weight $w = 5$. The values of λ larger than 180° map to the values $\lambda - 180°$, because of the symmetry of the model.

3.4 Distributions of pole longitudes λ

After testing our model we applied it to the photometric data for 69 053 asteroids from the Lowell Observatory database. For this sample, we used our model with weight $w = 5$, model noise $\sigma_{\mathrm{model}} = 0.06$, and data noise σ_L calculated for each asteroid according to the rule described above.

The resulting distribution of λ is shown in Fig. 3.6. As we can see, it is clearly nonuniform with an excess of asteroids with λ from 40° to 100° and with a minimum for $\lambda \sim 150°$. We calculated the Kolmogorov-Smirnov (KS) test for this distribution if it is compatible with a uniform one and we found that the probability Q_{KS} that they belong to the same parent distribution is $< 10^{-16}$. A similar result was obtained by Bowell et al. (2014), who estimated pole longitudes λ for more than 350 000 main-belt asteroids using the same dataset but different method, precisely the magnitude method (Magnusson, 1986) based on the variation of brightness L with λ, which can be fitted by a sinusoid curve. Essentially, from the maximum of the curve, which corresponds with the spin axis pointing either toward the Earth or opposite from the Earth, they found λ.

Up to now, there is no satisfactory explanation of such nonuniformity in the distribution of pole longitudes λ. We considered the observational and method biases described in Marciniak et al. (2015) and Santana-Ros et al. (2015), nevertheless, we found these do not influence our results. Therefore, we searched for some other observational biases and geometrical and dynamical effects as well.

3.4.1 Searching for an explanation

Correlation with heliocentric ecliptic longitudes of observations. First, we studied the influence of the geometry of observation, specifically the correlation between the calculated values of λ and the heliocentric ecliptic longitudes λ_{obs} of observations. We used data for the first 10 000 asteroids from the Lowell database. Such sample is large enough to show the nonuniformity in λ distribution. For
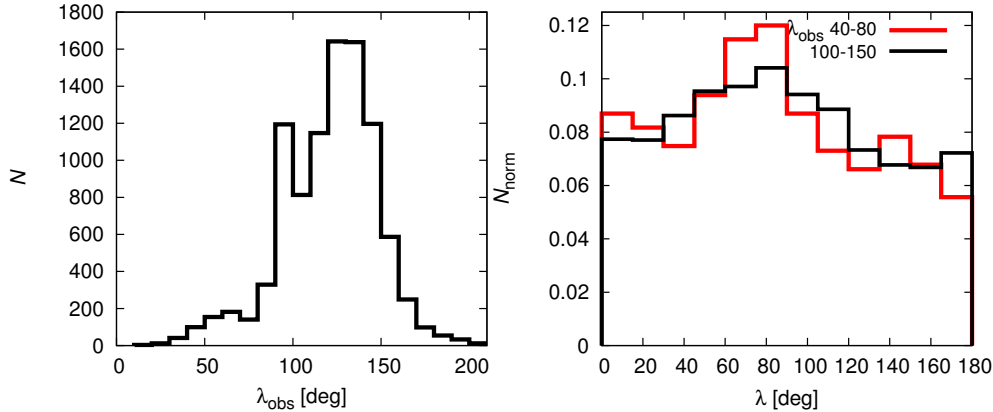
Figure 3.7: Left: Distribution of the mean values of heliocentric ecliptic longitudes λ_{obs} of observations. The shown distribution contains data for 9680 asteroids from the Lowell database. Right: Distributions of pole longitudes λ for two different intervals of λ_{obs}. The KS test did not find these distributions to be significantly different.

each asteroid apparition containing at least 20 measurements we calculated the mean value of λ_{obs}. If the number of apparitions was at least 5, we calculated the overall mean value of λ_{obs} for a given asteroid.

We found that the preferred values of λ_{obs} are $100° - 150°$ as shown in Fig. 3.7. Nevertheless, when we compared distributions of pole longitudes for asteroids observed at the privileged λ_{obs} (6437 bodies) and at $\lambda_{\mathrm{obs}} = 40° - 80°$ (575 bodies) we did not find any significant difference (see Fig. 3.7). The result of the KS test was $Q_{\mathrm{KS}} = 0.53$ meaning that there is no statistical difference between these two intervals of λ_{obs}.

Galactic plane bias. Next, we tested the influence of the measurements near the Galactic plane. The stellar background there is more dense and thus the photometric measurements may have higher uncertainties. We thus eliminated the observations with Galactic latitudes $|b| < 10°$ and repeated the analysis (for one asteroid there were on average about 6% less points). We again compared derived values of λ with λ's from the DAMIT database. The differences were comparable with values for the model with Galactic plane included. The nonuniformity in λ was, however, even slightly larger as we can see in Fig. 3.8. This result could suggest, on the contrary, that the nonuniformity of λ distribution could be caused by the shortage of observations near the Galactic plane. However, if such a bias could influence our results, it would have been seen in our test with synthetic data (Sec. 3.2), since the geometry of observations was kept unchanged. Nevertheless, the resulting distribution of pole longitudes was uniform, therefore, we believe our results are not influenced by such bias and we had to look for another explanation.

Correlation with the longitude of ascending node Ω. We also studied the role of the orbital longitude of node Ω. We tested a possible correlation between
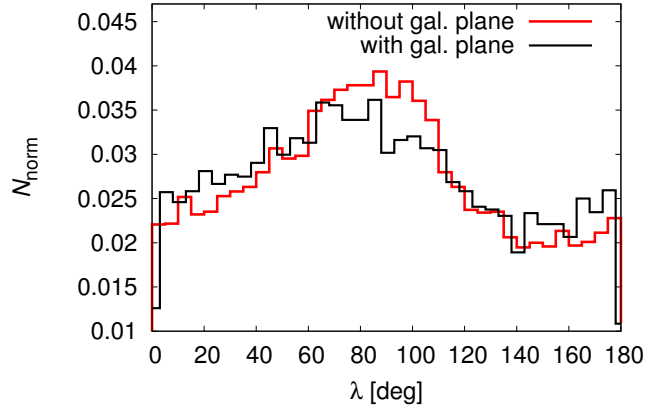
Figure 3.8: The distribution of λ computed from photometric observations including the Galactic plane (black line, 9679 asteroids) and without the Galactic plane (red line, 9653 asteroids).

asteroid's pole longitude λ and Ω. The orbital data were taken from the AstOrb catalog. Figure 3.9 shows the distribution of Ω values for 566 089 multi-opposition orbits of main-belt asteroids.

First, we focused on the data in the ecliptic reference system. The Ω values show an overpopulation centered at $\sim 100°$, and underpopulation shifted by about $180°$, i.e., centered at $\sim 270°$. This result is not new (see, e.g., JeongAhn and Malhotra, 2014, and references therein) and the reason for this nonuniformity in Ω is due to planetary perturbations. The asteroids' inclination I and node Ω evolve in time such that $\sin I \exp(\iota\Omega)$ can be represented with a Fourier series $\simeq \sum A_k \exp(\iota(s_k t + \Phi_k))$, with the first few terms typically dominating (e.g., Brouwer and Clemence, 1961). The first term, $k = 0$, is called proper as it is determined by the initial orbital conditions of each asteroid. The phase Φ_0 of the proper term is uniform at a current epoch $t = 0$. The other terms in the Fourier representation of $\sin I \exp(\iota\Omega)$ are due to planetary perturbations and they are common to all asteroids in the belt. In the ecliptic reference system, one of these planetary terms has zero frequency and amplitude corresponding to inclination of about $1.58°$. This is the tilt between the Laplace plane, normal to the planetary total angular momentum, and the plane of ecliptic. The common phase of this term, ascending node of the Laplace plane, is $\simeq 100°$ (see, e.g., (Dermott et al., 2002)). Further planetary terms have non-zero frequencies and smaller amplitudes, with the leading term due to the s_6 frequency and amplitude between $\simeq 0.8°$ and $\simeq 1°$ (depending on the mean heliocentric distance). The present phase Φ_6 of this term is $\simeq 305°$ in the ecliptic system. Therefore, the s_6 term partially, but not entirely, compensates the zero-frequency term. Other planetary terms have smaller amplitudes and may be ignored in our discussion.

The bottomline of this analysis is as follows. In the ecliptic system, the proper term of all asteroids in the $\sin I \exp(\iota\Omega)$ complex-plane representation is presently off-centered by about a degree towards the longitude $\simeq 100°$. Since asteroids are uniformly distributed along the proper-term circle, the planetary terms present compositely forcing which makes the value of osculating nodal longitude in the ecliptic coordinates non-uniform with a slightly preferred values near $\simeq 100°$ (Fig. 3.9). The situation in the Laplace reference frame is the same
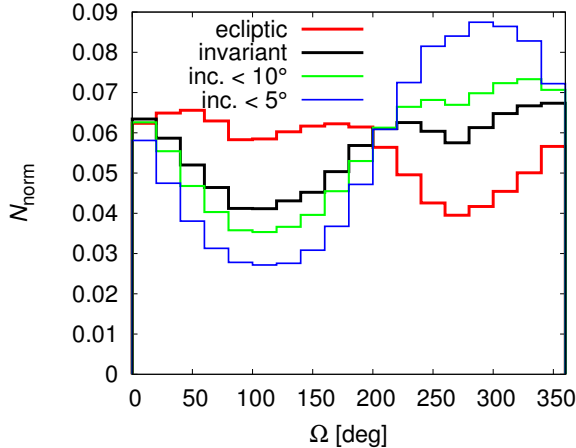
Figure 3.9: Distribution of the osculating longitudes of ascending node Ω (from AstOrb catalog) for MBAs. The red curve represents the distribution in the ecliptic plane; the black curve indicates the distribution in the invariant (Laplace) plane. The green and blue lines represent the distribution in the invariant plane for asteroids with the inclination of the orbit $I < 10°$ and $I < 5°$, respectively.

with the only difference consisting in the absence of the zero-frequency term in the Fourier representation of $\sin I \exp(\iota\Omega)$. Because the longitude origin in the Laplace plane was deliberately chosen to make only a small difference between the nodal longitudes in both reference frames (the ecliptic and Laplace), the proper term is now shifted by little less than a degree towards a longitude $\simeq 290°$. Therefore, this is also the preferred value of the asteroids' osculating longitude of node in the Laplace frame (Fig. 3.9). Obviously, the effect becomes larger for small-inclination orbits (i.e., whose proper inclination value is small), as also shown in Fig. 3.9. In next few tests we will examine, whether the nonuniform distribution of λ is not a simple implication of the known nonuniformity in Ω.

First, we ran the following experiment. We divided asteroids according to their value of Ω to 18 equal bins (each 20° wide). We found the bin that contains the smallest number N of asteroids, and we randomly selected N objects from all other bins. In other words, we had a sample of asteroids with a uniform distribution of ascending nodes. The distribution of pole longitudes λ for this subsample was, however, still nonuniform, resembling that in Fig. 3.6. The KS test of compatibility of the λ distributions obtained from our subsample and the whole sample of asteroids gave us a likelihood $Q_{KS} \simeq 0.90$ that they have the same parent distribution. We repeated this experiment several times, creating new subsamples, and obtained the same results. We also ran the same experiment in the Laplace reference system, but the choice of reference plane does not influence the result. These experiments suggest that the nonuniform distribution of orbital nodes does not play a fundamental role in the nonuniform distribution of longitudes of spin axis.

Nevertheless, we would expect some relation between Ω and λ should exist. For instance, plotting λ distributions for asteroids in each of the Ω bins described above, we obtained data shown in Fig. 3.10. As we can see, in each of the bins of restricted Ω values, distribution of pole longitude peaks at $\simeq (\Omega - 90°)$. This is actually understandable in the simplest model, in which the spin axis of each
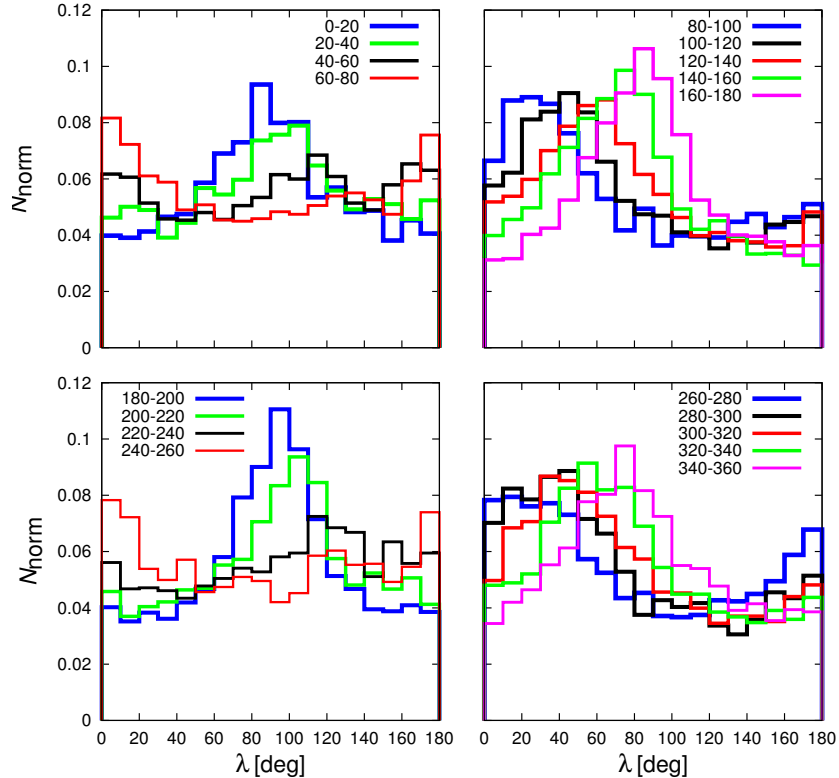
Figure 3.10: Distributions of pole longitudes λ for different intervals of longitude of ascending node Ω. Each distribution has a maximum for $\sim (\Omega - 90°)$.

asteroid just uniformly precesses about the normal to its osculating orbit due to solar gravitational torque. We have quantitatively tested how much this simple geometrical effect of such precession could contribute to the observed dependence of pole longitude λ on node Ω by running the following experiment: We assumed the pole position in the moving orbital plane is set with the obliquity ϵ and we chose the inclination of orbit I and the longitude of ascending node Ω. This initial set up was changed several times, specifically, we tested values of inclination $\sin I = 0.10, 0.15, 0.30$, values of node $\Omega = 10°, 170°, 250°$ and values of obliquity $\epsilon < I$, $\epsilon > I$. Assuming a simple regular precession, we randomly picked many values of the longitude λ', uniform in $0°$ to $360°$. We then transformed poles (λ', ϵ) to the ecliptic system:

$$\begin{pmatrix} \cos\lambda\cos\beta \\ \sin\lambda\cos\beta \\ \sin\beta \end{pmatrix} = R_z(-\Omega)R_x(-I) \begin{pmatrix} \sin\lambda'\sin\epsilon \\ \cos\lambda'\sin\epsilon \\ \cos\epsilon \end{pmatrix}, \qquad (3.18)$$

determined appropriate λ and constructed a model distribution of the ecliptical longitudes. Results of these simple simulations satisfied our hypothesis of geometrical effect; for $\epsilon < I$, the distribution of λ was only a tight interval of values near $\simeq (\Omega - 90°)$, and for $\epsilon > I$, the λ values spanned the whole interval from $0°$ to $360°$, but with a peak at $\simeq (\Omega - 90°)$ (see Fig. 3.11).

After these simple tests that confirmed our hypothesis we performed a more realistic simulation. Instead of only a single input value of I and Ω, we used a real distributions represented by the sample of 69 053 bodies for which we determined
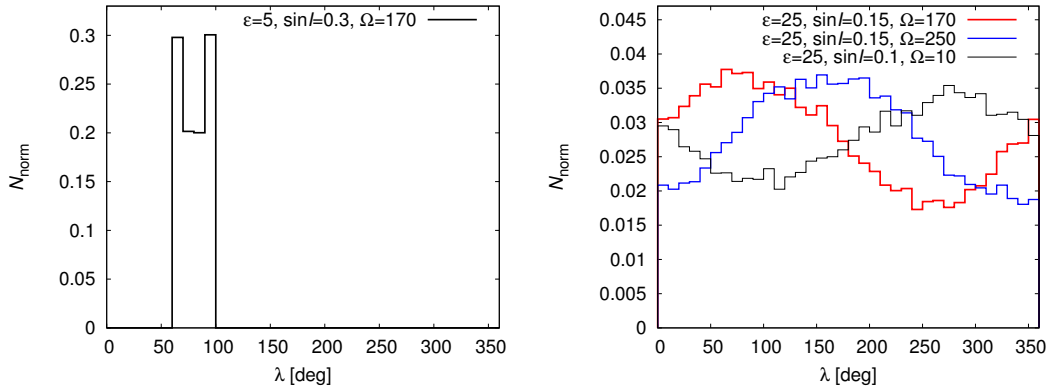
29

Figure 3.11: The results from the simulations of the precession of the spin axis. Left: The distribution of the ecliptical longitudes λ of the spin axis that precesses about the normal to its osculating orbit for an asteroid with obliquity $\epsilon < I$. Right: The same, but for an asteroid with $\epsilon > I$.

the λ distributions from Lowell photometric data. For each asteroid we randomly picked value of λ', uniform in 0° to 360°. As to the obliquity, we assigned to each asteroid a fixed value $\epsilon = 2°$. Such choice of obliquity may seem extreme, but our sample is dominated by small asteroids that have spin axes evolved by the YORP effect, i.e., small obliquities. Then we applied the Eq. 3.18. The resulting distribution of λ is shown in Fig. 3.12. We can see it is nearly uniform, with only a very slight excess of bodies at $\simeq 100°$. The probable explanation of this result is that the center of maximum of Ω distribution ($\simeq 100°$) and the deep minimum of its distribution ($\simeq 270°$) are basically 180° apart, which in our operation brings them together in contribution to the λ distribution. We tried several more initial condition, but only when we limit Ω to the narrow interval (in the most extreme case to a single value for all objects), we obtained λ distribution significantly different from uniform. Our results suggest that the projection of the spin axis precession can partly explain the nonuniform λ distribution, but there must be some other dynamical or observational effects because the simple projection model together with the nonuniformity of the ecliptic Ω values and other assumptions of our model cannot explain the nonuniformity in pole longitudes.

However, the evolution of pole orientation in the orbit frame may be much more complicated than just a simple steady precession about the orbital angular momentum vector due to a possibility of resonant, spin-orbit effects described by Cassini dynamics (e.g., (Colombo, 1966); (Henrard and Murigande, 1987); (Vokrouhlický et al., 2006)). In fact, a part of the Koronis family, the so called Slivan sample, has actually been identified as being captured in s_6 Cassini resonance resulting in a common orientation of their pole longitudes near the stationary point at $\lambda \simeq 35°$ (Vokrouhlický et al., 2003).

However, we verified that such resonant effects are not able to explain the nonuniformity in the distribution of λ. First, if the capture in the aforementioned Cassini resonance played a dominant role population-wise, the λ distribution would be peaked at the stationary point of the resonance, which is shifted by some $35° - 40°$ from the maximum seen in Fig. 3.6. Next, Vraštil and Vokrouhlický (2015) have shown that the capture in this resonance is generally unstable, especially in the inner part of the main belt. They also found that its phase vol-
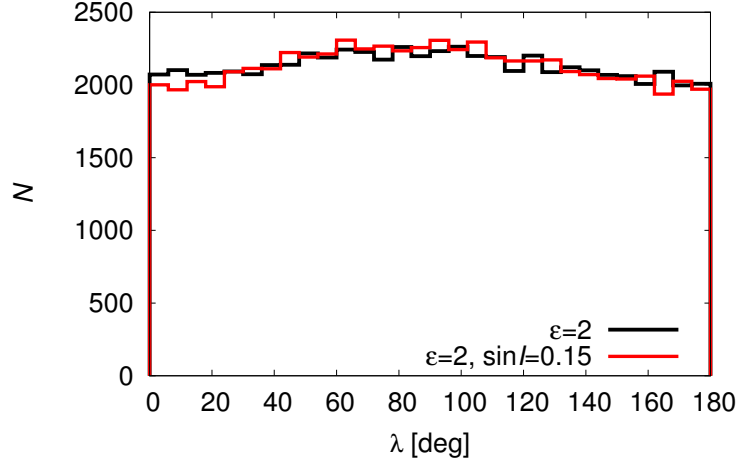
Figure 3.12: The same as in Fig. 3.11, but with real distribution of nodes Ω defined by 69 053 asteroids for which we determined λ distribution shown in Fig. 3.6. The distribution plotted by black line was obtained by using the real distribution of $\sin I$, the distribution plotted by red line was obtained by using a single value $\sin I = 0.15$.

ume is small (few percent at maximum), which implies that expecting the spin pole located in this resonance by chance is very small. In order to verify these preliminary conclusions, we used the software described in Vraštil and Vokrouhlický (2015) to probe the expected effect. This is basically a much more sophisticated variant of our previous Monte Carlo experiment in which we assumed a steady precession in the orbit frame. We numerically propagated orbit and spin evolution of the first 10 000 main belt asteroids for tens of millions of years (with the YORP effect included) and monitored the distribution of their pole longitudes. To the sample of asteroid we gave random initial rotation state parameters, such as rotation period pole orientation, and dynamical ellipticity. We found that the sample quickly forgets the initial conditions and fluctuates about a steady-state situation with basically uniform distribution of ecliptic longitudes of spin axes. We repeated the numerical experiment several times with different initial conditions but always obtained very similar results.

Synthetic data with narrow range of Ω. When studying the dependence of λ distribution on ascending node Ω we noticed that for two Ω intervals, $40°$ to $60°$ and $220°$ to $240°$, the distributions are flatter than for other Ω intervals. These two intervals are approximately $\pm 90°$ from the privileged ecliptic longitudes of observation λ_{obs} (see Fig. 3.7). That could suggest the pole longitudes are less constrained since we observed the asteroids mostly above or bellow the ecliptic.

To test this hypothesis, we performed the following test. We created synthetic data as in Sec. 3.2, but for all asteroids we chose obliquity from $\epsilon = 0°$ to $5°$ and pole longitude (in the asteroid coordinate system) uniformly distributed. Then we calculated the ecliptic coordinates of the spin axes $\lambda_{\mathrm{initial}}$, β_{intial}, selected objects with (i) $\Omega = 40° - 60$; (ii) $\Omega = 130° - 150°$; (iii) $\Omega = 220° - 240°$ and (iv) $\Omega = 340° - 360°$ and ran our model. The initial and calculated λ distributions for each of the tested intervals of Ω are shown in Fig. 3.13. We can see that
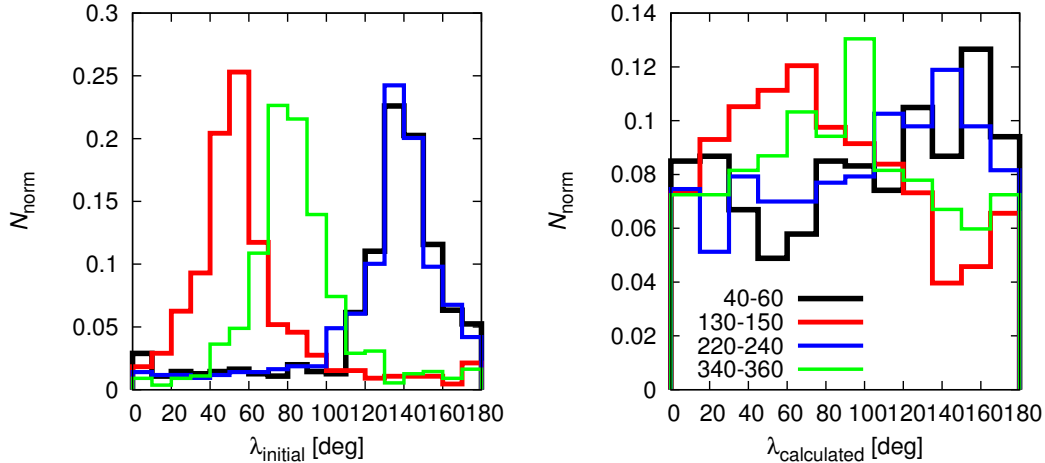
Figure 3.13: Test with synthetic data. Left: Distribution of initial pole longitudes λ_{initial} of asteroids with obliquities from $\epsilon = 0°$ to $5°$ for individual intervals of ascending nodes Ω. Right: Distributions of pole longitudes calculated with our model for appropriate Ω intervals. We can see that for each Ω interval, our model behaves similarly, distributions are mutually shifted but have similar shapes.

the information about the initial λ distribution is partially lost, but for each Ω interval to the same extent, i.e., the distributions have similar shapes, and are only mutually shifted.

The calculated distributions are flatter and their peaks are not so pronounced as in Fig. 3.10. This is possibly due to our choice of asteroid obliquities, which were too extreme. Thus, we performed a second test with the same initial conditions but with $\epsilon = 5° - 10°$. The results are in Fig. 3.14. The distributions are not improved in comparison to the previous test and again we do not see any differences between individual intervals of Ω except the mutual shift. In principle, it would be possible to choose such distributions of ϵ and λ_{initial} and their correlations with Ω distribution to obtain the nonuniform $\lambda_{\text{calculated}}$ distribution as shown in Fig. 3.6. However, we would not be able to explain, why the considered quantities should be bound by such correlations and thus, these tests would not provide us with any physical explanation of the problem.

Distribution of λ_{DAMIT}. As an independent check, we also plotted the distribution of λ for asteroids in DAMIT database to find if a different method applied to a different data would provide the same λ distribution and also to test if there is some difference between λ from interval $0° - 180°$ and $180° - 360°$. In Fig. 3.15, there is a distribution for 964 models from DAMIT (for asteroids with two different models available, we chose the first one). We can see that the nonuniformity is significant and in accordance with Fig. 3.6. The distributions in both intervals of λ are quite similar, in fact, when we transformed $\lambda \geq 180°$ into the interval $0°$ to $180°$ and compared with the group with $\lambda < 180°$ using the KS test, we found $Q_{\text{KS}} = 0.346$, which means no statistical difference. Therefore, the distributions limited to the interval of λ from $0°$ to $180°$ are reliable in a statistical sense.
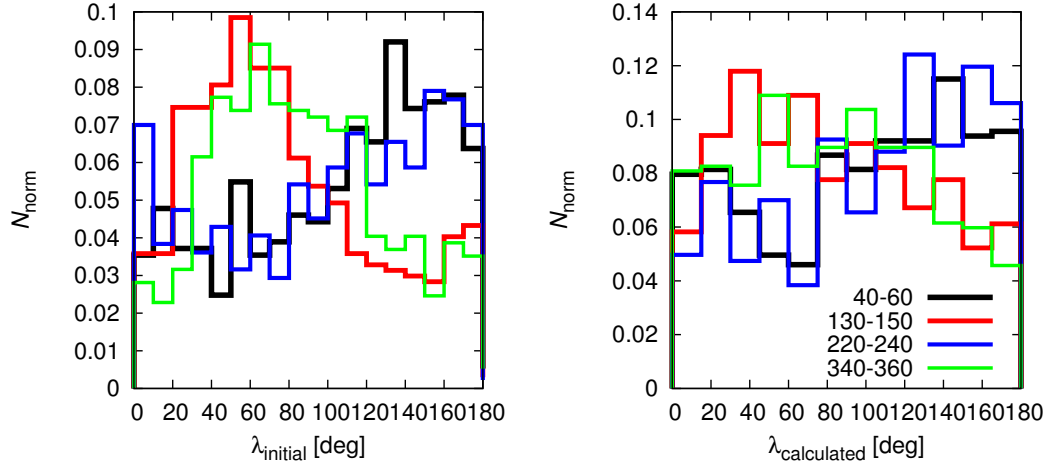
Figure 3.14: The same as in Fig. 3.13 but with initial obliquities from $\epsilon = 5°$ to $10°$. Again, there are no significant differences between individual Ω intervals.
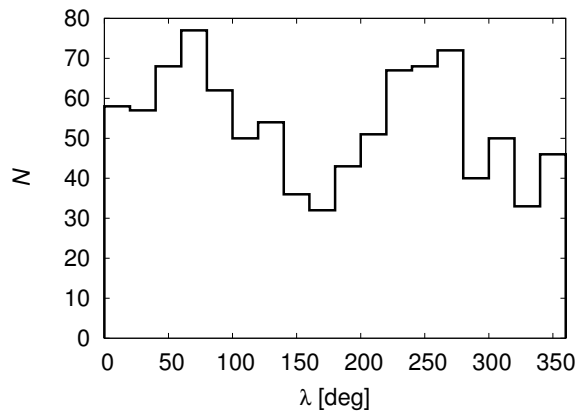

Figure 3.15: Distributions of pole longitudes λ of 964 DAMIT models. The intervals $\lambda = 0°$ to $180°$ and $180°$ to $360°$ are not statistically different.
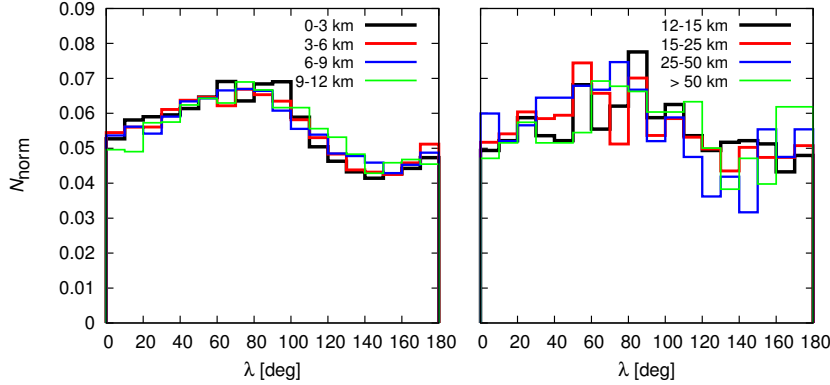
Figure 3.16: Distributions of pole longitudes λ for groups of asteroids with different intervals of diameter D. Distributions are not statistically different.

population	N	population	N
$0-3$ km	15 235	Flora	4 098
$3-6$ km	28 686	Massalia	434
$6-9$ km	12 618	Nysa/Polana	3 042
$9-12$ km	5 322	Vesta	3 788
$12-15$ km	2 127	Eunomia	2 115
$15-25$ km	2 069	Gefion	783
$25-50$ km	884	Maria	832
> 50 km	679	Koronis	1 616
		Eos	2 764
C class	4 550	Hygiea	746
S class	6 660	Themis	1 587

Table 3.1: Number of asteroids in several studied populations. The family membership was taken from Nesvorný et al. (2015).

3.4.2 Distribution of λ for groups of asteroids

Our next step was to study the distributions of λ for various groups of asteroids, specifically for asteroids with different sizes, different spectral types, individual dynamical families, and asteroids located in different parts of the main belt. Distributions were compared using the KS test.

Asteroids with different sizes. We divided asteroids into eight groups according to their diameters D: 0–3 km; 3–6; 6–9; 9–12; 12–15; 15–25; 25–50; and 50–1000 km; the number of asteroids decreases with larger diameters, therefore, we chose wider ranges of bins (the exact numbers of asteroids in these populations are listed in Table 3.1). We preferentially used diameters derived from the observations of the WISE satellite (Masiero et al., 2011)[2]. For asteroids not included there, we used diameters from AstOrb catalog. Distributions of λ of these asteroid populations were compared with each other. We found that the differences are not significant, which means that the data do not reveal any strong dependence of λ on D. The distributions of λ are shown in Fig. 3.16.

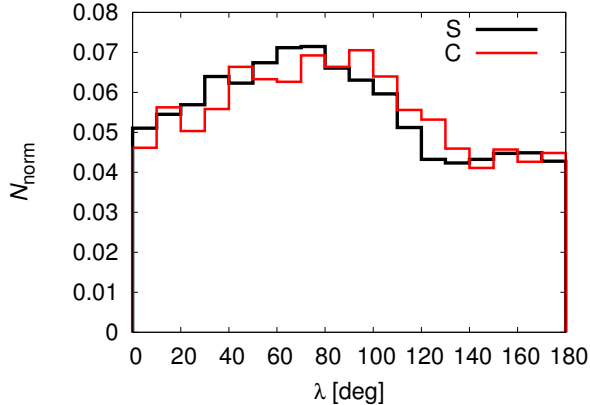[2]http://wise2.ipac.caltech.edu/staff/bauer/NEOWISE_pass1/.

Figure 3.17: Distributions of pole longitudes λ for taxonomic complex S (black line) and C (red line).

Taxonomic complexes. Next, we compared distributions of λ between asteroids belonging to the most common taxonomic complexes C and S. We assigned a taxonomic class to asteroids according to the SDSS-based Asteroid Taxonomy (Carvano et al., 2010). The result of the KS test, $Q_{KS} = 0.014$, does not indicate a significant difference between these two populations. Such value is usually considered small enough to signify relevant differences, nevertheless our model is calibrated by several parameters that influence the results. Thus, we require $Q_{KS} < 10^{-4}$ to claim that the two distributions do not belong to the same parent distribution. In Fig. 3.17 we can see there is only a small shift between the λ distributions of S and C complexes – the maximum for S complex is $\sim 70°$, for the C complex the maximum is $\sim 90°$. This difference is comparable with the uncertainty estimated by the bootstrap method, i.e., $30°$. The fact that the distribution of λ is independent of the sizes and taxonomic complexes actually simplified tests with other asteroid populations.

Different parts of the main belt. We also studied the distributions of pole longitudes for groups of asteroids located in different parts of the main belt. Specifically, asteroids with different inclinations $\sin I$, eccentricities e, and semimajor axes a of their orbits (we used osculating orbital elements from AstOrb). While our tests did not reveal the distribution of λ to be dependent on the eccentricity, we found that it is strongly dependent on the inclination. As is shown in Fig. 3.18, for $\sin I < 0.02$ there is a huge excess of asteroids with λ from $60°$ to $100°$, there are more than four times more bodies than for $\lambda \sim 150°$. With increasing I the maximum decreases and the minimum becomes shallow. This result is surprising and it actually goes against the ideas about simple geometrical (projection) effects discussed in Sec. 3.4.1, suggesting that perhaps some not yet identified dynamical effect influences the distribution of λ.

We also studied the dependence of the distribution of λ on the inclination of orbit in the invariant plane. Although the maximum of distribution for $\sin I < 0.02$ is slightly lower, there is still a strong dependence on the inclination.

Next, we constructed distributions of λ for individual Ω bins (as in Fig. 3.10) for asteroids with $\sin I < 0.04$. The peaks of all distribution correspond with the peak of the λ distribution for small inclinations (i.e., λ from $60°$ to $100°$).
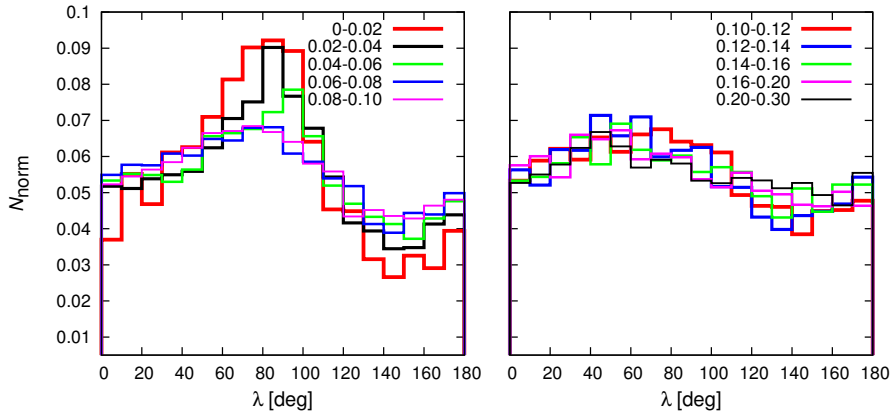
35

Figure 3.18: Distributions of pole longitudes for asteroids with different inclinations $\sin I$ of their orbits.
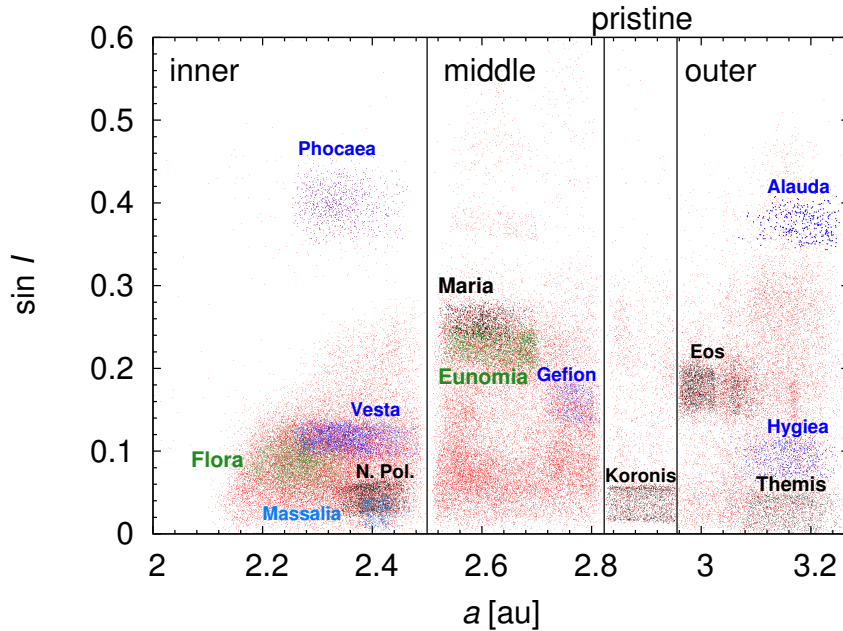

Figure 3.19: Four parts of the main asteroid belt defined according to the proper semimajor axis a (we used proper values of a and I from Asteroids Dynamic Site; (Knežević and Milani, 2003)). The locations of some more populous asteroid families are emphasized.
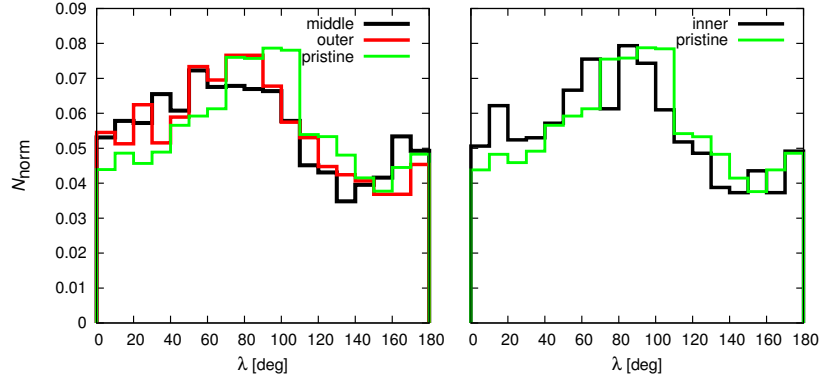
Figure 3.20: Distributions of λ for different parts of the main belt according to semimajor axis. The pristine zone is significantly different from the middle and outer belts. For the pair inner belt and pristine we cannot make a definitive conclusion.

This means that for orbits with small I, the dependence of λ on Ω is somehow suppressed.

We then constructed distributions of pole longitudes for asteroids with different semimajor axes a. We separated the main belt into four parts as shown in Fig. 3.19: the inner, middle, pristine and outer belt, which are naturally divided by low-order mean-motion resonances with Jupiter. To eliminate the dependence on the orbital inclination we divided asteroids of each part into bins of sines of inclinations (we used the same bins as in Figure 3.18) and we randomly chose such number of asteroids to have the same number of asteroids in corresponding bins of two populations. That way, we forced the $\sin I$ distributions for the two compared populations to be the same. The results of KS tests show that only the pristine zone, bracketed by the powerful mean-motion resonances 5:2 and 7:3 at $\simeq 2.82$ au and $\simeq 2.96$ au, has a significantly different distribution from the middle and outer belts ($Q_{\mathrm{KS}} < 3 \times 10^{-6}$); specifically, the nonuniformity is more significant in pristine zone than in other parts. For the pair inner belt and pristine zone, the KS test gives $Q_{\mathrm{KS}} = 0.00013$, which is on the edge of being significant. The distributions of λ are shown in Fig. 3.20. We can notice that the nonuniformity is larger than what is seen in Fig. 3.6. This is due to the fact that the pristine zone contains significantly more asteroids with small inclinations and as described above, we applied a correction to have the same number of asteroids in inclination bins. Therefore, also in other parts of the main belt, there are more low-inclination objects, which causes the stronger nonuniformity.

Dynamical families. Finally, we studied 13 major dynamical families shown in Fig. 3.19. The family membership of asteroids was taken from Nesvorný et al. (2015). Distributions of λ for individual families were compared with the distributions of corresponding backgrounds formed by asteroids that (i) do not belong to any of the studied families; (ii) are from the same part (inner, middle, pristine, and outer) as the family and (iii) have orbit inclinations from the interval defined by the members of the family. The KS test did not reveal any significant difference between any family and its background. We also compared families located
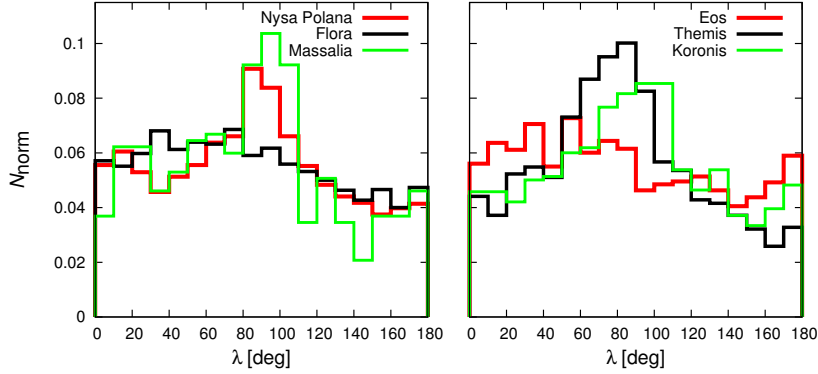
Figure 3.21: Distributions of λ for Flora, Nysa Polana, and Massalia (left) and for Eos, Themis, and Koronis (right). The individual distributions corresponds with the λ distributions for appropriate intervals of orbit inclinations.

approximately in the same interval of inclination (see Fig. 3.19) with each other, specifically: Themis with Massalia; Vesta with Eos, Hygiea and Flora; Hygiea with Flora; and Koronis with Nysa/Polana. Again, the KS test showed no differences for these pairs of families. The distributions of λ for six selected families are shown in Fig. 3.21. The differences we can see between the distributions are caused only by the dependence on the inclination of orbit.

We should note, that the strong maximum of the λ distribution between $\simeq (80° - 110°)$ in the Koronis family does not fit the interval of expected librators in Slivan states described by Vokrouhlický et al. (2003) which would be shifted by about 40° to 50° degrees toward lower values.

Rotational period. Using the LCDB database we divided main-belt asteroids into groups with different rotational periods P (we used only P with the quality U code 2-, 2, 2+, 3- and 3 that should be sufficient for a statistical study; Warner et al., 2009). To have a reasonable number of asteroids in individual groups we chose following ranges: $P < 3$ hours (609 asteroids); $3 - 6$ (2976); $6 - 10$ (2179); $10 - 40$ (2422); and $P > 40$ hours (811). For these groups we constructed distributions of λ. We found that for $P > 10$ h, the minimum around $\lambda = 140°$ becomes flatter and for $P > 40$ h, the minimum already vanished (see Fig. 3.22). This is an unexpected result that we are not able to explain.

Prograde and retrograde rotation. One limitation of our model is that we are not able to distinguish between prograde and retrograde rotators, it gives us only the absolute value of β. However, it could be useful to check if the distribution of pole longitude λ differs for populations with different sense of rotation. Therefore, we divided 964 asteroids from DAMIT database according to their sense of rotation: there are 454 prograde rotators and 510 retrograde rotators. We constructed appropriate distributions of λ, which are shown in Fig. 3.23. We can see, that the distributions are not different, the KS test gave us the probability that the distributions belong to the same parent distribution $Q_{KS} = 0.59$.

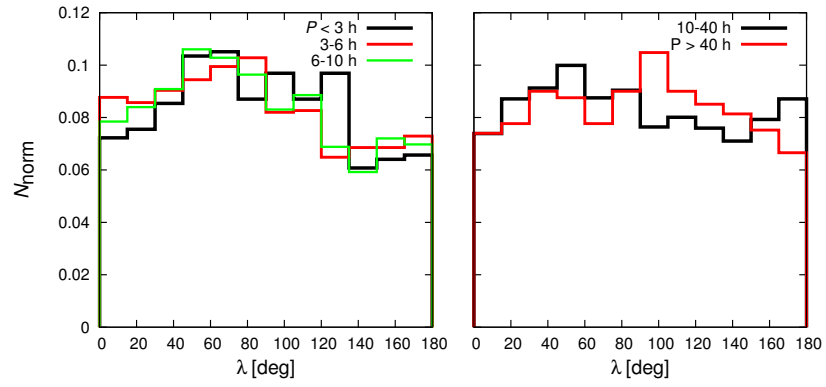**Figure 3.22:** Distributions of λ for asteroids with different rotational periods P.
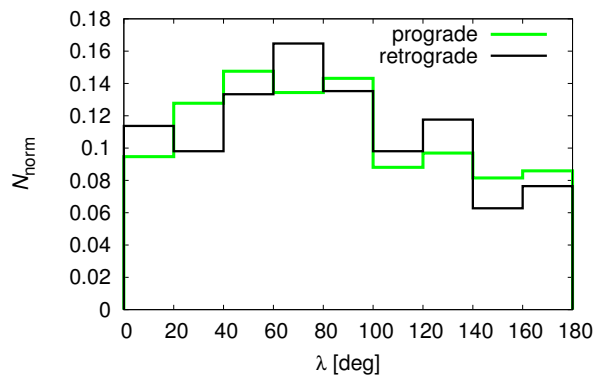

Figure 3.23: Distributions of λ for prograde and retrograde asteroids based on models from DAMIT. Distributions are not significantly different.
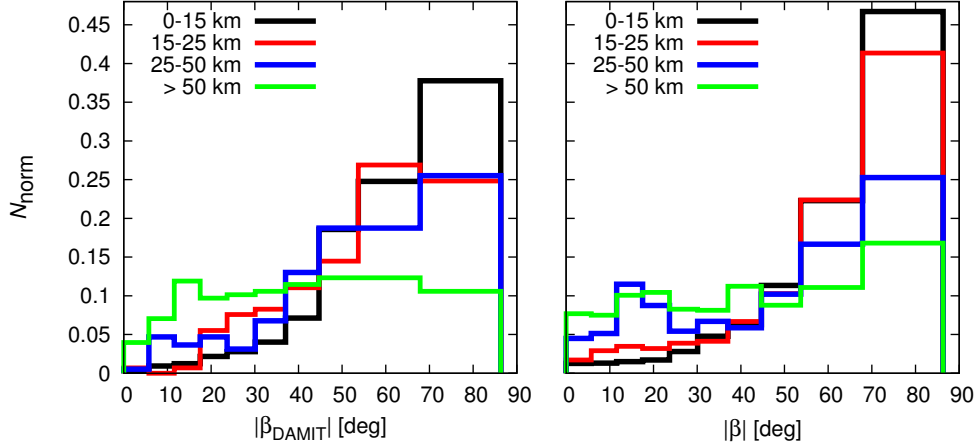
Figure 3.24: Left: Distribution of pole latitudes $|\beta|$ from DAMIT database for 964 asteroids divided to populations with different sizes. Right: Distribution of $|\beta|$ derived with our model for 69 053 asteroids using the data from the Lowell database. Bins are equidistant in $\sin\beta$. Distributions are debiased, i.e., divided by the synthetic distribution with noise 0.15 and model noise 0.06 (Fig. 3.4 right panel, black curve).

3.5 Distributions of pole latitudes β

In this Section, we study the distribution of absolute value of ecliptical latitude $|\beta|$ for groups of asteroids. Since the distribution calculated for the synthetic data was not uniform, the determined latitudes are affected by the method bias. Therefore, all constructed distributions of $|\beta|$ are divided by the distribution for synthetic data with noise 0.15 and model noise 0.06 (Fig. 3.4 right panel, black curve). This is the simplest debiasing procedure we can use.

Asteroids with different sizes. First, we studied the dependence of pole latitude $|\beta|$ on size and tried to confirm and extend the result of Hanuš et al. (2011), who found the dependence of the distribution of β on the diameter D (for $D \lesssim 30$ km asteroids they found a strong preference for pole orientation near the pole of the ecliptic). In agreement with findings of Hanuš et al. (2011), we found a visible depopulation of spin axes close to the ecliptic plane with decreasing diameter as shown in Fig. 3.24 on the right. The same figure on the left shows distributions of $|\beta|$ inferred from DAMIT models. We can see that, in comparison with models from DAMIT, our model overestimates high $|\beta|$ bins, however, the trend for decreasing diameter of asteroids is obvious.

This is yet another interesting hint about the origin of the nonuniformity of λ distribution. The affinity of latitudes toward extreme values for small asteroids clearly shows that the YORP effect has been affecting the population in a size-dependent way, as predicted by the theory. However, the distribution of the longitudes does not indicate this size-dependency, implying the YORP effect is not the primary mechanism in the longitude story. Indeed, the theory of the YORP effect alone so far has not predicted any significant effects for the pole longitude.
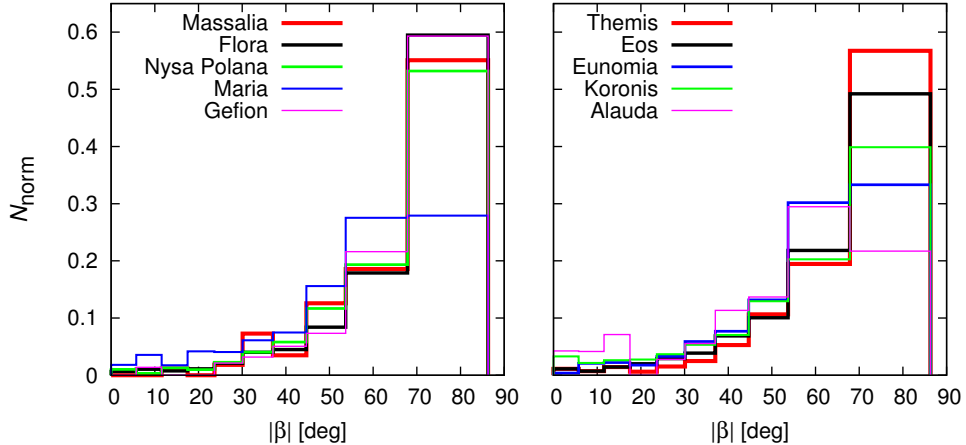
Figure 3.25: Debiased distributions of $|\beta|$ for some of the most populous dynamical families. Bins are equidistant in $\sin\beta$.

Dynamical families, inclination dependence.   Next, we constructed distributions of $|\beta|$ for asteroid families. We included only asteroids with diameter $D < 20\,\mathrm{km}$ to eliminate the above described dependence on diameter. Resulting distributions are shown in Fig. 3.25. The high-inclination families in the middle belt, Eunomia and Maria, have significantly smaller number of spin axes with $|\beta| \gtrsim 70°$ and more asteroids with $|\beta| \lesssim 70°$. Even more significant is that for the outer-belt family Alauda.

The shown distributions of pole latitude $|\beta|$ of asteroid families correspond with distributions of $|\beta|$ of populations with different inclination of orbits plotted in Fig. 3.26. To suppress this dependence we should rather plot the distributions of obliquities. The quantity influenced by the YORP effect is the obliquity ϵ, not the latitude β (only for inclination $I = 0°$ is $\epsilon = 90° - \beta$). Unfortunately, we are not able to compute obliquities, because our model provides longitudes only in the interval $\langle 0°, 180° \rangle$.

Nevertheless, it is possible to test the respective relation between ϵ and β on the synthetic data with isotropic distribution of spin axes described in Section 3.2. To this aim, we calculated obliquity for each asteroid in our synthetic sample as

$$\cos\epsilon = \sin I \sin\Omega \cos\lambda \cos\beta - \sin I \cos\Omega \sin\lambda \cos\beta + \cos I \sin\beta. \qquad (3.19)$$

We chose only asteroids with $\cos\epsilon > 0.866$ (the spin axes $\lesssim 30°$ from the pole of ecliptic). Then we ran our model to get the new values of pole latitudes β. The results were divided into the inclination bins and for each of them we plotted the distributions of $|\beta|$. As we can see in Fig. 3.27, for $\sin I < 0.02$, the majority of objects have $\beta > 60°$, which corresponds with the original obliquities. With growing inclinations, the number of bodies with $\beta < 60°$ is growing and the information about the original obliquities is practically lost. Thus, we have to be careful when analyzing the results since the debiasing distribution derived in Sec. 3.2 includes the whole population. However, for the individual inclination intervals the debiasing distributions could be different.

The two families that do not follow the distribution of the corresponding background are Gefion in the middle belt and Koronis in the pristine zone. The result of the KS test suggests that Gefion could be different from its background,
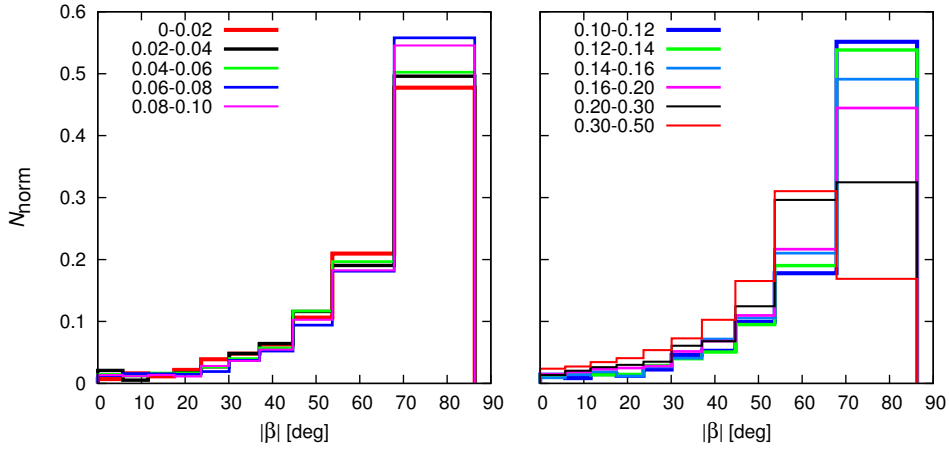
41

Figure 3.26: Debiased distributions of $|\beta|$ for groups of asteroids with different inclinations of orbits $\sin I$. Bins are equidistant in $\sin \beta$.
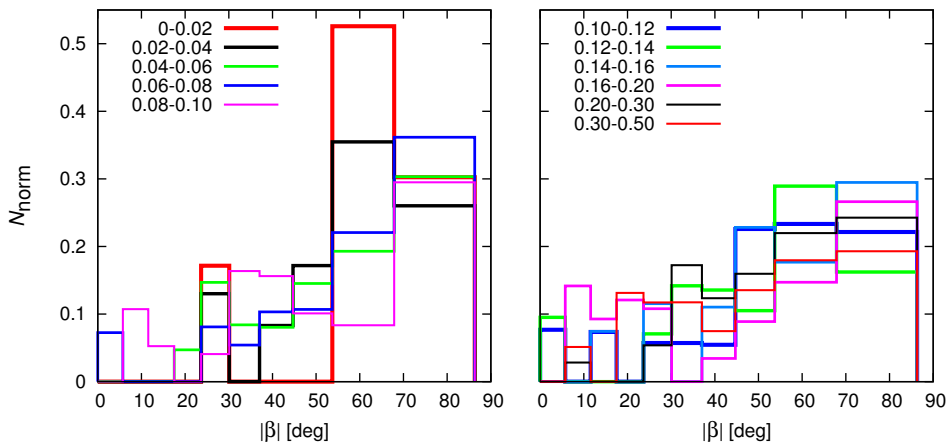

Figure 3.27: The same as Fig. 3.26 but for a synthetic data created in Sec. 3.2 from which we chose only asteroids with obliquity $\cos \epsilon > 0.866$.
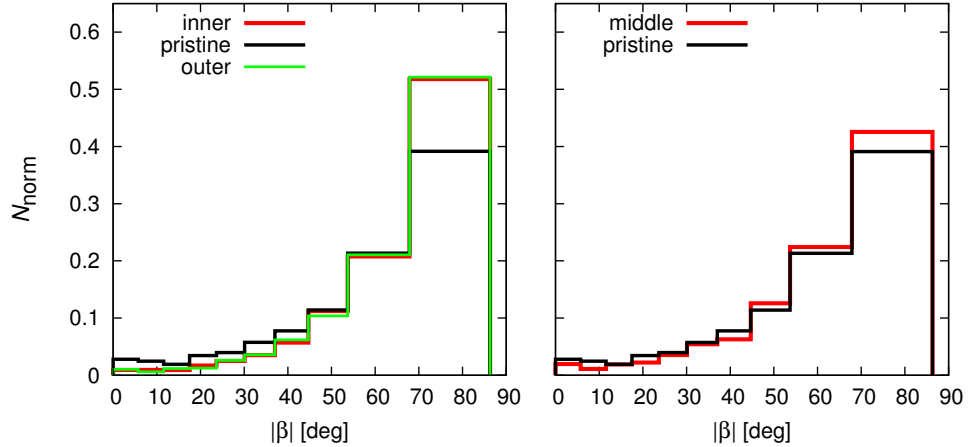
Figure 3.28: Distributions of $|\beta|$ for groups of asteroids with different semimajor axes. The inner and outer belts do not differ and both are significantly different from the middle belt and pristine zone.

$Q_{\mathrm{KS}} = 0.0017$ is on the edge of being significant. Nevertheless, if we compare Gefion with the objects with appropriate orbit inclinations ($0.16 < \sin I < 0.2$), we obtain $Q_{\mathrm{KS}} < 10^{-8}$. We also compared Gefion with the Eos family, which is located approximately at the same interval of inclination, and obtained $Q_{\mathrm{KS}} = 0.00068$, which gave us no definite answer. Koronis is not significantly different from its background, however, when we compared it with corresponding interval of $\sin I$ ($0.02 - 0.06$, see Fig. 3.19), the value of Q_{KS} is almost zero. Such results suggest, that the whole pristine zone could be different from the rest of the main belt.

Different semimajor axes, taxonomic classes. Previous results motivated us to compare also distributions of β for asteroids in different parts of the main belt according to their semimajor axes a. Again, we used only bodies with $D < 20\,\mathrm{km}$, and moreover, we eliminated the dependence on inclination in the same way as when we studied the distributions of longitudes λ. The results are shown in Fig. 3.28. The inner and outer belts have practically the same distribution of β ($Q_{\mathrm{KS}} = 0.28$) and both are significantly different from the middle belt and pristine zone ($Q_{\mathrm{KS}} < 10^{-11}$). For the pair middle belt and pristine zone, the KS test gave us the probability $Q_{\mathrm{KS}} = 0.0225$. These two parts contain significantly less objects with β close to 90° than inner and outer belt. In contrary, the Gefion family, located in the middle belt, contains more objects in the last bin of β distribution, and is therefore exceptional in two ways: (i) it is different from objects with the same interval of inclinations and (ii) from other objects in the middle belt ($Q_{\mathrm{KS}} < 10^{-7}$).

Though we did not assume the distribution of β to be different for asteroids with different taxonomic classes, we performed also this test for the sake of completeness. The probability that the taxonomic classes S and C have distributions of β that are both drawn from the same parent distribution is $Q_{\mathrm{KS}} = 0.46$.
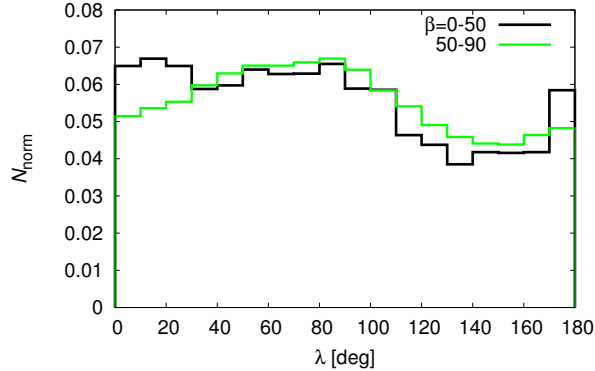
Figure 3.29: Distributions of λ for asteroids with pole latitude $|\beta| = 0°$ to $90°$ and $|\beta| = 50°$ to $90°$.

Distributions of λ for different β values. Finally, we checked the correlation of λ and β. We thus divided asteroids to two groups: 9 191 asteroids that have $|\beta|$ from $0°$ to $50°$ and 59 721 asteroids that have $|\beta|$ from $50°$ to $90°$. The result of the KS test ($Q_{KS} < 10^{-9}$) shows that the distributions are significantly different. As we can see in Fig. 3.29, the distribution of λ for lower values of $|\beta|$ is uniform from $\lambda = 0°$ to approximately $100°$ and then, there is a deep minimum around $140°$, while the distribution for $|\beta| > 50°$ is similar as the distribution for the whole main belt.

3.6 Distributions of shape elongations a/b

In this section, we study ellipsoidal shapes of asteroids, specifically the ratios of axes a/b and b/c derived from our model. As described in Sec. 3.2, we tested our model on synthetic data with assumed noise level $\sigma_L = 0.15$. The values of ratios a/b and b/c obtained with our model were compared with values from DAMIT models derived from the principal moments I_1, I_2, I_3 of the inertia tensor (assuming uniform density) as

$$\frac{a}{b} = \sqrt{\frac{I_3 - I_1 + I_2}{I_3 + I_1 - I_2}}, \quad \frac{b}{c} = \sqrt{\frac{I_1 - I_2 + I_3}{I_1 + I_2 - I_3}}. \tag{3.20}$$

Since the values of ratios computed with our model were obtained from synthetic data based on DAMIT, they should be ideally the same as values derived from the inertia tensor, but our model is, of course, simplified and surely introduces a method bias. The result is shown in Fig. 3.30. For both ratios, we calculated the linear (Pearson) correlation and Spearman correlation, the coefficients ρ are summarized in Table 3.2. For the ratio a/b we obtained the correlation coefficients $\rho \sim 0.9$ which suggests that a/b is well-determined, while the ratio b/c is unconstrained.

Next, we applied our model on real data. The setup was the same as described in Section 3.4: weight $w = 5$; model noise $\sigma_{model} = 0.06$; and data noise $\sigma_L = 0.07$, respectively, σ_L was calculated according the equation (3.17) for asteroids less bright than 80. We compared resulting ratios a/b and b/c of 765 asteroids included in DAMIT with a/b_{DAMIT} and b/c_{DAMIT} and calculated correlation coefficients (see

44
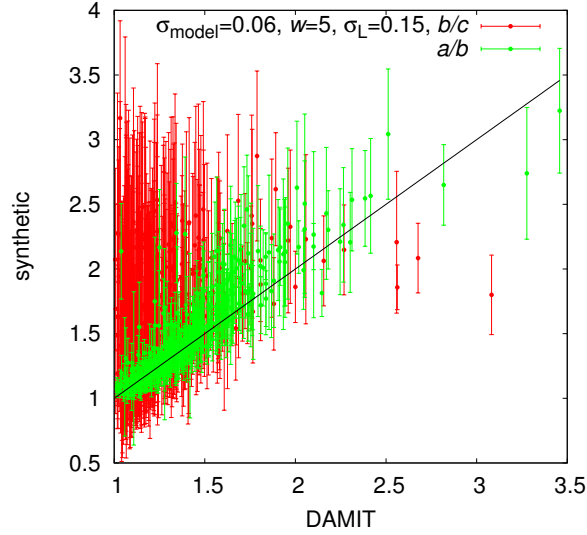
Figure 3.30: A comparison of the values of a/b and b/c derived from DAMIT shape models with values calculated from synthetic data described in Sec. 3.2. To create the synthetic data, one shape model from DAMIT was used more than once. The error bars thus denote the standard deviation of the mean value of the calculated values that all match with a single shape model from DAMIT.

	ρ_{linear}	ρ_{Spearman}
synthetic data, a/b	0.88	0.91
synthetic data, b/c	0.35	0.38
real data, a/b	0.48	0.61
real data, b/c	0.053	0.088

Table 3.2: The linear (Pearson) and Spearman coefficients ρ of correlation between ratios a/b and b/c derived from DAMIT shape models and ratios calculated with our model from synthetic data.
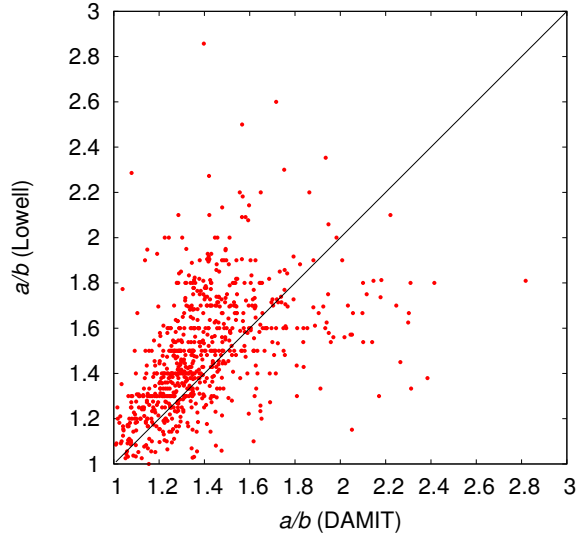
Figure 3.31: A comparison of 756 values of the a/b ratio calculated from the photometric data from the Lowell database with the corresponding values from the DAMIT database.

Table 3.2 and also Fig. 3.31). Since the ratio b/c is unconstrained (the correlation coefficient is lower than 0.1), in following tests we will study only the a/b ratio. The problem to determine the ratio b/c is linked to our previous result that the distribution of pole latitudes β shows a preference for high values of β, especially for small bodies (see Fig. 3.24), because for a spin axis with high β (small ϵ) we have observations only from a limited range of polar aspect angles. The determination of b/c, however, definitely requires observations from wide range of aspect angles. In principle, we could choose asteroids with sufficient coverage of observations and obtain reliable values of b/c, but considering the β distribution, such sample would be too small for a statistical use.

3.6.1 Distribution of a/b for groups of asteroids

Similar as for distribution of spin axes longitudes, we constructed distributions of a/b for some selected asteroid populations.

Asteroids with different sizes. First, we studied groups of asteroids with different diameters and we found that larger asteroids ($D > 25\,\text{km}$) are clearly more spheroidal (values of a/b are closer to 1) and smaller bodies are more elongated (the mean value of a/b is 1.6 ± 0.3), as is shown in Fig. 3.32. The differences between distributions in Fig. 3.32 on the right are much bigger than the uncertainties estimated from bootstrap testing.

We repeated this test for a smaller sample of 3819 asteroids, which were verified by bootstrapping in Sec. 3.3.3 as having well-determined a/b. The dependence of a/b on D remained, which means that the poorly constrained models did not cause any systematic change of a/b distribution.

McNeill et al. (2016) determined the average axial ratio for asteroids with diameters $D < 8\,\text{km}$ from Pan-STARRS1 survey as $1:0.85 \pm 0.13$, i.e., $a/b = 1.18$, which is not in agreement with our findings. For the corresponding range of
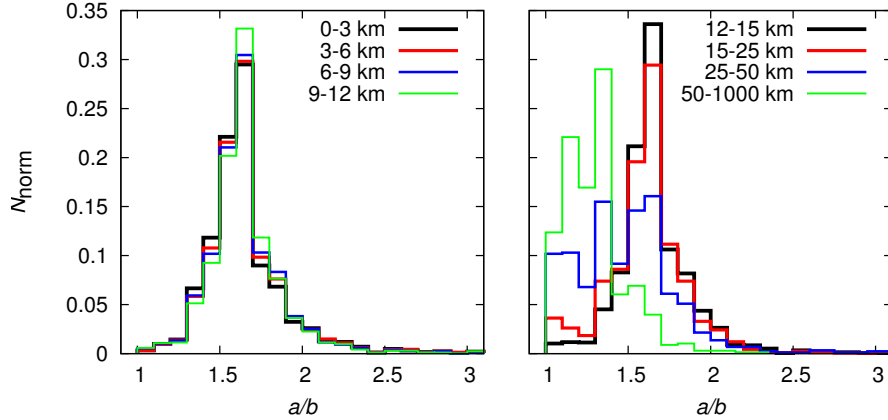
Figure 3.32: Distributions of a/b for groups of asteroids with different sizes (from 0 to 12 km on the left; from 12 to 1000 km on the right). The numbers of objects in individual groups are listed in Table 3.1.

diameters, we calculated the average value of a/b for asteroids in DAMIT (derived from the principal moments of the inertia tensor). The average value is $a/b_{\text{DAMIT}} = 1.47 \pm 0.25$, however, the sample of asteroids from DAMIT with $D < 8\,\text{km}$ is probably strongly biased, containing preferentially more elongated asteroids, for which it is easier to find a solution of the lightcurve inversion. In Chap. 4, we also analyze the Pan-STARRS data using a different method and compare the results with findings of McNeill et al. (2016).

We also checked our result that larger asteroids are more often spheroidal, against the asteroids in DAMIT. For $D > 50\,\text{km}$, we obtained the average value of $a/b_{\text{DAMIT}} = 1.23 \pm 0.13$ (our model gives $a/b = 1.29 \pm 0.17$). We can conclude that the dependence of a/b on diameter is real, but our model gives higher values of a/b for asteroids with $D < 25\,\text{km}$. Considering the dispersion of values σ_L in Fig. 3.5, this could be because we underestimated data noise for smaller and less bright asteroids.

Different parts of the main belt. Next, we constructed distributions of a/b for asteroids with different inclinations of orbits. Since the previously revealed dependence on the diameter can influence also this comparison, we used only asteroids with $D < 20\,\text{km}$. The differences between resulting a/b distributions are not so pronounced as when we studied the dependence on diameter, and they are comparable with the uncertainties of a/b.

We also studied distributions of a/b for asteroids with different semimajor axes, specifically inner, middle, pristine, and outer belt. The differences between distributions of a/b are not significant though, as they are again comparable with the uncertainties in a/b.

Dynamical families. Regarding the comparison for dynamical families and their backgrounds, we used only asteroids with $D < 20\,\text{km}$. We did not found any family to be significantly different from its background. Neither the comparison for families with each other show any differences larger than uncertainties of a/b.
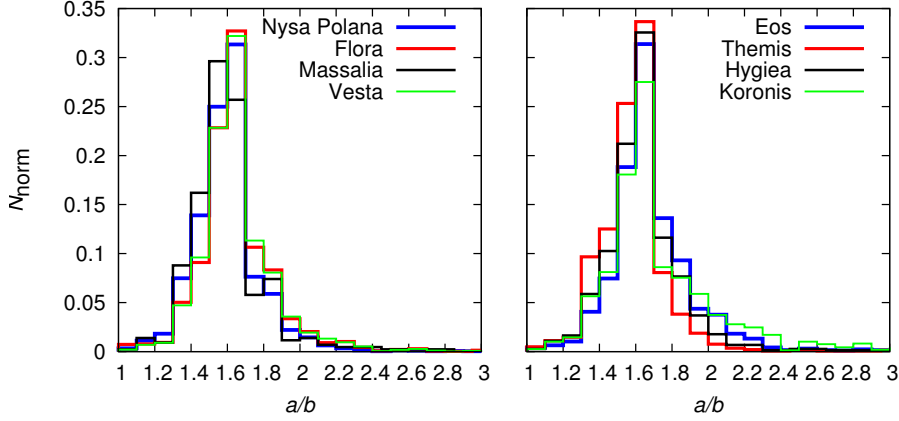
Figure 3.33: Distributions of a/b for some selected dynamical families.
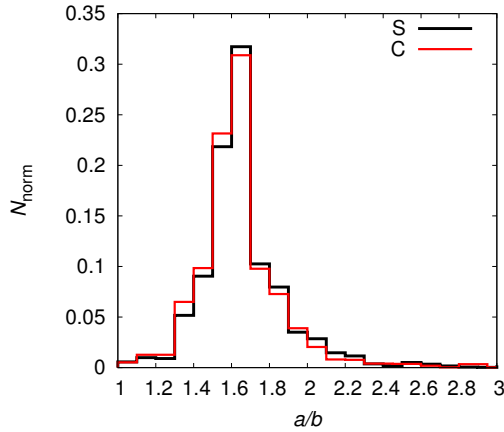
Figure 3.34: Distributions of a/b for two main taxonomic complexes S (black line) and C (red line).

Szabó and Kiss (2008) derived distributions of a/b for eight asteroids families using data from the Sloan Digital Sky Survey (SDSS). Their distributions are surprisingly different from ours; they are often bimodal (Figures 4, 5, 6 therein) and have a maximum for $a/b \sim 1.2$ (recall our distributions have maximum around 1.6). They also suggested a possible dependence on the age of families (old families should contain more spheroidal members), but we do not observe that behaviour in our distributions. We believe they used a questionable assumption that could influence the results: a fixed value of spin axis latitude for all asteroids (they tested $\beta = 50°$ and also a simplified case when the rotational axes of all asteroids are perpendicular to the line of sight).

Taxonomic classes. Finally, we compared distributions of a/b of the two largest taxonomic classes C and S. The result of the KS test, $Q_{KS} = 0.0018$, suggests that these two populations are not significantly different since as explained above (Sec. 3.4.2), we require $Q_{KS} < 10^{-4}$ to decide otherwise. The distributions shown in Fig. 3.34 confirm this interpretation.
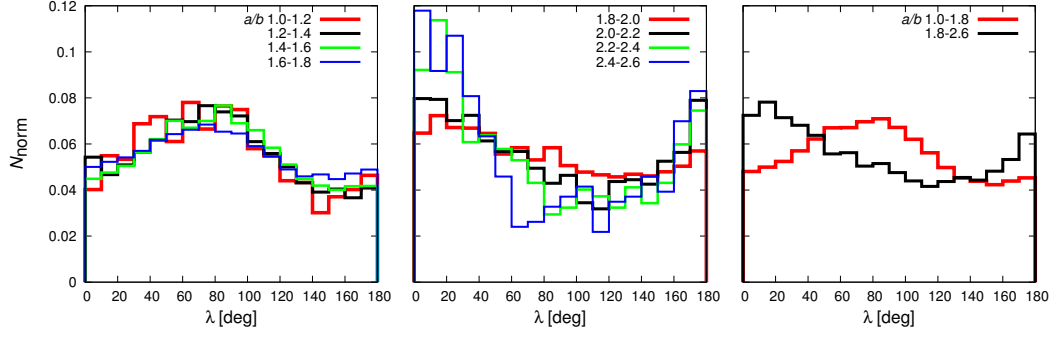
Figure 3.35: Left and middle: Distributions of λ for different elongations of asteroids. Right: The previous distributions summed into two groups.

a/b	$1.0 - 1.2$	$1.2 - 1.4$	$1.4 - 1.6$	$1.6 - 1.8$
N	1 294	4 476	22 782	27 515
a/b	$1.8 - 2.0$	$2.0 - 2.2$	$2.2 - 2.4$	$2.4 - 2.6$
N	7 744	2 609	1 020	458

Table 3.3: The number of asteroids N in asteroid populations with different shape elongation a/b.

3.6.2 Dependence of distribution of λ on a/b

After studying distributions of spin axis longitudes λ and shape elongations a/b separately, we then examined the dependence of λ on a/b. We divided asteroids into eight groups according to their elongation: from $a/b = 1.0$ to 2.6, with the width of each bin 0.2. For each group, we constructed a distribution of λ (see Fig. 3.35 on the left and in the middle). We found that with increasing elongation, the maximum of the distribution of λ is shifted towards lower values. Nevertheless, we have to be careful, because with increasing elongation, the number of asteroids decreases and the group with a/b from 2.4 to 2.6 contains 458 objects only (see Table 3.3). Therefore, we created only two subpopulations, first with a/b from 1.0 to 1.8 containing in total 56 067 asteroids, the second from 1.8 to 2.6 containing 11 831 asteroids, which is sufficiently numerous sample. We calculated the KS test and obtained almost zero probability ($Q_{\text{KS}} < 10^{-16}$) that these two λ distributions belong to the same parent distribution (see also Fig. 3.35 on the right). This is another interesting result, for which we were not able to find an explanation.

4. Analysis of the photometric data from the Pan-STARRS1 survey

In this Chapter, we focus on photometric data from Panoramic Survey Telescope & Rapid Response System (Pan-STARRS). These data cannot be analyzed with the model described in Chapter 3.1, because Pan-STARRS photometry does not provide enough measurements covering long enough time intervals. Therefore, we used a different model developed by Nortunen et al. (2017), which also enables us to construct distributions of shape elongations b/a and ecliptical latitudes β of the spin axis for selected asteroid populations. We should emphasize that this method is not meant to invert the shape and spin characteristics of individual lightcurves; the inversion works only on a population-scale, where we consider the shape and spin distributions of a large population. The distributions are then compared with the Latitudes and Elongations of Asteroid Distributions Estimated Rapidly (LEADER) algorithm (Nortunen and Kaasalainen, 2017).

4.1 Description of the model

Similar as in Sec. 3.1, we approximate the shape of an asteroid with a simple biaxial ellipsoid with $a \geq b = c = 1$ and we describe the shape elongation by the parameter $0 < b/a \leq 1$. Small b/a denotes an elongated body, and $b/a = 1$ denotes a sphere. This shape approximation is rough, but with a high number of observations ($\propto 10^3$), it will portray statistical tendencies of a population accurately. For completeness, we include all the values $0 < b/a \leq 1$ in our grid, despite the fact that the proportion of highly elongated values $b/a < 0.4$ is negligible, and most asteroids have $b/a > 0.5$. Thus, if the solved b/a distribution contains an unusually high number of bodies with $b/a < 0.4$, it is usually an indicator of some error in the solution, caused by noise and/or instabilities. Our second parameter is the spin co-latitude $\beta^\star$ of the spin axis. In our convention, $\beta^\star = 0$ indicates that the spin direction is perpendicular to the ecliptic plane, while $\beta^\star = \pi/2$ means the spin is in the ecliptic plane (this is opposite from the ecliptical latitude β used in previous section).

As our observable we utilize the brightness variation η defined in Eq. 3.7. For the lightcurve amplitude A we can write:

$$A = \sqrt{1 - \left(\frac{1}{\sqrt{8}\eta} + \frac{1}{2}\right)^{-1}}. \tag{4.1}$$

Note that the amplitude is based on intensity, not on magnitudes. With the amplitudes known, we can create their cumulative distribution function $C(A)$.

To solve the joint distribution for elongation b/a and spin co-latitude $\beta^\star$, we create a grid of bins $((b/a)_i, \beta_j^\star) \in [0,1] \times [0, \pi/2]$, where i = 1, ..., k and j = 1, ..., l. Our goal is to determine the proportion of each bin. The cumulative distribution function (CDF) can be written as a linear combination of other

functions:

$$C(A) = \sum_{i,j} w_{ij} F_{ij}(A), \qquad (4.2)$$

where $F_{ij}(A)$ are monotonously increasing basis functions derived by Nortunen et al. (2017):

$$F_{ij}(A) = \begin{cases} 0, & A \leq (b/a)_i \\ \frac{\pi}{2} - \arccos \frac{\sqrt{A^2 - (b/a)_i^2}}{\sin \beta_j^\star \sqrt{1 - (b/a)_i^2}}, & (b/a)_i < A < \mathcal{F}((b/a)_i, \beta_j^\star) \\ \frac{\pi}{2}, & A \geq \mathcal{F}((b/a)_i, \beta_j^\star), \end{cases} \qquad (4.3)$$

where $\mathcal{F}((b/a)_i, \beta_j^\star) = \sqrt{\sin^2 \beta_j^\star + (b/a)_i^2 \cos^2 \beta_j^\star}$. Each basis function $F_{ij}(A)$ describes the contribution made by objects in a given bin $((b/a)_i, \beta_j^\star)$ to the CDF $C(A)$. The weights w_{ij} are the occupation numbers of each bin $((b/a)_i, \beta_j^\star)$. Eq. (4.2) can be written in an equivalent form,

$$Mw = C, \qquad (4.4)$$

where each column of the matrix M contains a basis function $F_{ij}(A)$, the vector w contains the occupation numbers w_{ij} and the vector C contains the CDF $C(A)$. To solve the Eq. (4.4), we can use linear least squares methods in e.g. Matlab, along with regularization and a positivity constraint that $w_{ij} \geq 0$. With the weights w_{ij} solved, we have the proportion of each bin $((b/a)_i, \beta_j^\star)$.

Having the joint distribution for b/a and $\beta^\star$, we can compute the marginal distribution functions (DFs) for both parameters $f_{b/a}$ and $f_{\beta^\star}$:

$$f_{(b/a)_i} = \sum_{j=1}^{l} w_{ij}, \quad f_{\beta_j^\star} = \sum_{i=1}^{k} w_{ij}. \qquad (4.5)$$

For the marginal DFs, we can compute the CDFs labeled as $F_{b/a}$ and $F_{\beta^\star}$. Typically, are goal is to compare CDFs of two populations, S_1 and S_2 (the CDFs are denoted as $F_{b/a}(S_1)$, $F_{b/a}(S_2)$, $F_{\beta^\star}(S_1)$ and $F_{\beta^\star}(S_2)$). To measure the statistical difference between populations we use the measure

$$D_{b/a}(S_1, S_2) = \alpha_k \| F_{b/a}(S_1) - F_{b/a}(S_2) \|_k, \qquad (4.6)$$

$$D_{\beta^\star}(S_1, S_2) = \alpha_k \| F_{\beta^\star}(S_1) - F_{\beta^\star}(S_2) \|_k, \qquad (4.7)$$

where $k = 1; 2; \infty$ and α_k is a norm-based scaling factor: $\alpha_1 = 1/4$; $\alpha_2 = 1$ and $\alpha_\infty = 2$ (Nortunen et al., 2017). Each norm provides different kind of information about the statistical differences of the populations. As a general rule, two distributions can be considered significantly different if $D \gtrsim 0.2$. However, to obtain a better understanding of the statistical differences, a visual inspection of DFs and CDFs is also recommended. The detailed description of the LEADER software can be found in Nortunen and Kaasalainen (2017) and the software itself is available in DAMIT database.

4.2   Data description

The 1.8-meter Pan-STARRS1 survey telescope (Hodapp et al., 2004; Tonry et al., 2012), build atop of Haleakala, Maui, started its 3-year science mission in May 2010. Photometric data were obtained in six optical and near-infrared filters (g, r, i, z, y and w). Due to the distinct survey goals and patterns, most of the asteroids were observed in a wide-band w-filter ($\sim 400 - 700$ nm). We used the unpublished high-precision calibrated chip-stage photometry (Schlafly et al., 2012) with photometric errors and selected detections of a good photometric quality. Only PSF-like and untrailed detections were considered. Our subset spanned from April 11, 2011 until May 19, 2012. In total, we had photometric data for 348 210 asteroids with about 20 measurements for an asteroid on average. The second highest number of measurements is in the i-band, where we have data for 136 463 asteroids. Only the w-band data provided enough measurements for a reasonable application of our model. We shortly discuss results from the i-filter and compare them with results from the w-filter in Sect. 4.4.5.

The typical time interval between two measurements in the w-band filter is $\sim$17 minutes (see Fig. 4.1). However, not all the data were applicable to our model. Our conditions on the data were following:

1. The time interval between measurements greater than 0.01 day ($\sim$ 14 minutes). In the case of shorter interval the rotational period would not be randomly sampled over one rotation of $\sim$hours, and in the case of longer minimum interval we would lose a significant amount of data, as we can see from Fig. 4.1.

2. Then, we limited the solar phase angle α to be $\leq 20°$. In the model we assume this angle to be close to zero, however, in the data, there are not enough measurements with $\alpha \sim 0°$, therefore, we have to choose some reasonable value (see also Fig. 4.1). As described in Nortunen et al. (2017) (they used $\alpha \leq 30°$) the error caused by this condition is negligible.

3. Finally, we required at least five measurements satisfying previous conditions within 3 days to keep the geometry of observation sufficiently constant (this is the same condition as in Nortunen et al., 2017).

It is possible that for the same asteroid we had two (or even more) sets of measurements. In that case, each set was incorporated in the model.

4.3   Tests of the model

Before we compute the solution of the inverse problem from Eq. (4.4) for any Pan-STARRS1 population, we should test if the method is reliable with the given database. To do that, we first test our model using synthetic data. Then, with the real data, we test how large population of asteroids is necessary to provide stable results.
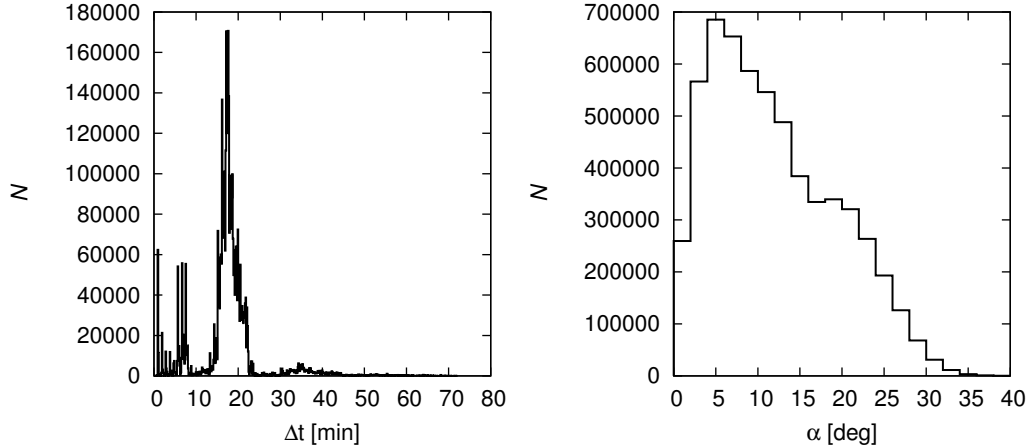
Figure 4.1: Left: The histogram of time intervals between measurements in the w-band filter from the Pan-STARRS1 survey. Right: The histogram of the solar phase angle α.

4.3.1 Synthetic data

The synthetic data were created according to the procedure described in Nortunen and Kaasalainen (2017). We chose a peak of the $(b/a, \beta^\star)$ distribution. For each asteroid in the considered population we chose a shape model from DAMIT, with $|b/a_{\mathrm{DAMIT}} - b/a_{\mathrm{wanted}}| \leq 0.075$. The rotation period was chosen randomly between 3 and 12 hours from a uniform distribution (we did not use rotation periods from DAMIT, as they could be biased). Next, we used the real Pan-STARRS1 geometries and times of observations and computed the synthetic brightness using a combination of Lommel–Seeliger and Lambert scattering laws. To simulate noise, we added a minor Gaussian perturbation $1 - 2\%$. Our aim was to find how well the solution distribution computed from Eq. (4.4) coincides with the known, synthetic distribution. For simplicity, we are interested in reconstructing the highest peak of the joint $(b/a, \beta^\star)$ distribution. The peak is defined as the bin with the highest occupation numbers. Similar synthetic simulations were used by Nortunen et al. (2017) to estimate the accuracy of the method for the WISE database. They found systematic errors in the computed solution and apply a posterior correction to the solution.

Number of bodies in a population. First, we create 50 synthetic populations, each containing N asteroids, where $N = 100$ to 5000 to test how the accuracy of our method increases with a growing number of bodies. For each population we randomly chose a single peak (actual $(b/a, \beta^\star)$) and plotted it together with the computed $(b/a, \beta^\star)$ peak to see how well they coincide. The results are shown in Fig. 4.2.

As we can see from the b/a plots (left columns), with growing number of asteroids in a population, the accuracy of the obtained b/a distribution is significantly improved. For $b/a \lesssim 0.4$, there is always some overshoot and undershoot, but as mentioned above, with the real data, we typically have $b/a \gtrsim 0.5$. Thus, the peak of the distribution can also be expected to be above 0.5. For $N < 1000$, there is a slight overshoot even when $b/a > 0.5$, suggesting the asteroids are slightly
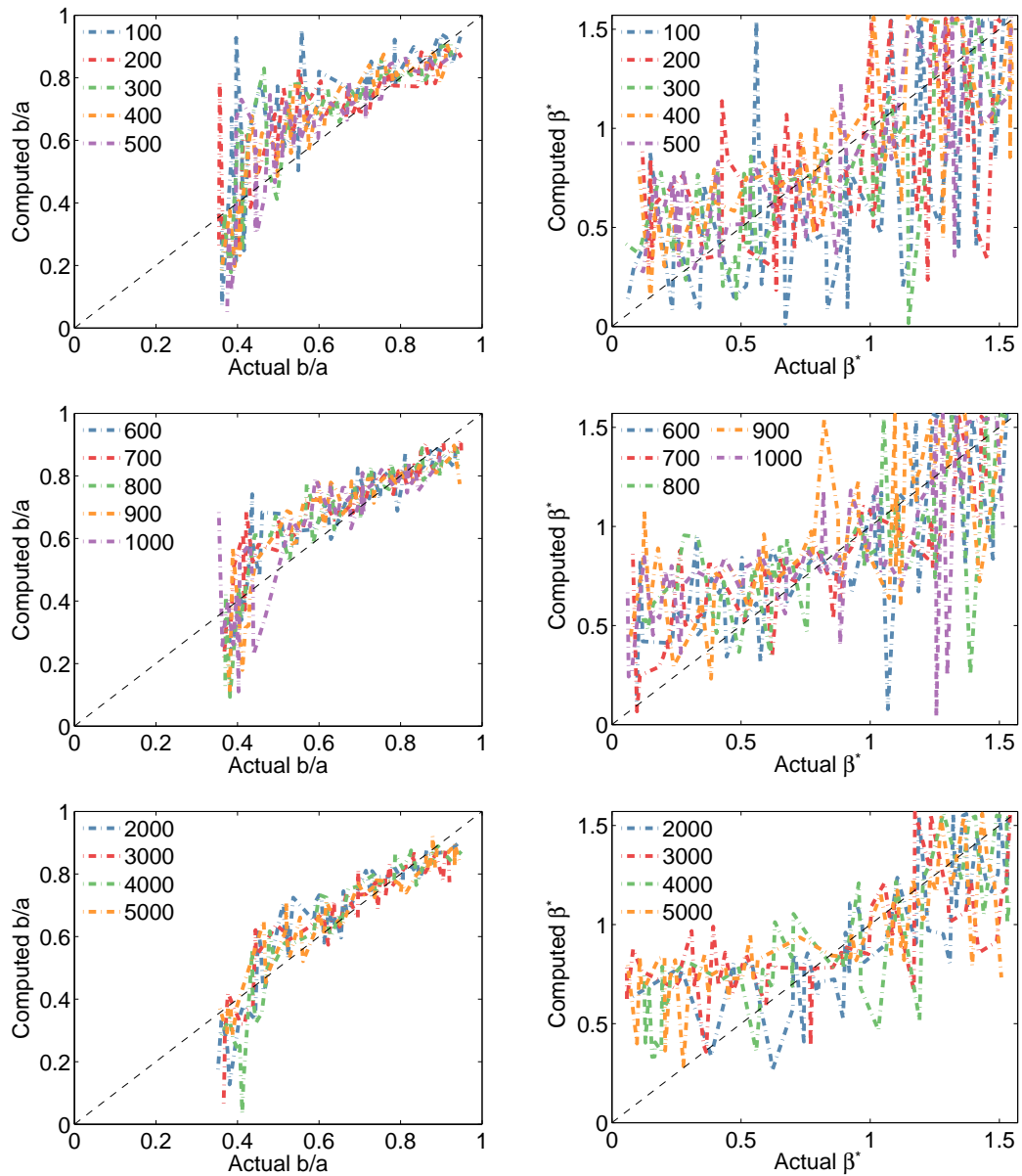
Figure 4.2: Synthetic simulations showing how the accuracy of our method improves with a growing number of asteroids (from 100 to 5000). The plots have the real peak of the distribution plotted versus the computed peak. The black dashed line of the form "$y = x$" denotes the ideal situation when the actual and computed peaks are the same.
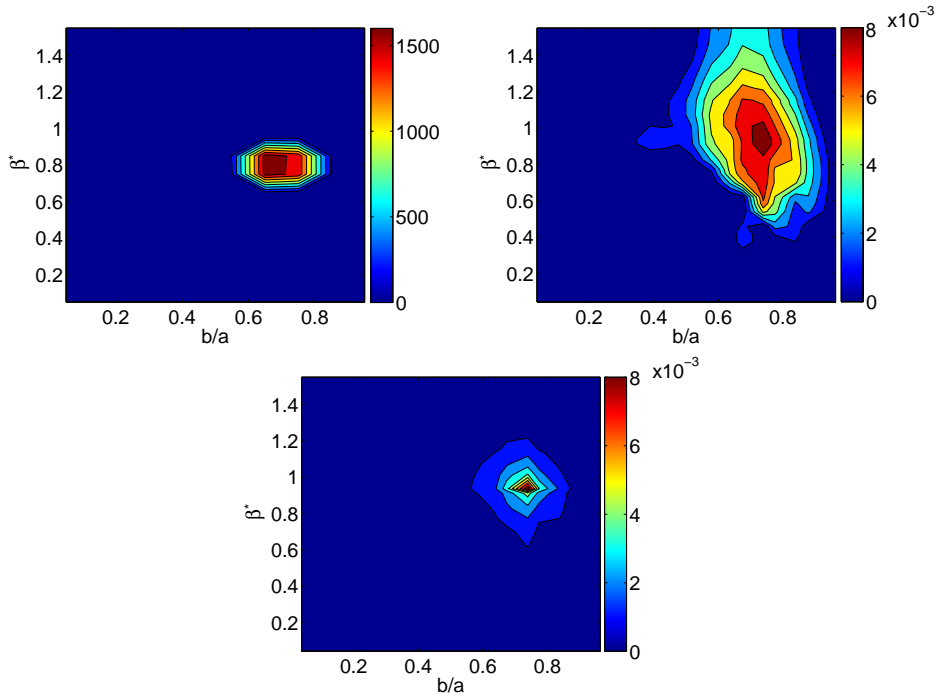
Figure 4.3: Synthetic simulations using a fixed $(b/a, \beta^\star)$ peak for a population of $10\,000$ asteroids. Top left plot shows the actual $(b/a, \beta^\star)$ distribution, top right shows the computed $(b/a, \beta^\star)$ distribution, and bottom shows the top right solution with a deconvolution filter applied.

more spheroidal than what they actually are. Nevertheless, with a population of more than 1000 objects, the computed b/a peak is very accurate for the realistic shape elongations $b/a > 0.5$.

The situation is substantially worse for the $\beta^\star$ distribution (see Fig. 4.2, right columns). For a population with a number of asteroids $N < 1000$, no actual information can be recovered since the solution is too noisy. The improvement of the accuracy is noticeable for populations with $2\,000 - 5\,000$ bodies. When the $\beta^\star$ peak is high (bodies in the ecliptic plane), the computed distribution also has a high $\beta^\star$ peak, but for a low $\beta^\star$ peak, our model shifts the computed $\beta^\star$ to the middle values. To conclude, due to the low accuracy of the computed $\beta^\star$, we have to be careful when interpreting results of $\beta^\star$ distributions of asteroid populations.

We are also interested in the overall shape of the joint distribution. The computed distribution is typically spread too much, especially in $\beta^\star$ direction, and has a tail towards the spin directions in the ecliptic plane. To correct this error, we may apply a deconvolution filter to the computed distribution, i.e., we reduce the occupation numbers of bins when moving further away from the peak. A similar method was used in Nortunen et al. (2017). In Fig. 4.3, we plotted an example of a typical solution and the effects of deconvolution, when we reduced the spreading of the solved distribution, but did not shift the position of the $(b/a, \beta^\star)$ peak. The shown results are from the simulation with a population of 10 000 asteroids with fixed $(b/a, \beta^\star)$ peak and with the geometries from Pan-STARRS1 database.

We emphasize that the reliability of this method is strongly dependent on the used asteroid database and it should never be used as a "black box" for a database.
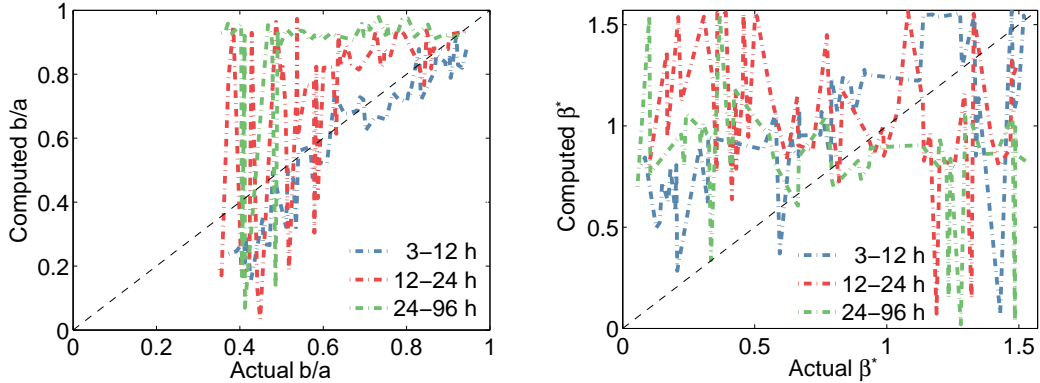
Figure 4.4: Synthetic simulations showing the accuracy of our method for different values of rotation period P. The black dashed line denotes the ideal situation.

For each database we should test the validity using synthetic simulations to estimate the error, since the noise level and noise distribution in the database is rarely known, For example, Nortunen and Kaasalainen (2017) performed similar synthetic simulations for WISE database and found that in comparison with the synthetic simulations with Pan-STARRS1 database, the results are considerably different.

The influence of the rotation period. Next, we studied how accurately we are able to reproduce the known $(b/a, \beta^\star)$ distribution when we create synthetic data by using different rotation periods P. We chose the following intervals of P: (i) $3 - 12$ hours; (ii) $12 - 24$ hours; and (iii) $24 - 96$ hours. The synthetic populations contained $2\,000$ asteroids each. The results are plotted in Fig. 4.4. Considering the b/a distribution, for $P < 12\,\mathrm{h}$ our method provides reliable results. For $P > 12\,\mathrm{h}$ the solution prefers values of $b/a \sim 1$ (spheroidal bodies) and moreover, the solution becomes unstable for $b/a < 0.6$. As to the $\beta^\star$ distribution, for $3 < P < 12\,\mathrm{h}$ we can notice a correlation between actual and computed $\beta^\star$, but for $P > 12\,\mathrm{h}$, the $\beta^\star$ distribution is unconstrained.

The fact, that our computed distributions of b/a for slow rotators ($P > 12\,\mathrm{h}$) peak at $b/a \sim 1$ is probably due to the time distribution of Pan-STARRS1 measurements. For most asteroids, data were obtained during a single night, i.e., few hours. If the real P is much longer, the data cover only a small fraction of the full lightcurve (showing the time evolution of brightness during the whole P). The changes of brightness are thus small and our model interprets them as belonging to a spheroidal asteroid. If we construct the distribution of P from the LCDB database for the asteroid included in Pan-STARRS1 database we found that most of the asteroids have $P \lesssim 15\,\mathrm{h}$. Nevertheless, we have to mention that the sample of objects in the LCDB database is biased and the number of slow rotators is underestimated since it is observationally difficult to determine long periods (Marciniak et al., 2015; Szabó et al., 2016).

The influence of the orbit inclination. Finally, using the synthetic data we tested the influence of the orbit inclination $\sin I$ on our solution since in the model we assume $\sin I = 0$. When creating the synthetic data, we used Pan-STARRS1
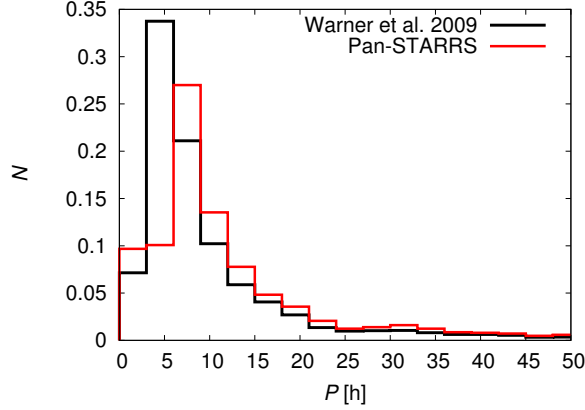
Figure 4.5: The distribution of rotation periods P for $14\,048$ asteroids stored in the LCDB database (Warner et al., 2009) (black line) and for $3\,731$ asteroids included in the Pas-STARRS1 database (red line).
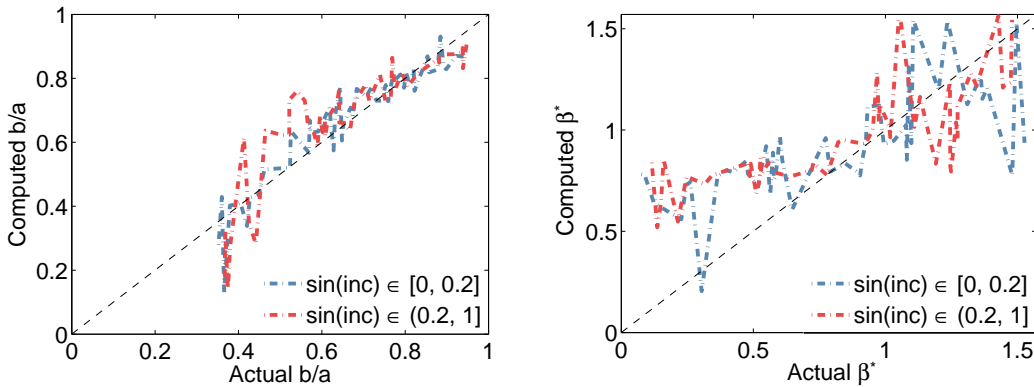
Figure 4.6: Synthetic simulations showing the accuracy of our method for different values of orbital inclination $\sin I$. The black dashed line denotes the ideal situation. There is no significant difference between populations with small and high inclinations.

geometries of $2\,000$ asteroids with $\sin I \leq 0.2$, i.e., first population, and $2\,000$ asteroids with $\sin I > 0.2$, i.e., second population. The resulting distributions of b/a and β are shown in Fig. 4.6. We can see that the differences between populations with small and high inclinations of orbits. For b/a, the computed peak corresponds with the actual peak, but for $\beta^\star$, we can notice the same problem as in Fig. 4.2, the model shifts the peak to middle values.

4.3.2 Test on the number of asteroids in a population with real data

Using the real photometric data from Pan-STARRS1, we tested how many asteroids have to be in a studied population to obtain reliable results, because typically we compare populations that contain different numbers of asteroids. We performed the following test: We used data for the Flora family and we randomly chose 100 of its members and ran our model ten times. We obtained ten distributions of b/a and of $\beta^\star$ from which we calculated one mean distribution

Figure 4.7: Distributions of b/a and $\beta^\star$ for Flora family constructed for growing number of asteroids that were included (from 100 to 2000).

for b/a and one for $\beta^\star$. We repeated this for a sample of 200 randomly chosen asteroids, then 300, 400 etc., up to the sample of 2000 asteroids. The selected mean distributions of these subpopulations of Flora family are shown in Fig. 4.7. For t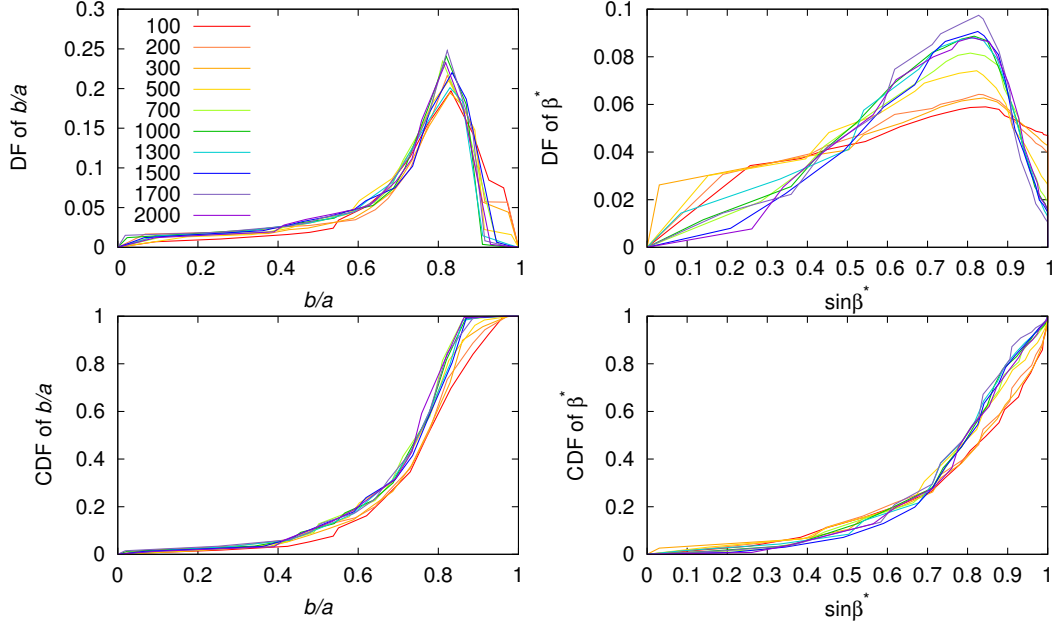he distribution of b/a we can see that the results are stable from ~ 700 asteroids in the subpopulation. However, for $\beta^\star$ the results are much more unstable, the distributions are clearly different even for populations with > 1000 asteroids. With growing number of bodies the peak of $\beta^\star$ distribution is higher and the number of asteroids with $\beta^\star \sim \pi/2$ decreases.

4.4 Distributions of shape elongations a/b

In this section, we will construct the distributions of shape elongation b/a for various subpopulations of main-belt asteroids. Similarly as in Sec. 3.6.1 we will focus on asteroids with different sizes, dynamical families, taxonomic classes and subpopulations of asteroids located in different parts of the main belt. To compare the distributions, we calculated $D_{b/a}$ and $D_{\beta^\star}$ according the Eq. (4.6) and (4.7). The bins in the distributions of b/a and $\beta^\star$ are chosen randomly, hence, for each two subpopulations that were compared, we processed ten runs and obtained 10 values of $D_{b/a}$ and $D_{\beta^\star}$, from which we calculated the mean values. For the distribution of b/a we chose 14 bins from 0 to 1, however, because the shape elongation greater than 0.25 is improbable, there was only one bin from 0 to 0.25, then one bin from 0.25 to 0.4 and 12 bins from 0.4 to 1. For the distribution of $\beta^\star$ we chose 20 bins from 0 to $\pi/2$, specifically, 15 bins for $\beta^\star > 43.4°$ and then always one bin in following intervals: $37.2° - 43.4°$, $31° - 37.2°$, $24.7° - 31°$, $18.5° - 24.7°$ and $0° - 18.5°$ to consider that the distribution of pole co-latitudes is uniform in $\sin\beta^\star$.

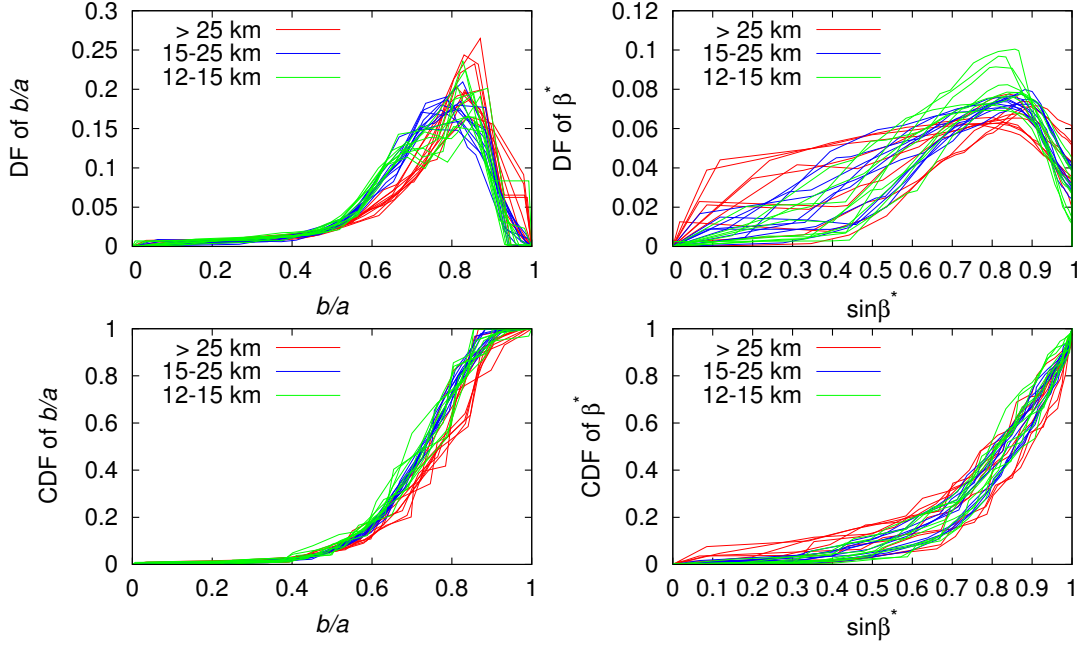**Figure 4.8:** DFs and CDFs of b/a and $\beta^\star$ for asteroids with $12 < D < 15$ km (red lines), $15 < D < 25$ (blue lines) and $D > 25$ km (green lines).

4.4.1 Asteroids with different diameters

First, we focused on groups of asteroids with different diameters D. We divided asteroids into seven groups: with $D < 3\,\mathrm{km}$; $3 - 6\,\mathrm{km}$; $6 - 9\,\mathrm{km}$; $9 - 12\,\mathrm{km}$; $12 - 15\,\mathrm{km}$; $15 - 25\,\mathrm{km}$; and $D > 25\,\mathrm{km}$; and compared them with each other. For $D < 15\,\mathrm{km}$ we have in all five groups more than 1200 asteroids, however, there are only 990 asteroids with $15 < D < 25\,\mathrm{km}$ and only 223 bodies in the last group ($D > 25\,\mathrm{km}$), which is not enough for a reliable result. The distributions for three groups with the largest D are shown in Fig. 4.8. Although, it is in agreement with the findings from Sec. 3.6.1 that the asteroids larger than $D > 25\,\mathrm{km}$ are more often spheroidal, in our case it might be just an effect of the low number of asteroids in the last subpopulation.

The mean values of $D_{b/a}$ for distributions of b/a for the three subpopulations with largest diameters are listed in Table 4.1. The distributions of b/a for groups of asteroids with $D < 15\,\mathrm{km}$ are not statistically different from the group of asteroids with $15 < D < 25\,\mathrm{km}$ and have a maximum for $b/a \sim 0.8$. The average axial ratio b/a from Pan-STARRS1 survey was also determined by McNeill et al. (2016). For asteroids with $D < 8\,\mathrm{km}$ they found the average b/a to be 0.85, which is a little more spheroidal than our result. Our results from Sec. 3.6.1 showed that the maximum of distribution of b/a for $D < 25\,\mathrm{km}$ is at ~ 0.63, i.e., asteroids are more elongated, nevertheless, as mentioned above, the previous results could be influenced by the underestimated data noise, which causes shape estimates to be more elongated. Finally, we can compare our results with the work of Nortunen et al. (2017) based on WISE data: the maxima of distributions of b/a for asteroids smaller than 25 km are ~ 0.5, for the large object ($D > 50\,\mathrm{km}$), the maximum is for $b/a \sim 0.7$, i.e., they determined larger asteroid elongations than what was found from Lowell photometry and Pan-STARRS1 data.

populations	$D_{b/a}(L^1)$	$D_{b/a}(L^2)$	$D_{b/a}(L^\infty)$
$D = 15 - 25$ km; > 25 km	0.164	0.269	0.351
$D = 12 - 15$ km; $15 - 25$ km	0.091	0.146	0.189
$P = 0 - 4$ h; $4 - 8$ h	0.369	0.537	0.573
$P = 0 - 4$ h; $8 - 15$ h	0.107	0.163	0.204
$P = 4 - 8$ h; $8 - 15$ h	0.450	0.638	0.642
Flora; background	0.087	0.159	0.244
Massalia; background	0.294	0.462	0.554
Nysa Polana; background	0.140	0.259	0.399
Vesta; background	0.068	0.114	0.170
Phocaea; background	0.175	0.274	0.367
Eunomia; background	0.079	0.123	0.176
Gefion; background	0.132	0.203	0.270
Maria; background	0.078	0.129	0.186
Koronis; background	0.142	0.244	0.367
Eos; background	0.084	0.142	0.208
Hygiea; background	0.098	0.163	0.218
Themis; background	0.134	0.243	0.342
Alauda; background	0.144	0.219	0.250
C class; S class	0.081	0.129	0.174
Massalia; backgro1und (filter i)	0.273	0.415	0.495
Phocaea; background (filter i)	0.212	0.291	0.333
filter w; filter i for Nysa Polana	0.095	0.160	0.220

Table 4.1: The parameter $D_{b/a}$ for selected pairs of populations that were compared. The given values are the mean values from ten runs of our model.
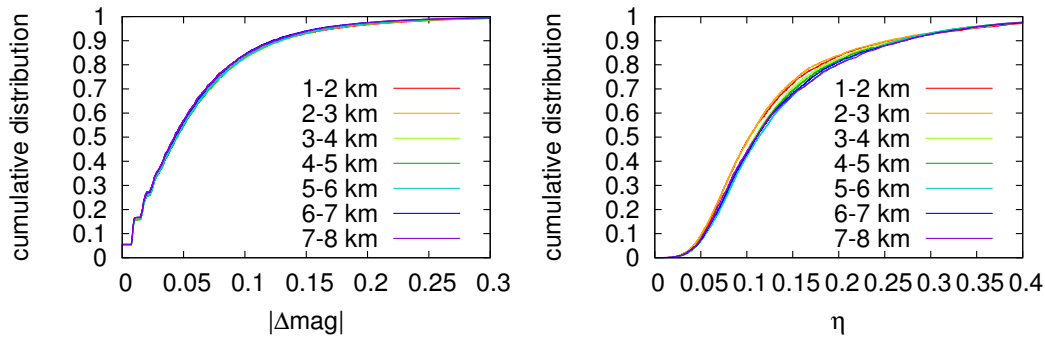
Figure 4.9: Left: Cumulative distributions of absolute value of change in magnitude $|\Delta\text{mag}|$ for groups of asteroids with different sizes. Right: Cumulative distributions of η for groups of asteroids with different sizes.

We also tried to reconstruct the cumulative distributions of absolute rate of change in magnitude from work McNeill et al. (2016), who constructed distributions for asteroids with $1 < D < 8\,\text{km}$ and divided them into groups $1-2\,\text{km}$, $2-3\,\text{km}$ etc. to $7-8\,\text{km}$. They found that with decreasing diameter, the distributions show smaller change in magnitude. However, we did not reveal any differences between individual distributions (see Fig. 4.9 on the left). The possible explanation of this disagreement is that McNeill et al. (2016) used only measurements with magnitude uncertainty ≤ 0.02, however, we used all measurements, our only conditions were (i) the solar phase angle $\alpha < 10°$ (this is the same condition as in McNeill et al., 2016) and (ii) pairs of measurements separated by time interval $10\text{ min} < \Delta t < 20\text{ min}$. We constructed also cumulative distributions of brightness variation η to see if there will be any differences, but as shown in Fig. 4.9 on the right, the η distributions for groups of asteroids with different diameters are almost the same.

Then we focused on the distributions of $\beta^\star$. As we can see in Fig. 4.8 on the right, they look different from our previous results or e.g., from Hanuš et al. (2011), where $\beta^\star$ is clustered around 0 due to the YORP effect, that shifts $\beta^\star$ near the pole of the ecliptic. Nevertheless, as explained in Sec. 4.3.1 or 4.3.2, we found that the distribution of $\beta^\star$ is considerably influenced by the number of asteroids in given subpopulation and becomes flatter with decreasing number of asteroids. In Fig. 4.2 we can also see that the model tends to shift the peak to the middle values. The results on $\beta^\star$ are thus not reliable and in the following tests, we will only focus on the distributions of b/a.

Because the number of asteroids with $D > 25$ km in data from Pan-STARRS1 is insignificant in comparison to the number of smaller asteroids (less than 1%), this dependence on diameter does not influence the results of the following tests.

4.4.2 Different rotation periods

According to their rotation periods P provided by the LCDB database, we divided asteroids into three groups. We chose different intervals than in Sec. 3.4.2 to ensure that all groups are populous enough for stable results. The individual groups are the following: (i) $P = 0-4\,\text{h}$ (1081 bodies); (ii) $4-8\,\text{h}$ (1967 bodies);
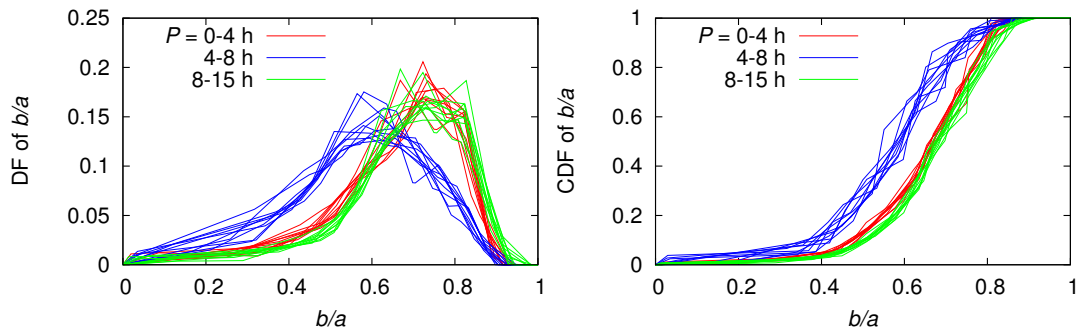
Figure 4.10: DFs and CDFs of b/a for asteroid populations with different rotation periods.
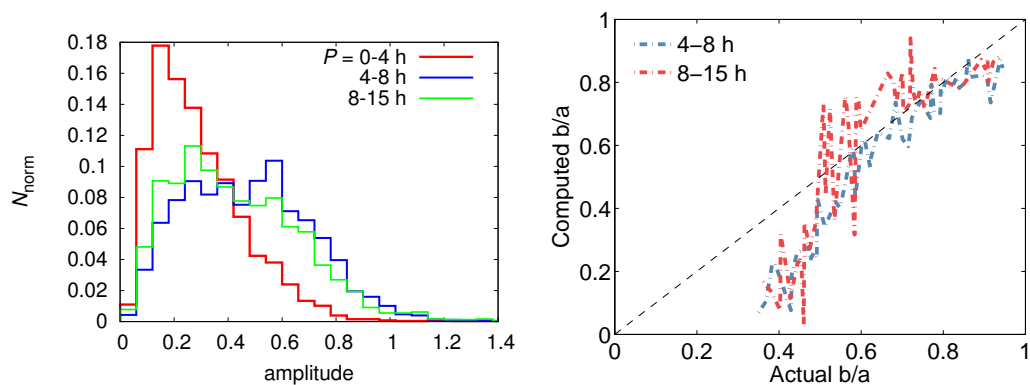

Figure 4.11: Left: Distributions of lightcurves amplitudes from the LCDB database for different rotation periods P. Right: Synthetic simulations showing the accuracy of our method for two different intervals of rotation period P.

and (iii) $8 - 15\,\mathrm{h}$ (1071 bodies). We excluded asteroids with $P > 15\,\mathrm{h}$ since our simulations with synthetic data showed the results are not reliable (see also Fig. 4.4).

We compared populations with each other and plotted their distributions of b/a in Fig. 4.10. We can see that the fastest rotators ($P = 0 - 4\,\mathrm{h}$) are on average more spheroidal (peak at $b/a \sim 0.75$) than the population with $P = 4 - 8\,\mathrm{h}$ (peak at $b/a \sim 0.6$), but their b/a distribution is not different from the third population with $P = 8 - 15\,\mathrm{h}$. The mean values of $D_{b/a}$ are listed in Table 4.1.

The critical rotation rate is, for the same density, dependent on the elongation (Pravec and Harris, 2000). The spheroidal bodies are thus able to rotate faster that the elongated ones, which is in accordance with our results for the first two populations. However, we were not able to explain why the third population, with $P = 8 - 15\,\mathrm{h}$, should contain more spheroidal asteroids than the population with $P = 4 - 8\,\mathrm{h}$. Therefore, using the LCDB database we constructed distributions of lightcurves amplitudes for the three above mentioned populations (see Fig. 4.11). Higher amplitudes correspond with larger elongations. The distributions of the first two groups are in accordance with the results from Pan-STARRS1 data, but for the third population ($P = 8 - 15\,\mathrm{h}$), we obtained similar distribution as for the population with $P = 4 - 8\,\mathrm{h}$.

To explain this discrepancy we performed another test with synthetic data. We used the same setup as in Sec. 4.3.1, where we studied the influence of the rotation period on the accuracy of the solution, but we chose populations with $P = 4 - 8\,\mathrm{h}$ and $P = 8 - 15\,\mathrm{h}$. The resulting distributions of b/a are shown in Fig. 4.11, right panel. We can see that for both populations, our model is not able to correctly reproduce peak $b/a \lesssim 0.6$, nevertheless such elongation peak is uncommon, most of the asteroids have $b/a > 0.6$. Considering $0.8 > b/a > 0.6$, for the population with $P = 8 - 15\,\mathrm{h}$, our model provides slightly more spheroidal objects ($b/a \sim b/a_{\mathrm{actual}} + 0.1$) and for the population with $P = 4 - 8\,\mathrm{h}$, it provides slightly more elongated objects ($b/a \sim b/a_{\mathrm{actual}} - 0.05$). We can conclude that the difference between b/a distributions for these two populations (shown in Fig. 4.10) is due to the method bias that shifts their b/a values ~ 0.15 apart.

By this analysis we have learned that our distributions of b/a for other asteroid populations can be strongly influenced by the appropriate period distributions. Unfortunately, our model does not provide the rotation period P and the LCDB database contains P for only $\sim 14\,000$ asteroids. That sample, divided into individual populations, is not large enough for a statistical purpose. Nevertheless, we noticed that P could be formally calculated directly from photometric data if there are many measurements for an asteroid and if they are appropriately distributed in time. More precisely, we need pairs of measurements close in time and also a sufficient number of such pairs.

As described in Nortunen et al. (2017), for the brightness L of an biaxial ellipsoid we can write (assuming $b = c = 1$)

$$L^2 = 1 + ((b/a)^2 - 1)\sin^2\theta\cos^2\phi \tag{4.8}$$

where θ denotes the aspect angle and ϕ the rotational angle. The mean quadratic brightness over one rotational period is then

$$\langle L^2 \rangle = \frac{1}{2\pi}\int_0^{2\pi} L^2 \mathrm{d}\phi = 1 + \frac{1}{2}\sin^2\theta\left(\frac{b^2}{a^2} - 1\right), \tag{4.9}$$

and the mean value of time derivative of L^2 is

$$\left\langle \left|\frac{\mathrm{d}L^2}{\mathrm{d}t}\right|\right\rangle = \frac{4}{P}\left(1 - \frac{b^2}{a^2}\right)\sin^2\theta. \tag{4.10}$$

For the variation of brightness defined by Eq. (3.7) we can write

$$\eta = \frac{1}{\sqrt{8}}\left(\frac{1}{\sin^2\theta(1 - b^2/a^2)} - \frac{1}{2}\right)^{-1} \tag{4.11}$$

Combining Eqs. (4.9), (4.10) and (4.11) we can derive the relation for the rotational period

$$P = 8\sqrt{2}\,\eta\frac{\langle L^2 \rangle}{\langle |\frac{\mathrm{d}L^2}{\mathrm{d}t}|\rangle}. \tag{4.12}$$

Notice, that to calculate the period we need only mean brightness, time derivative of brightness and variation of brightness η, but for each asteroid it requires a lot of measurements. The derivative $\frac{\mathrm{d}L^2}{\mathrm{d}t}$ can be approximately calculated from pairs of measurements close in time, but there is a lower limit due to the accuracy of

data. We chose $dt > 10$ min to distinguish the change of brightness from data noise.

To verify, if this relation can be used in practice, we performed a test on synthetic data created as follows: using the DAMIT models, the Hapke scattering model with randomly chosen parameters (as in Sec. 3.2) and randomly chosen rotational period P (uniformly distributed from 2 to 50 h), we calculated synthetic brightness that we assigned to ~1000 asteroids observed with Pan-STARRS1 (we left the geometry of observations unchanged), for which we had the largest number of measurements. From this new synthetic brightnesses we can calculate the period P according the Eq. (4.12) that should be the same as the synthetic P.

The derivative $\langle |dL^2/dt| \rangle$ was calculated from pairs of measurement separated by time interval $10 < \Delta t < 20$ min and we required at least 12 pairs (to calculate the mean value) within 5 days. The variation η as well as the mean brightness $\langle L^2 \rangle$ were also calculated within 5 days. We tested synthetic data without any noise and also data with Gaussian noise of 2%. We compared the calculated P with the synthetic by computing the correlation coefficient: data with noise show no correlation (the coefficient is 0.19) and as we can see in Fig. 4.12 (blue points), there is a strong preference for low values of P. Interestingly enough, the bias is systematic and amounts to an underestimation factor of about 0.5 for the point fan. Apparently noise systematically increases the slope average from the pairwise slope estimates. The situation for data without noise is slightly better (coefficient 0.30) and if we consider only periods from interval 2 to 30 hours, the correlation coefficient is 0.65 (see also Fig. 4.12). For periods under ten hours, the points are even more tightly clustered near the $x = y$ correlation line.

The possible reason for this bad correlation could be the insufficient number of measurements from which the mean values are calculated. Therefore, to each measurement we added two another, one 0.01 d (14.4 minutes) earlier and the second 0.01 d later. In total, we had three times more measurements for each asteroid. However, the resulting P were not significantly different from the previous test, in the interval of P from 2 to 30 hours, the correlation coefficient is 0.60.

We also tested the relation (4.12) on real data from Pan-STARRS1 survey, however, there were only few asteroids for which we had required number of measurements (as described above) and at the same time also the information about the real rotational period (from LCDB). For these bodies we did not obtain a good agreement between the estimated and the real periods. Apparently the use of the period estimate Eq. (4.12) requires a large number of well-distributed pairs of measurements over a rotation cycle and a low number of pairs exacerbates the effects of noise. Estimates based on the derivative of a function are usually considerably more unstable than those based on the function itself. This approach is thus not applicable in practice and we are not able to correct b/a distributions of other asteroid populations to have the same P distributions.

4.4.3 Dynamical families

Next, we compare distributions of dynamical families with their background formed by asteroids from the same part of the main belt as the family (inner, middle, pristine, outer), which do not belong to any other family. We focused
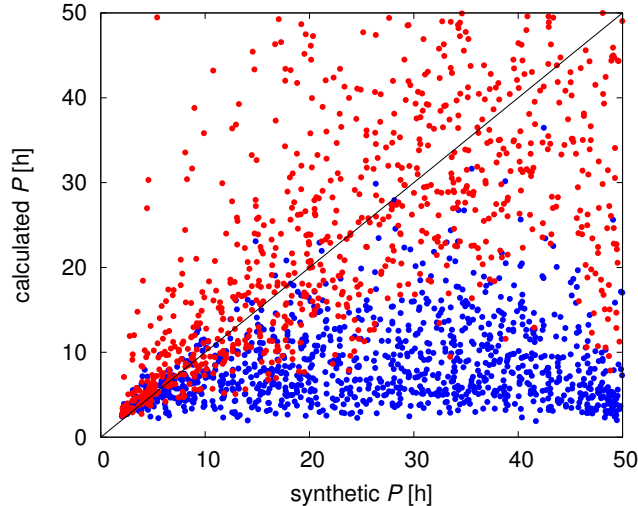
Figure 4.12: The comparison of calculated and synthetic rotational period P. The red points denote synthetic data without noise, the blue points synthetic data with noise 0.02.

on 13 most populous families: Vesta, Massalia, Flora, Nysa Polana and Phocaea in the inner belt; Eunomia, Gefion and Maria in the middle belt; Koronis in the pristine belt; Themis, Eos, Hygiea and Alauda in the outer belt; see also Fig. 3.19. The typical number of asteroids (for which we have enough data) in a family is few thousands, for Vesta, Flora and Nysa Polana it is slightly more than ten thousands and for Phocaea and Alauda it is less than 1000 (the exact numbers are in Table 4.2). Unlike in Sec. 3.6.1, where we did not reveal any differences among families, we found that Massalia has a significantly different distribution of b/a from its background, containing more elongated asteroids. Distributions are shown in Fig. 4.13 on the left. Significantly different are also cumulative distributions of brightness variation η of Massalia and its background, which are shown in Fig. 4.14 on the left. Unfortunately, we cannot compare our distribution of b/a for Massalia with the distribution from Nortunen et al. (2017) based on WISE data, because their sample contained insufficient number of bodies. The mean values of $D_{b/a}$ for all families are listed in Table 4.1. The second largest difference between distribution of b/a is for the Phocaea family and its background (see Fig. 4.13 on the right), nevertheless the value $D_{b/a}(L^1) = 0.175$ is not high enough for a definite answer. We should note than for Phocaea we have only data for 812 asteroids, however, the small number of asteroids causes the population to be more spheroidal and, as we can see in Fig. 4.13 on the right, Phocaea, in comparison to its background, contains more elongated objects.

We have to remind that the difference between Massalia family and its background can be due to the different period distributions. To test this possibility we used the LCDB database and constructed distributions of P for Massalia and its background (see Fig. 4.15). Before interpreting the results we have to emphasize that the shown distribution of Massalia contains only 100 bodies and 420 bodies represent its background, which is not enough for a solid conclusion. Nevertheless, we can see that Massalia really contains less objects with $P = 0 - 4\,\text{h}$ and more with $P = 4 - 8\,\text{h}$ than its background, which is in accordance with the
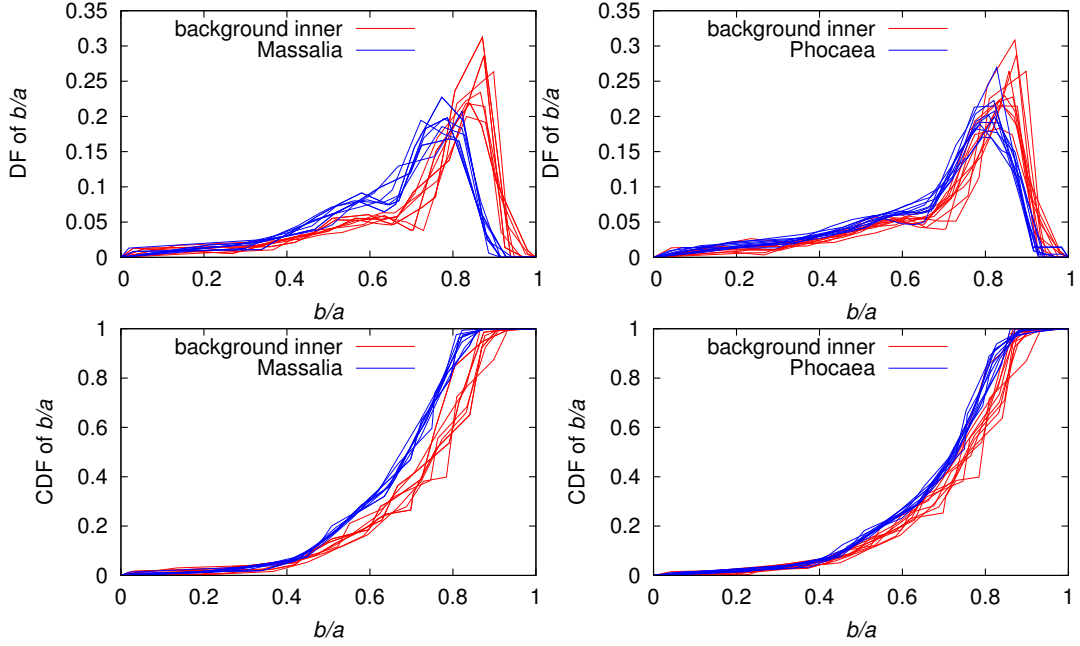
Figure 4.13: Left: DFs and CDFs of b/a for Massalia family (blue lines) and its background (red lines). Right: The same for Phocaea family.

family members being more elongated (compare with Fig. 4.10). We do not have enough periods determined for members of Phocaea to perform such test as for Massalia.

4.4.4 Taxonomic classes and different parts of the main belt

We also compared the distributions of b/a of the two most populous taxonomic classes: S that dominates in the inner mail belt, and C that dominates in the middle and outer belt. For both classes we had data for $\sim 10\,000$ asteroids from the SDSS-based Asteroid Taxonomy. We did not find these two groups to have different distributions of the shape elongation b/a.
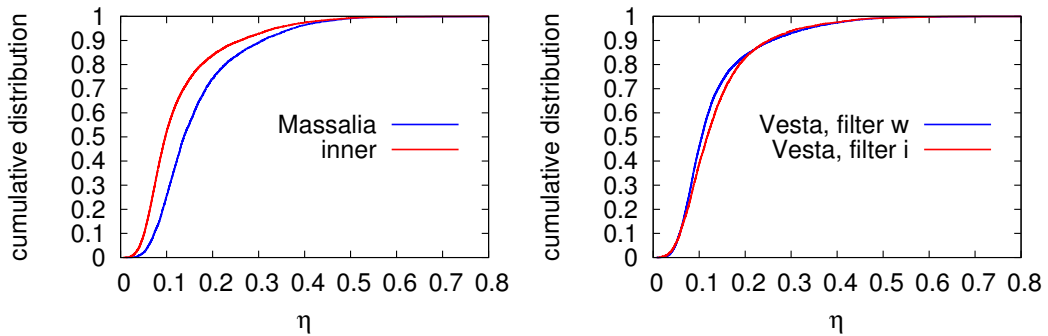
Figure 4.14: Left: Cumulative distributions of brightness variation η for Massalia family and its background. Right: Cumulative distributions of η for Vesta family in filter w and filter i.

67
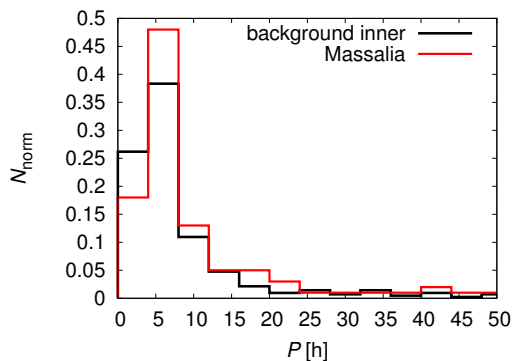
Figure 4.15: Distributions of rotation period P for Massalia family and its background. The values of P were taken from LCDB database. There are 100 bodies in Massalia and 420 bodies in its background.

family	N_w	background$_w$	N_i	background$_i$
Flora	11 291	11 029	4135	5316
Massalia	4267	11 029	1032	5316
Nysa Polana	14 741	11 029	4675	5316
Vesta	11 895	11 029	4863	5316
Phocaea	812	11 029	577	5316
Eunomia	4126	12 069	2247	6728
Gefion	2629	12 069	1203	6728
Maria	2203	12 069	1243	6728
Koronis	4845	1272	1881	775
Eos	8237	6665	4272	4172
Hygiea	4191	6665	1584	4172
Themis	4181	6665	1588	4172
Alauda	649	6665	489	4172

Table 4.2: The number of asteroids in individual families and corresponding backgrounds for which we have data from Pan-STARRS1 survey in filters w and i.

Figure 4.16: The same as in Fig. 4.13, but in the i-filter.

Finally, we compared groups of asteroids with different semimajor axes (inner, middle, pristine, outer) and with different inclinations of orbit. None of the subpopulations is significantly different from others.

4.4.5 Comparison of results from filters w and i

We also analyzed Pan-STARRS1 data in the i-filter ($\sim 700\text{-}800$ nm) (Tonry et al., 2012) and compared the results with the w-filter. We had data for 136 463 asteroids and on average, there were $\s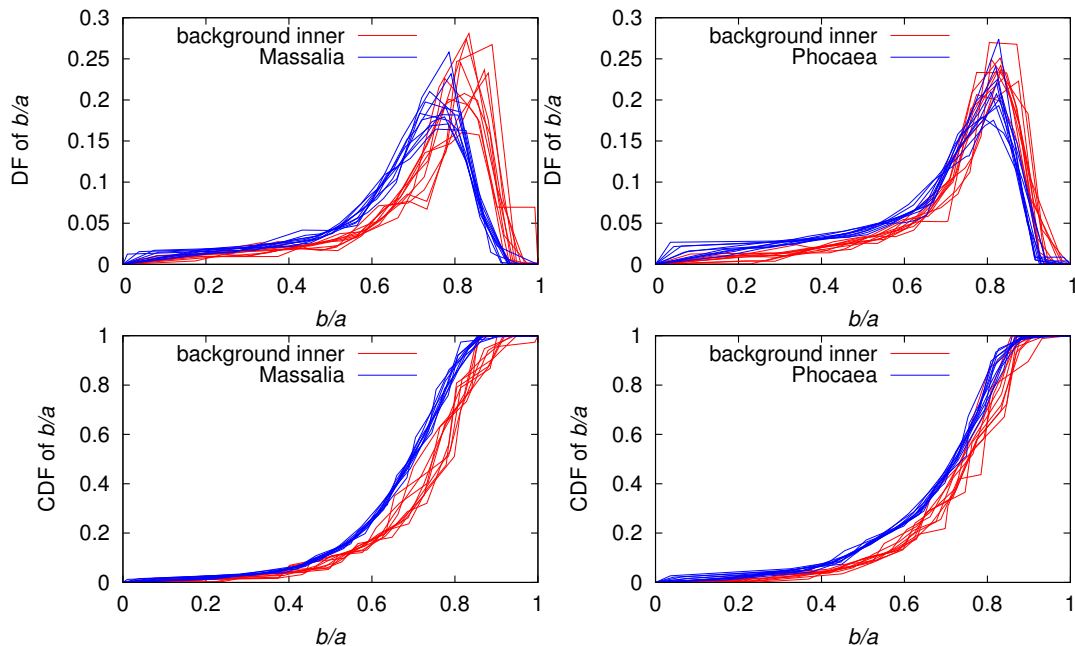im 10$ measurements for one asteroid. We focused only on taxonomic classes and dynamical families. There were not enough asteroids to study the dependence of the elongation of asteroids on the diameter (only few asteroids were in the two subpopulations with the largest D).

The number of asteroids in subpopulations containing the taxonomic class S was 6349 and for the taxonomic class C 5813. As in the w-filter, the difference between these two groups is insignificant. Then we focused on dynamical families. As in the w-filter, we found that Massalia family has a significantly different distribution of b/a from its background. Moreover, also the result for Phocaea ($D_{b/a}(L^1) = 0.212$) suggests that this family could have a different distribution of b/a from its background. However, Fig. 4.16 does not show a significant difference.

To compare results from the filters w and i directly, we constructed distributions of b/a for some families in both filters and calculated $D_{b/a}$. We did not find any significant differences between filters. As an example, distributions of Nysa Polana are shown in Fig. 4.17. We also constructed cumulative distributions of the brightness variation η for some families in both filters to confirm that there are no differences between filters before the inversion.
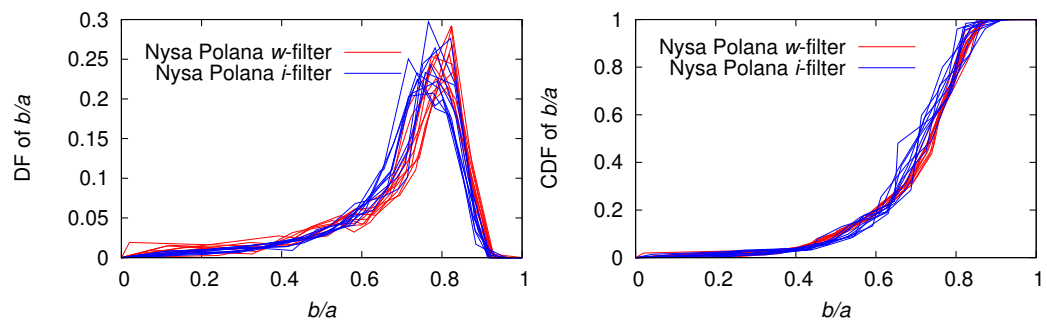
Figure 4.17: DFs (left) and CDFs (right) of b/a for Nysa Polana family in the i-filter (blue lines) and the w-filter (red lines).

Conclusions

The aim of this thesis was to study physical parameters of asteroids, specifically the distributions of position of the spin axes and of shape elongations. We analyzed two different datasets using two different methods, each suitable for the specific time distribution of photometric measurements.

Lowell Observatory database. Assuming a triaxial shape model, we developed a new method for determination of the direction of spin axis and elongation of asteroids, which can be used for sparse photometric data covering several apparitions. By testing on synthetic data, we found that our resulting distributions of ecliptical latitudes β have to be divided by the bias function. Our model has also few limitations: (i) it provides λ only in the interval $(0°, 180°)$, (ii) instead pole latitude, it provides only its absolute value and (iii) the determined shape elongation of asteroids could be a little larger than the real one (the determination is sensitive on data noise, which in our case can be underestimated). Using the bootstrap method we estimated the uncertainties in λ as $\simeq 30°$, in β as $16°$ and in a/b as 0.18. These uncertainties are large for individual bodies, but for statistical approach, such accuracy is sufficient. We then applied our method to $69\,053$ main belt asteroids for which a suitably rich and good quality set of observations were obtained from the Lowell Observatory database. The main results are as follows:

1. The distribution of λ is nonuniform, with an excess of asteroids with λ values between $60°$ and $100°$. Similarly, there is a deficiency of asteroids with λ values between $130°$ and $160°$. By testing on DAMIT models, we show that this nonuniformity is for both prograde and retrograde rotators and that there is not difference for $0° < \lambda < 180°$ and $180° < \lambda < 360°$.

2. Curiously, our tests revealed a correlation of the nonuniformity in λ with orbital inclination: asteroids with very low-inclination orbits ($\sin I \leq 0.04$) show the effect more significantly than asteroids with higher inclination orbits.

3. We constructed distributions of the absolute value β for asteroids with different sizes and we confirmed previously reported results that asteroids with size $D \leq 25$ km have their pole latitude tightly clustered about the poles of ecliptic. This is due to the YORP effect that makes the pole latitude to approach the extreme values asymptotically.

4. When studying the λ distribution for different intervals of rotation period P, we revealed that while for $P \lesssim 10\,\mathrm{h}$ the distribution follows the pattern of the whole asteroid population, for $P \gtrsim 10\,\mathrm{h}$ the distribution is significantly flatter.

5. We also analyzed our results for populations in different asteroid families. As to the λ distribution, they mainly derive from their inclination value of the aforementioned inclination dependence. For instance, the low-inclination families such as Massalia or Themis have the strongest nonuniformity of the λ distribution in our results. Among distributions of a/b

71

of families, we did not find any significantly different family from others. When studying distributions of β, we found that Gefion in the middle belt contains significantly more asteroids with $\beta > 70°$ than population of bodies in corresponding interval of inclinations and than population of bodies in the middle belt.

6. We also found that small main belt asteroids ($D \leq 25$ km) are more elongated, with a median of ratio $a/b \simeq 1.6$, compared to the large asteroids ($D \geq 50$ km), which have a median of ratio $a/b \simeq 1.3$.

7. Finally, we found that the distribution of λ is dependent on the elongation a/b: with increasing elongation, the maximum of λ distribution shifts to lower values.

We confirmed the previous unexpected result of Bowell et al. (2014), who found the nonuniformity in distribution of ecliptic longitude of spin axes of the main belt asteroids. We tested various hypotheses of its origin, but we had to reject most of them, proving that the proposed processes would not lead to a significant enough nonuniformity. A part of the solution of this problem could be a geometric projection of the precessing axis, but it seems it cannot explain the whole nonuniformity, unless there are some additional correlations between the relevant quantities. Therefore, this result remains enigmatic and requires further analysis. In particular, it would be very useful if more detailed methods of spin state and shape inversion from astronomical data confirmed this result and provided more details. Justifications of reliability of our method, by running blind tests against synthetic populations of asteroids and limited datasets for which complete models are already available, make our method a solid tool for further studies. Our results are available online and can be used in independent investigations of, e.g., asteroid families to constrain theoretical evolution models. It would be also interesting to apply our model to more accurate photometric data provided by Large Synoptic Survey Telescope (LSST).

Pan-STARRS1 survey. The previous method cannot be used when we have only few points during a single apparition. For such data, Nortunen et al. (2017) and Nortunen and Kaasalainen (2017) developed model that instead of individual asteroids works with large asteroid populations and instead of the inversion of lightcurves realizes inversion of distribution functions. Limitations of this model are: (i) it does not provide the pole longitude and (ii) it provides only the combined distribution of the $\beta^{\star}$ of both ecliptic hemispheres. Moreover, by testing on synthetic data we found that our model shifts the peak of the $\beta^{\star}$ distribution to the middle values and is strongly influenced by the number of objects in studied populations. For the distribution of b/a we found that the model provides stable results for numbers of objects higher than ~ 700. The test with synthetic data also revealed that our model provides reliable results only for asteroids with rotation periods $P \lesssim 12$ h. This is due to the time distribution of measurements of Pan-STARRS1 survey and thus it is not a limitation of the method in general. We analyzed mainly data in the wide w-band filter. The most populous asteroid populations were studied also in the i-filter. The main results are as follows:

1. Groups of asteroids with diameter $D < 25\,\mathrm{km}$ do not have significantly different distributions of b/a, the maximum of these distribution is for $b/a \simeq 0.8$. The distribution for asteroids larger than 25 km suggests that these objects are more spheroidal in comparison with the smaller ones, nevertheless, the number of objects in this population is insufficient for a strong result.

2. By comparing distributions of b/a for different intervals of rotation period P we found, that the fastest rotators with $P = 0 - 4\,\mathrm{h}$ are more spheroidal (the maximum is for $b/a \sim 0.75$) than the population with $P = 4 - 8\,\mathrm{h}$ (the maximum is for $b/a \sim 0.6$).

3. We constructed distributions of b/a for 13 most populous dynamical families. We revealed two families in the inner belt, Massalia and Phocaea, to be significantly different from their background. Both families have members that are more elongated than corresponding backgrounds. One possible explanation is that such result is due to the dependence of shape elongation on the rotation period.

4. By analyzing data in the i-filter we confirmed previous results and we did not found any significant differences between populations studied in the w-filter in comparison with the i-filter.

Bibliography

Belton M. J. S., Veverka J., Thomas P., Helfenstein P., Simonelli D., et al. (1992). Galileo encounter with 951 Gaspra - First pictures of an asteroid. *Science*, 257, 1647–1652.

Benner L. A. M., Busch M. W., Giorgini J. D., Taylor P. A., and Margot J.-L. (2015). Radar Observations of Near-Earth and Main-Belt Asteroids. In *Asteroids IV* (Michel P., DeMeo F. E., and Bottke W. F., editors). pp. 165–182.

Bottke, Jr. W. F., Vokrouhlický D., Rubincam D. P., and Broz M. (2002). The Effect of Yarkovsky Thermal Forces on the Dynamical Evolution of Asteroids and Meteoroids. In *Asteroids III* (Bottke, Jr. W. F., Cellino A., Paolicchi P., and Binzel R. P., editors). pp. 395–408.

Bowell E., Koehn B. W., Howell S. B., Hoffman M., and Muinonen K. (1995). The Lowell Observatory Near-Earth-Object Search: A Progress Report. In *AAS/Division for Planetary Sciences Meeting Abstracts #27*, volume 27 of *Bulletin of the American Astronomical Society*, p. 1057.

Bowell E., Oszkiewicz D. A., Wasserman L. H., Muinonen K., Penttilä A., et al. (2014). Asteroid spin-axis longitudes from the Lowell Observatory database. *Meteoritics and Planetary Science*, 49, 95–102.

Brouwer D. and Clemence G. M. (1961). *Methods of celestial mechanics*.

Busch M. W., Kulkarni S. R., Brisken W., Ostro S. J., Benner L. A. M., et al. (2010). Determining asteroid spin states using radar speckles. *Icarus*, 209, 535–541.

Callahan S., Gressler W., Thomas S. J., Gessner C., Warner M., et al. (2016). Large Synoptic Survey Telescope mount final design. In *Ground-based and Airborne Telescopes VI*, volume 9906 of *Proceedings of the SPIE*, p. 99060M.

Čapek D. and Vokrouhlický D. (2004). The YORP effect with finite thermal conductivity. *Icarus*, 172, 526–536.

Carry B. (2012). Density of asteroids. *Planetary and Space Science*, 73, 98–118.

Carvano J. M., Hasselmann P. H., Lazzaro D., and Mothé-Diniz T. (2010). SDSS-based taxonomic classification and orbital distribution of main belt asteroids. *Astronomy and Astrophysics*, 510, A43.

Chesley S., Farnocchia D., Pravec P., and Vokrouhlicky D. (2015). Direct Detections of the Yarkovsky Effect: Status and Outlook. *IAU General Assembly*, 22, 2248872.

Chesley S. R., Ostro S. J., Vokrouhlický D., Čapek D., Giorgini J. D., et al. (2003). Direct Detection of the Yarkovsky Effect by Radar Ranging to Asteroid 6489 Golevka. *Science*, 302, 1739–1742.

Cibulková H., Nortunen H., Ďurech J., Kaasalainen M., Vereš P., et al. (2017). Distribution of shape elongations of main belt asteroids derived from Pan-STARRS1 photometry. *Astronomy and Astrophysics, submitted*.

Cibulková H., Brož M., and Benavidez P. G. (2014). A six-part collisional model of the main asteroid belt. *Icarus*, 241, 358–372.

Cibulková H., Ďurech J., Vokrouhlický D., Kaasalainen M., and Oszkiewicz D. A. (2016). Distribution of spin-axes longitudes and shape elongations of main-belt asteroids. *Astronomy and Astrophysics*, 596, A57.

Colombo G. (1966). Cassini's second and third laws. *Astronomical Journal*, 71, 891.

Connelly R. and Ostro S. J. (1984). Ellipsoids and lightcurves. *NASA STI/Recon Technical Report A*, 85, 87–98.

Davis D. R., Weidenschilling S. J., Farinella P., Paolicchi P., and Binzel R. P. (1989). Asteroid collisional history - Effects on sizes and spins. In *Asteroids II* (Binzel R. P., Gehrels T., and Matthews M. S., editors), pp. 805–826.

Davison A. C. and Hinkley D. V. (1997). *Boostrap methods and their applications*. Cambridge University Press, New York.

DeMeo F. E., Alexander C. M. O., Walsh K. J., Chapman C. R., and Binzel R. P. (2015). The Compositional Structure of the Asteroid Belt. In *Asteroids IV* (Michel P., DeMeo F. E., and Bottke W. F., editors). pp. 13–41.

DeMeo F. E., Binzel R. P., Slivan S. M., and Bus S. J. (2009). An extension of the Bus asteroid taxonomy into the near-infrared. *Icarus*, 202, 160–180.

DeMeo F. E. and Carry B. (2014). Solar System evolution from compositional mapping of the asteroid belt. *Nature*, 505, 629–634.

Dermott S. F., Durda D. D., Grogan K., and Kehoe T. J. J. (2002). Asteroidal Dust. In *Asteroids III* (Bottke, Jr. W. F., Cellino A., Paolicchi P., and Binzel R. P., editors). pp. 423–442.

Drake A. J., Beshore E., Djorgovski S. G., Larson S., Boattini A., et al. (2012). The First Data Release of the Catalina Surveys. In *American Astronomical Society Meeting Abstracts #219*, volume 219 of *American Astronomical Society Meeting Abstracts*, p. 428.20.

Dunham D. W., Herald D., Frappa E., Hayamizu T., Talbot J., et al. (2014). Asteroid Occultations V12.0. *NASA Planetary Data System*, 216.

Ďurech J., Grav T., Jedicke R., Denneau L., and Kaasalainen M. (2005). Asteroid Models from the Pan-STARRS Photometry. *Earth Moon and Planets*, 97, 179–187.

Ďurech J., Scheirich P., Kaasalainen M., Grav T., Jedicke R., et al. (2007). Physical models of asteroids from sparse photometric data. In *IAU Symposium* (Valsecchi G. B., Vokrouhlický D., and Milani A., editors), volume 236 of *IAU Symposium*, pp. 191–200.

Ďurech J., Kaasalainen M., Warner B. D., Fauerbach M., Marks S. A., et al. (2009). Asteroid models from combined sparse and dense photometric data. *Astronomy and Astrophysics*, 493, 291–297.

Ďurech J., Sidorin V., and Kaasalainen M. (2010). DAMIT: a database of asteroid models. *Astronomy and Astrophysics*, 513, A46.

Ďurech J., Kaasalainen M., Herald D., Dunham D., Timerson B., et al. (2011). Combining asteroid models derived by lightcurve inversion with asteroidal occultation silhouettes. *Icarus*, 214, 652–670.

Ďurech J., Carry B., Delbo M., Kaasalainen M., and Viikinkoski M. (2015a). Asteroid Models from Multiple Data Sources. In *Asteroids IV* (Michel P., DeMeo F. E., and Bottke W. F., editors). pp. 183–202.

Ďurech J., Hanuš J., and Vančo R. (2015b). Asteroids@home-A BOINC distributed computing project for asteroid shape reconstruction. *Astronomy and Computing*, 13, 80–84.

Ďurech J., Hanuš J., Oszkiewicz D., and Vančo R. (2016). Asteroid models from the Lowell photometric database. *Astronomy and Astrophysics*, 587, A48.

Farinella P., Vokrouhlický D., and Hartmann W. K. (1998). Meteorite Delivery via Yarkovsky Orbital Drift. *Icarus*, 132, 378–387.

Farnocchia D., Chesley S. R., Chodas P. W., Micheli M., Tholen D. J., et al. (2013a). Yarkovsky-driven impact risk analysis for asteroid (99942) Apophis. *Icarus*, 224, 192–200.

Farnocchia D., Chesley S. R., Vokrouhlický D., Milani A., Spoto F., et al. (2013b). Near Earth Asteroids with measurable Yarkovsky effect. *Icarus*, 224, 1–13.

Gladman B. J., Migliorini F., Morbidelli A., Zappala V., Michel P., et al. (1997). Dynamical lifetimes of objects injected into asteroid belt resonances. *Science*, 277, 197–201.

Hanuš J., Delbo M., Alí-Lagoa V., Bolin B., Jedicke R., et al. (2017a). Spin states of asteroids in the Eos collisional family. *Icarus, in press.*

Hanuš J., Ďurech J., Brož M., Marciniak A., Warner B. D., et al. (2013). Asteroids' physical models from combined dense and sparse photometry and scaling of the YORP effect by the observed obliquity distribution. *Astronomy and Astrophysics*, 551, A67.

Hanuš J., Ďurech J., Brož M., Warner B. D., Pilcher F., et al. (2011). A study of asteroid pole-latitude distribution based on an extended set of shape models derived by the lightcurve inversion method. *Astronomy and Astrophysics*, 530, A134.

Hanuš J., Ďurech J., Oszkiewicz D. A., Behrend R., Carry B., et al. (2016). New and updated convex shape models of asteroids based on optical data from a large collaboration network. *Astronomy and Astrophysics*, 586, A108.

Hanuš J., Viikinkoski M., Marchis F., Ďurech J., Kaasalainen M., et al. (2017b). Volumes and bulk densities of forty asteroids from ADAM shape modeling. *Astronomy and Astrophysics*, 601, A114.

Hapke B. (1981). Bidirectional reflectance spectroscopy. 1. Theory. *Journal of Geophysical Research*, 86, 4571–4586.

Hapke B. (1993). *Theory of reflectance and emittance spectroscopy.* UK: Cambridge University Press.

Henrard J. and Murigande C. (1987). Colombo's top. *Celestial Mechanics*, 40, 345–366.

Hestroffer D. and Tanga P. (2006). Asteroids from Observations to Models. In *Dynamics of Extended Celestial Bodies and Rings* (Souchay J., editor), volume 682 of *Lecture Notes in Physics, Berlin Springer Verlag*, p. 89.

Hirayama K. (1918). Groups of asteroids probably of common origin. *Astronomical Journal*, 31, 185–188.

Hodapp K. W., Kaiser N., Aussel H., Burgett W., Chambers K. C., et al. (2004). Design of the Pan-STARRS telescopes. *Astronomische Nachrichten*, 325, 636–642.

JeongAhn Y. and Malhotra R. (2014). On the non-uniform distribution of the angular elements of near-Earth objects. *Icarus*, 229, 236–246.

Kaasalainen M. (2004). Physical models of large number of asteroids from calibrated photometry sparse in time. *Astronomy and Astrophysics*, 422, L39–L42.

Kaasalainen M. and Torppa J. (2001). Optimization Methods for Asteroid Lightcurve Inversion. I. Shape Determination. *Icarus*, 153, 24–36.

Kaasalainen M., Torppa J., and Muinonen K. (2001). Optimization Methods for Asteroid Lightcurve Inversion. II. The Complete Inverse Problem. *Icarus*, 153, 37–51.

Kaasalainen M., Ďurech J., Warner B. D., Krugly Y. N., and Gaftonyuk N. M. (2007). Acceleration of the rotation of asteroid 1862 Apollo by radiation torques. *Nature*, 446, 420–422.

Kaasalainen M. and Viikinkoski M. (2012). Shape reconstruction of irregular bodies with multiple complementary data sources. *Astronomy and Astrophysics*, 543, A97.

Knežević Z. and Milani A. (2003). Proper element catalogs and asteroid families. *Astronomy and Astrophysics*, 403, 1165–1173.

Kryszczyńska A., La Spina A., Paolicchi P., Harris A. W., Breiter S., et al. (2007). New findings on asteroid spin-vector distributions. *Icarus*, 192, 223–237.

Kuchynka P. and Folkner W. M. (2013). A new approach to determining asteroid masses from planetary range measurements. *Icarus*, 222, 243–253.

La Spina A., Paolicchi P., Kryszczyńska A., and Pravec P. (2004). Retrograde spins of near-Earth asteroids from the Yarkovsky effect. *Nature*, 428, 400–401.

Li J.-Y., Helfenstein P., Buratti B., Takir D., and Clark B. E. (2015). Asteroid Photometry. In *Asteroids IV* (Michel P., DeMeo F. E., and Bottke W. F., editors). pp. 129–150.

Lowry S. C., Fitzsimmons A., Pravec P., Vokrouhlický D., Boehnhardt H., et al. (2007). Direct Detection of the Asteroidal YORP Effect. *Science*, 316, 272.

Lumme K. and Bowell E. (1981). Radiative transfer in the surfaces of atmosphereless bodies. I - Theory. II - Interpretation of phase curves. *Astronomical Journal*, 86, 1694–1721.

Magnusson P. (1986). Distribution of spin axes and senses of rotation for 20 large asteroids. *Icarus*, 68, 1–39.

Mainzer A., Grav T., Bauer J., Masiero J., McMillan R. S., et al. (2011a). NEOWISE Observations of Near-Earth Objects: Preliminary Results. *Astrophysical Journal*, 743, 156.

Mainzer A., Grav T., Masiero J., Bauer J., Wright E., et al. (2011b). Thermal Model Calibration for Minor Planets Observed with Wide-field Infrared Survey Explorer/NEOWISE. *Astrophysical Journal*, 736, 100.

Marciniak A., Pilcher F., Oszkiewicz D., Santana-Ros T., Urakawa S., et al. (2015). Against the biases in spins and shapes of asteroids. *Planetary and Space Science*, 118, 256–266.

Masiero J. R., Mainzer A. K., Grav T., Bauer J. M., Cutri R. M., et al. (2011). Main Belt Asteroids with WISE/NEOWISE. I. Preliminary Albedos and Diameters. *Astrophysical Journal*, 741, 68.

McNeill A., Fitzsimmons A., Jedicke R., Wainscoat R., Denneau L., et al. (2016). Brightness variation distributions among main belt asteroids from sparse lightcurve sampling with Pan-STARRS 1. *Monthly Notices of the Royal Astronomical Society*, 459, 2964–2972.

Milani A., Nobili A. M., and Knežević Z. (1997). Stable Chaos in the Asteroid Belt. *Icarus*, 125, 13–31.

Moons M., Morbidelli A., and Migliorini F. (1998). Dynamical Structure of the 2/1 Commensurability with Jupiter and the Origin of the Resonant Asteroids. *Icarus*, 135, 458–468.

Morbidelli A., Bottke W. F., Nesvorný D., and Levison H. F. (2009). Asteroids were born big. *Icarus*, 204, 558–573.

Morbidelli A., Bottke, Jr. W. F., Froeschlé C., and Michel P. (2002). Origin and Evolution of Near-Earth Objects. In *Asteroids III* (Bottke, Jr. W. F., Cellino A., Paolicchi P., and Binzel R. P., editors). pp. 409–422.

Morbidelli A., Walsh K. J., O'Brien D. P., Minton D. A., and Bottke W. F. (2015). The Dynamical Evolution of the Asteroid Belt. In *Asteroids IV* (Michel P., DeMeo F. E., and Bottke W. F., editors). pp. 493–507.

Muinonen K., Piironen J., Shkuratov Y. G., Ovcharenko A., and Clark B. E. (2002). Asteroid Photometric and Polarimetric Phase Effects. In *Asteroids III* (Bottke, Jr. W. F., Cellino A., Paolicchi P., and Binzel R. P., editors). pp. 123–138.

Nesvorný D., Brož M., and Carruba V. (2015). Identification and Dynamical Properties of Asteroid Families. In *Asteroids IV* (Michel P., DeMeo F. E., and Bottke W. F., editors), pp. 297–321. University of Arizona Press.

Nesvorný D., Jedicke R., Whiteley R. J., and Ivezić Ž. (2005). Evidence for asteroid space weathering from the Sloan Digital Sky Survey. *Icarus*, 173, 132–152.

Nesvorný D. and Morbidelli A. (1998). Three-Body Mean Motion Resonances and the Chaotic Structure of the Asteroid Belt. *Astronomical Journal*, 116, 3029–3037.

Nortunen H. and Kaasalainen M. (2017). LEADER: fast estimates of asteroid shape elongation and spin latitude distributions from scarce photometry. *Astronomy and Astrophysics, submitted*.

Nortunen H., Kaasalainen M., Ďurech J., Cibulková H., Ali-Lagoa V., et al. (2017). Shape and spin distributions of asteroid populations from brightness variation estimates and large databases. *Astronomy and Astrophysics*, 601, A139.

Ostro S. J., Hudson R. S., Benner L. A. M., Giorgini J. D., Magri C., et al. (2002). Asteroid Radar Astronomy. In *Asteroids III* (Bottke, Jr. W. F., Cellino A., Paolicchi P., and Binzel R. P., editors). pp. 151–168.

Ostro S. J., Hudson R. S., Nolan M. C., Margot J.-L., Scheeres D. J., et al. (2000). Radar Observations of Asteroid 216 Kleopatra. *Science*, 288, 836–839.

Oszkiewicz D. A., Muinonen K., Bowell E., Trilling D., Penttilä A., et al. (2011). Online multi-parameter phase-curve fitting and application to a large corpus of asteroid photometric data. *Journal of Quantitative Spectroscopy & Radiative Transfer*, 112, 1919–1929.

Pravec P. and Harris A. W. (2000). Fast and Slow Rotation of Asteroids. *Icarus*, 148, 12–20.

Pravec P., Harris A. W., and Michalowski T. (2002). Asteroid Rotations. *Asteroids III*, pp. 113–122.

Pravec P., Harris A. W., Vokrouhlický D., Warner B. D., Kušnirák P., et al. (2008). Spin rate distribution of small asteroids. *Icarus*, 197, 497–504.

Pravec P., Harris A. W., and Warner B. D. (2007). NEA rotations and binaries. In *Near Earth Objects, our Celestial Neighbors: Opportunity and Risk* (Valsecchi G. B., Vokrouhlický D., and Milani A., editors), volume 236 of *IAU Symposium*, pp. 167–176.

Rubincam D. P. (2000). Radiative Spin-up and Spin-down of Small Asteroids. *Icarus*, 148, 2–11.

Santana-Ros T., Bartczak P., Michałowski T., Tanga P., and Cellino A. (2015). Testing the inversion of asteroids' Gaia photometry combined with ground-based observations. *Monthly Notices of the Royal Astronomical Society*, 450, 333–341.

Scheeres D. J., Fahnestock E. G., Ostro S. J., Margot J.-L., Benner L. A. M., et al. (2006). Dynamical Configuration of Binary Near-Earth Asteroid (66391) 1999 KW4. *Science*, 314, 1280–1283.

Schlafly E. F., Finkbeiner D. P., Jurić M., Magnier E. A., Burgett W. S., et al. (2012). Photometric Calibration of the First 1.5 Years of the Pan-STARRS1 Survey. *Astrophysical Journal*, 756, 158.

Shibai H. (2007). AKARI (ASTRO-F): Flight performance and preliminary results. *Advances in Space Research*, 40, 595–599.

Skoglöv E. and Erikson A. (2002). The Influence of the Orbital Evolution of Main Belt Asteroids on Their Spin Vectors. *Icarus*, 160, 24–31.

Slivan S. M. (2002). Spin vector alignment of Koronis family asteroids. *Nature*, 419, 49–51.

Slivan S. M., Binzel R. P., Crespo da Silva L. D., Kaasalainen M., Lyndaker M. M., et al. (2003). Spin vectors in the Koronis family: comprehensive results from two independent analyses of 213 rotation lightcurves. *Icarus*, 162, 285–307.

Szabó G. M. and Kiss L. L. (2008). The shape distribution of asteroid families: Evidence for evolution driven by small impacts. *Icarus*, 196, 135–143.

Szabó R., Pál A., Sárneczky K., Szabó G. M., Molnár L., et al. (2016). Uninterrupted optical light curves of main-belt asteroids from the K2 mission. *Astronomy and Astrophysics*, 596, A40.

Taylor P. A., Margot J.-L., Vokrouhlický D., Scheeres D. J., Pravec P., et al. (2007). Spin Rate of Asteroid (54509) 2000 PH5 Increasing Due to the YORP Effect. *Science*, 316, 274.

Tedesco E. F., Matson D. L., Veeder G. J., and Lebofsky L. A. (1988). IRAS Observations of Asteroids. In *Comets to Cosmology* (Lawrence A., editor), volume 297 of *Lecture Notes in Physics, Berlin Springer Verlag*, p. 19.

Timerson B., Durech J., Aguirre S., Benner L., Blacnhette D., et al. (2009). A Trio of Well-Observed Asteroid Occultations in 2008. *Minor Planet Bulletin*, 36, 98–100.

Tonry J. L., Stubbs C. W., Lykke K. R., Doherty P., Shivvers I. S., et al. (2012). The Pan-STARRS1 Photometric System. *Astrophysical Journal*, 750, 99.

Usui F., Kuroda D., Müller T. G., Hasegawa S., Ishiguro M., et al. (2011). Asteroid Catalog Using Akari: AKARI/IRC Mid-Infrared Asteroid Survey. *Publications of the Astronomical Society of Japan*, 63, 1117–1138.

Veverka J., Belton M., Klaasen K., and Chapman C. (1994). Galileo's Encounter with 951 Gaspra: Overview. *Icarus*, 107, 2–17.

Veverka J., Farquhar B., Robinson M., Thomas P., Murchie S., et al. (2001). The landing of the NEAR-Shoemaker spacecraft on asteroid 433 Eros. *Nature*, 413, 390–393.

Vokrouhlický D., Nesvorný D., and Bottke W. F. (2003). The vector alignments of asteroid spins by thermal torques. *Nature*, 425, 147–151.

Vokrouhlický D., Nesvorný D., and Bottke W. F. (2006). Secular spin dynamics of inner main-belt asteroids. *Icarus*, 184, 1–28.

Vraštil J. and Vokrouhlický D. (2015). Inner main belt asteroids in Slivan states? *Astronomy and Astrophysics*, 579, A14.

Warner B. D., Harris A. W., and Pravec P. (2009). The asteroid lightcurve database. *Icarus*, 202, 134–146.

Zappala V., Cellino A., Farinella P., and Knezevic Z. (1990). Asteroid families. I - Identification by hierarchical clustering and reliability assessment. *Astronomical Journal*, 100, 2030–2046.

List of papers

Title: **A six-part collisional model of the main asteroid belt**
Authors: Cibulková, H.; Brož, M.; Benavidez, P. G.

Title: **Distribution of spin-axes longitudes and shape elongations of main-belt asteroids**
Authors: Cibulková, H.; Ďurech, J.; Vokrouhlický, D.; Kaasalainen, M.; Oszkiewicz, D. A.

Title: **Distribution of shape elongations of main belt asteroids derived from Pan-STARRS1 photometry**
Authors: Cibulková, H.; Nortunen, H.; Ďurech, J.; Kaasalainen, M.; Vereš, P.; Jedicke, R.; Wainscoat, R. J.; Mommert, M.; et al.

Title: **Spin states of asteroids in the Eos collisional family**
Authors: Hanuš, J.; Delbo, M.; Alí-Lagoa, V.; Bolin, B.; Jedicke, R.; Ďurech, J.; Cibulková, H.; Pravec, P.; Kušnirák, P.; Behrend, R.; et al.
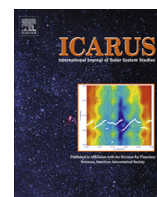
Title: **Shape and spin distributions of asteroid populations from brightness variation estimates and large databases**
Authors: Nortunen, H.; Kaasalainen, M.; Ďurech, J.; Cibulková, H.; Ali-Lagoa, V.; Hanuš, J.

Paper 1

A six-part collisional model of the main asteroid belt

H. Cibulková [a,*], M. Brož [a], P.G. Benavidez [b]

[a] Institute of Astronomy, Charles University in Prague, V Holešovičkách 2, 18000 Prague 8, Czech Republic
[b] Departamento de Física, Ingeniería de Sistemas y Teoría de la Señal, Universidad de Alicante, P.O. Box 99, 03080 Alicante, Spain

ARTICLE INFO

ABSTRACT

In this work, we construct a new model for the collisional evolution of the main asteroid belt. Our goals are to test the scaling law of Benz and Asphaug (Benz, W., Asphaug, E. [1999]. Icarus, 142, 5–20) and ascertain if it can be used for the whole belt. We want to find initial size–frequency distributions (SFDs) for the considered six parts of the belt (inner, middle, "pristine", outer, Cybele zone, high-inclination region) and to verify if the number of synthetic asteroid families created during the simulation matches the number of observed families as well. We used new observational data from the WISE satellite (Masiero et al., 2011) to construct the observed SFDs. We simulate mutual collisions of asteroids with a modified version of the Boulder code (Morbidelli, A., et al. [2009]. Icarus, 204, 558–573), where the results of hydrodynamic (SPH) simulations of Durda et al. (Durda, D.D., et al. [2007]. Icarus, 498–516) and Benavidez et al. (Benavidez, P.G., et al. [2012]. 219, 57–76) are included. Because material characteristics can significantly affect breakups, we created two models — for monolithic asteroids and for rubble-piles. To explain the observed SFDs in the size range $D = 1$ to 10 km we have to also account for dynamical depletion due to the Yarkovsky effect. The assumption of (purely) rubble-pile asteroids leads to a significantly worse fit to the observed data, so that we can conclude that majority of main-belt asteroids are rather monolithic. Our work may also serve as a motivation for further SPH simulations of disruptions of smaller targets (with a parent body size of the order of 1 km).

1. Introduction

The collisional evolution of the main asteroid belt has been studied for more than 60 years (Dohnanyi, 1969; Davis et al., 1979 etc.). The first collisional model was created by Dohnanyi (1969) and his important result was that a size–frequency distribution for a population of mutually colliding asteroids will reach an equilibrium. If the cumulative distribution is described by a power law, the corresponding slope (exponent) will be close to −2.5. An overview of previous modeling of the main belt and subsequent advances can be found in a relatively recent paper by Bottke et al. (2005), so that we shall not repeat it here. Nevertheless, it is worth to mention another development, which is an attempt to merge a classical particle-in-a-box collisional model with (parametrized) results of smooth-particle hydrodynamic (SPH) codes as done in Morbidelli et al. (2009). We are going to use this kind of method in this work.

Every collisional model should comply with two important constraints: (1) the size–frequency distribution (SFD) of main belt at

the end of a simulation must fit the observed SFD; (2) the number of asteroid families created during this simulation must fit the observed number of families. It is important to note, that the models were improved in the course of time not only due to the progress of technology or new methods but also thanks to an increasing amount of observational data. In this work, we could exploit new data obtained by the WISE satellite (Wide-field Infrared Survey Explorer; Masiero et al., 2011), specifically, diameters and geometric albedos for 129,750 asteroids.

Moreover, several tens of asteroid families are observed in the main belt as shown by many authors (Zappalà et al., 1995; Nesvorný et al., 2005, 2010; Brož et al., 2013; Masiero et al., 2013; Milani et al., 2013). The lists of collisional families are also steadily improved, they become more complete and (luckily) compatible with each other.

In order to fully exploit all new data, we created a new collisional model in which we divided the whole main belt into six parts (see Section 2 for a detailed discussion and Section 3 for the description of observational data). Our aims are: (1) to check the number of families in individual parts of the belt — we use the list of families from Brož et al. (2013) (which includes also their physical properties) with a few modifications; (2) to verify whether a single scaling law (e.g. Benz and Asphaug, 1999) can

be used to fit the *whole* asteroid belt, or it is necessary to use two different scaling laws, e.g. one for the inner belt and second for the outer belt; (3) and we also test a hypothesis, if the main belt is mostly composed of monolithic or rubble-pile objects.

In this paper, we assume that *all* families observed today were created in the last ~4 Gyr (without any influence of the late heavy bombardment dated approximately 4.2 to 3.85 Gyr ago).[1] We thus focus on an almost steady-state evolution of the main belt, without any significant changes of collisional probabilities or dynamical characteristics. This is different from the work of Bottke et al. (2005). We must admit here that the assumption of the steady-state evolution could be disputable, since Dell'Oro et al. (2001) showed that the formation of big asteroid families may influence the impact probability.

We model collisions with the statistical code called Boulder (Morbidelli et al., 2009) that we slightly extended to account for six populations of asteroids (Sections 5 and 6). As mentioned above, the Boulder code incorporates the results of the SPH simulations by Durda et al. (2007) for *monolithic* $D_{PB} = 100$ km parent bodies, namely for the masses of the largest remnant and fragment and an overall slope of fragment's SFD. For asteroids larger or smaller than $D_{PB} = 100$ km a scaling is used for sake of simplicity.

Material characteristics definitely have significant influence on mutual collisions (e.g. Michel et al., 2011; Benavidez et al., 2012). Therefore, we also run simulations with *rubble-pile* objects, which are less firm (refer to Section 7). A set of simulations analogous to Durda et al. (2007) for rubble-pile targets with $D_{PB} = 100$ km was computed by Benavidez et al. (2012).

First, we try to explore the parameter space using a simplex algorithm while we keep the scaling law fixed. Considering a large number of free parameters and the stochasticity of the system, we look only for some local minima of χ^2 and we do not expect to find a statistically significant global minimum. Further possible improvements and extensions of our model are discussed in Sections 8 and 9.

2. A definition of the six parts of the main belt

We divided the main belt into six parts (sub-populations) according the synthetic orbital elements (the semimajor axis a and the inclination I, Fig. 1). Five parts separated by major mean-motion resonances with Jupiter are well-defined — if an asteroid enters a resonance due to the Yarkovsky effect (Bottke et al., 2006), its eccentricity increases and the asteroid becomes a near-Earth object. Consequently, vast majority of large asteroids do not cross the resonances[2] and we do not account for resonance crossing in our model. The sixth part is formed by asteroids with high inclinations, $\sin I_p > 0.34$. This value corresponds approximately to the position of the ν_6 secular resonance.

Namely, the individual parts are defined as follows:

1. inner belt – from $a = 2.1$ to 2.5 AU (i.e. the resonance 3:1);
2. middle belt – from 2.5 to 2.823 AU (5:2);

Fig. 1. A definition of the six parts of the main asteroids belt according to the semimajor axis a and the inclination I: inner, middle, "pristine", outer, Cybele zone and high-inclination region. The numbers of objects in these parts are the following: 177,756; 186,307; 23,132; 121,186; 1894 and 25,501, respectively.

3. "pristine" belt – from 2.823 to 2.956 AU (7:3; as explained in Brož et al. (2013));
4. outer belt – from 2.956 to 3.28 AU (2:1);
5. Cybele zone – from 3.3 to 3.51 AU;
6. high-inclination region – $\sin I > 0.34$.

For a and $\sin I$ we preferentially used the proper values from the AstDyS catalog (Asteroids Dynamic Site; Knežević and Milani, 2003).[3] For remaining asteroids, not included in AstDyS, we used osculating orbital elements from the AstOrb catalog (The Asteroid Orbital Elements Database).[4]

More precisely, we used proper values from AstDyS for 403,674 asteroids and osculating values from AstOrb for 132,102 not-yet-numbered (rather small) asteroids, which is a minority. We thus think that mixing of proper and osculating orbital elements cannot affect the respective size–frequency distributions in a significant way. Moreover, if we assign (erroneously) e.g. a high-inclination asteroid to the outer main belt, then it is statistically likely that another asteroid from the outer main belt may be assigned (erroneously) to the high-inclination region, so that overall the SFDs remain almost the same.

3. Observed size–frequency distributions

To construct SFDs we used the observational data from the WISE satellite (Masiero et al., 2011)[5] — for 123,306 asteroids. Typical diameter and albedo relative uncertainties are ~10% and ~20%, respectively (Mainzer et al., 2011), but since we used a statistical approach (10^4 to 10^5 bodies), this should not present a problem. For asteroids not included there we could exploit the AstOrb catalog (i.e. data from IRAS; Tedesco et al., 2002) — for 451 bodies. For remaining asteroids (412,019), we calculated their diameters according the relation (Bowell et al., 1989)

$$D = 10^{0.5(6.259-\log p_V)-0.4H},\tag{1}$$

where H denotes the absolute magnitude from the AstOrb catalog and p_V the (assumed) geometric albedo. We assigned albedos to asteroids without a known diameter randomly, by a Monte-Carlo method, from the distributions of albedos constructed according

---

[1] This is an approach different from Brož et al. (2013), where (at most) 5 large ($D_{PB} > 200$ km) catastrophic disruptions were attributed to the LHB. Nevertheless, there was a possibility (at a few-percent level) that all the families were created without the LHB. So our assumptions here do not contradict Brož et al. (2013) and we will indeed discuss a possibility that the number of post-LHB families is lower than our 'nominal' value.

[2] For very small asteroids ($D \lesssim 10$ m) we must be more careful. Nevertheless, if an asteroid is able to cross the resonance between e.g. the pristine and the middle belt (i.e. increasing the population of the middle belt) then another asteroid is able to cross the resonance between the middle and the inner belt (decreasing the population of the middle belt). The crossing of the resonances essentially corresponds to a longer time scale of the dynamical decay, which we shall discuss in Section 8.
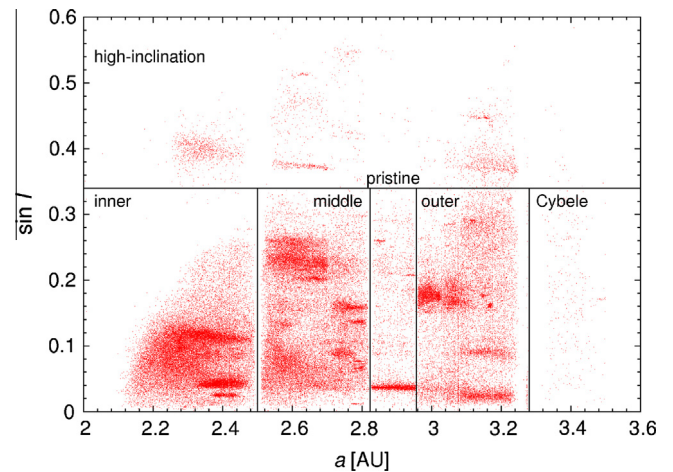
[3] http://hamilton.dm.unipi.it/astdys/.
[4] ftp://ftp.lowell.edu/pub/elgb/astorb.html.
[5] http://wise2.ipac.caltech.edu/staff/bauer/NEOWISE_pass1/.

to the WISE data. Differences in albedo distributions can influence the resulting SFDs, therefore for each part of the main belt, we constructed a distribution of albedos separately.

We checked that the WISE distributions of albedos are (within a few percent) in agreement with the distributions found by Tedesco et al. (2005). The (minor) differences can be attributed for example to a substantially larger sample (119,876 asteroids compared to 5983), which includes also a lot of asteroids with smaller sizes ($D \lesssim 10$ km). The resulting observed SFDs are shown in Fig. 2. We can see clearly that the individual SFDs differ significantly in terms of slopes and total numbers of asteroids.

To verify a validity of this method, we perform the following test (for the whole main belt). We assume a known set of diameters. We then assign albedos randomly to the individual diameters according to the distribution of WISE albedos. We calculate the values of the absolute magnitudes H by the inversion of Eq. (1). Now, we try to reconstruct the SFD from H and p_V. The new "unknown" values of diameters are computed according to Eq. (1) and for the values of p_V we test three following options: (1) a fixed albedo $p_V = 0.15$; (2) the mean value $p_V = 0.13$ (derived from the distribution of WISE albedos); (3) for $H < 15$ mag we used the known albedos, for other bodies we assigned albedos by the Monte-Carlo method as above. The known SFD and the three reconstructed SFDs are shown in Fig. 3.

The largest uncertainties of the reconstruction are given by the method of assignment of geometric albedos, but we verified that the third method is the best one and that these uncertainties (Fig. 3) are much smaller than the differences between individual SFDs (Fig. 2).

Another possible difficulty, especially for asteroids with diameters $D < 10$ km, is the observational bias. In Fig. 2, we can see that for sizes smaller than some D_{limit} the total number of asteroids remains constant. We also probably miss same asteroids with $D_{limit} < D < 10$ km. These objects are less bright than the reach of current surveys: LINEAR (Stuart, 2001), Catalina,[6] Spacewatch (Bottke et al., 2002), or Pan-STARRS (Hodapp et al., 2004). Nevertheless, for $D > 10$ km we do not need to perform debiasing and neither for smaller asteroids we do not account for the bias, because the range of diameters D where we fit out model is limited (see Table 4).

4. Collisional probabilities and impact velocities

To model the collisional evolution of the main belt by the Boulder code we need to know the intrinsic probabilities p_i of collisions between individual parts and the mutual impact velocities v_{imp}. The values of p_i and v_{imp} were computed by the code written by W.F. Bottke (Bottke and Greenberg, 1993; Greenberg, 1982). For this calculation, we used only the osculating elements from the AstOrb catalog.

We calculated p_i's and v_{imp}'s between each pair of asteroids of different populations. We used first 1000 asteroids from each population (first according to the catalog nomenclature). We checked that this selection does not significantly influence the result. We constructed the distributions of eccentricities and inclinations of first 1000 objects from each region and we verified that they approximately correspond with the distributions for the whole population. We also tried a different selection criterion (last 1000 orbits), but this changes neither p_i nor v_{imp} values substantially.

From these sets of p_i's and v_{imp}'s, we computed the mean values $\overline{p_i}$ and $\overline{v}_{imp}$ (for v_{imp} only if corresponding $p_i \neq 0$). We checked that the distributions are relatively close to the Gauss distribution and the computations of the mean values are reasonable.

We found out that the individual p_i and v_{imp} differ significantly (values from 0.35×10^{-18} to 11.98×10^{-18} km^{-2} yr^{-1} and from
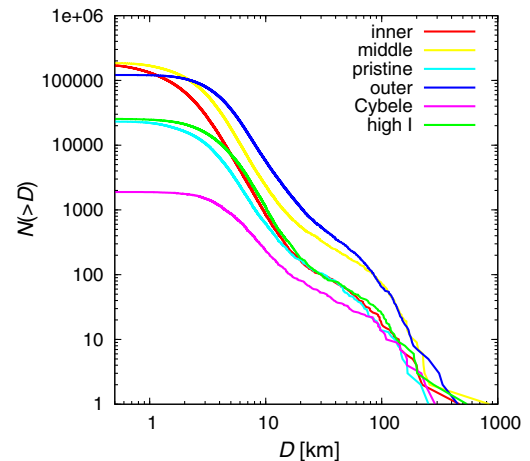
---

[6] http://www.lpl.arizona.edu/css/.

Fig. 2. The observed cumulative size–frequency distributions $N(> D)$ of the six parts of the main belt. We used the observational data from the WISE satellite (Masiero et al., 2011) and the AstOrb catalog for their construction. For asteroids which have no albedos in the WISE database, we assigned albedos by a Monte Carlo method from the distribution of WISE albedos.

2.22 to 10.09 km s^{-1}) — see Table 1. The collision probability decreases with an increasing difference between semimajor axis of two asteroids (the lowest value is for the interaction between the inner belt and the Cybele zone, while the highest for the interactions inside the inner belt). The highest impact velocities are for interactions between the high-inclination region and any other population.

The uncertainties of $\overline{p_i}$ are of the order 0.1×10^{-18} km^{-2} yr^{-1} and for $\overline{v}_{imp}$ about 0.1 km s^{-1}. Values computed by Dahlgren (1998), $p_i = 3.1 \times 10^{-18}$ km^{-2} yr^{-1} and $v_{imp} = 5.28$ km s^{-1} (mean values for the whole main belt), are in accordance with our results as well as values computed by Dell'Oro and Paolicchi (1998) — from 3.3 to 3.5×10^{-18} km^{-2} yr^{-1} (depending on assumptions for orbital angles distributions). However, it seems to be clear that considering only a single value of p_i and v_{imp} for the *whole* main belt would result in a systematic error of the model.

5. A construction of the model

In this section, we are going to describe free and fixed input parameters of our model, the principle how we explore the parameter space and we also briefly describe the Boulder code.

The initial SFDs of the six parts of the main belt are described by 36 free parameters — six for every part: q_a, q_b, q_c, d_1, d_2 and n_{norm}. Parameter q_a denotes the slope of the SFD for asteroids with diameters $D > d_1$, q_b the slope between d_1 and d_2, q_c the slope for $D < d_2$ (in other words, d_1 and d_2 are the diameters separating different power laws) and n_{norm} is the normalization of the SFD at d_1, i.e. the number of asteroids with $D > d_1$ (see also Table 4).

We must also "manually" add biggest asteroids, which likely stay untouched from their formation, to the input SFDs: (4) Vesta with a diameter 468.3 km (according to AstOrb) in the inner belt, (1) Ceres with a diameter 848.4 km (AstOrb) in the middle belt, and (2) Pallas with a diameter 544 km (Masiero et al., 2011) in the high-inclination region. These asteroids are too big and "solitary" in the respective part of the SFD and consequently cannot be described by the slope q_a.

The list of fixed input parameters is as follows: collision probabilities and impact velocities from Section 4; the scaling law parameters according to Benz and Asphaug (1999); initial (−4 Gyr) and final (0) time and the time step (10 Myr).
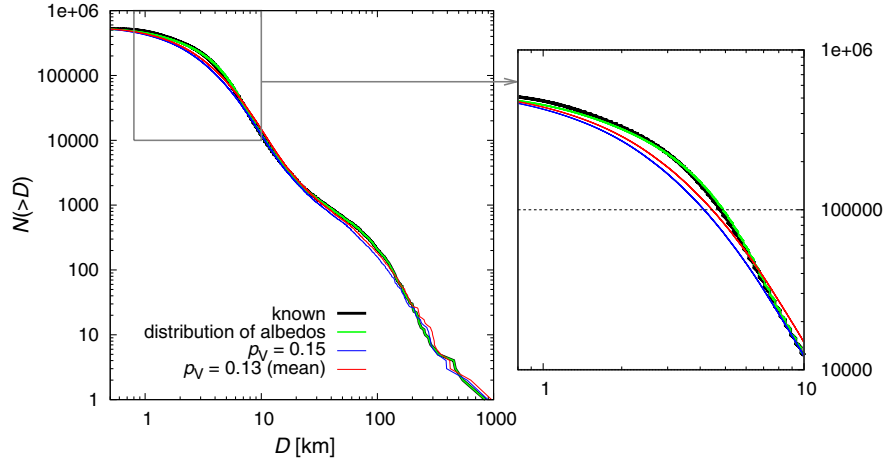
Fig. 3. A test of three reconstructions of a "known" size–frequency distribution. Diameters were calculated according to Eq. (1) and for values of p_V we try to use: (1) $p_v = 0.15$ (blue line), (2) $p_v = 0.13$, i.e. the mean value from the distribution of WISE albedos (red line), and (3) we used albedos from WISE for $H < 15$ mag; for other bodies we assigned albedos by a Monte-Carlo method according to the distribution of WISE albedos (green line). We can see that the third method is the best one. (For interpretation of the references to colour in this figure legend, the reader is referred to the web version of this article.)

5.1. The scaling law

One of the input parameters is the scaling law described by a parametric relation

$$Q_D^\star = \frac{1}{q_{fact}}(Q_0 r^a + B\rho r^b), \qquad (2)$$

where r denotes the radius in cm, ρ the density in g/cm³, parameters q_{fact}, Q_0 and B are the normalization parameters, a and b characterize the slope of the corresponding power law. $Q_D^\star$ is the specific impact energy required to disperse half of the total mass of a target. A scaling law which is often used is that of Benz and Asphaug (1999) (Fig. 4), which was derived on the basis of SPH simulations. Parameters in Eq. (2), corresponding to Benz and Asphaug (1999), are listed in Table 2.

In our simulations, we used three different scaling laws, one for monolithic bodies and two for rubble-pile bodies (to be studied in Section 7). Densities we assumed are within the ranges reported by Carry (2012) for major taxonomical classes (C-complex 1.3 to 2.9 g/cm³; S-complex 2 to 4 g/cm³; for X-types the interval is wide; see Fig. 7 or Table 3 therein).

5.2. A definition of the χ^2 metric

To measure a match between our simulations and the observations we calculate χ^2 prescribed by the relation

$$\chi^2 = \sum_{i=1}^{n} \frac{(syn_i - obs_i)^2}{\sigma_i^2}, \qquad (3)$$

where syn_i denotes the synthetic data (i.e. results from Boulder simulations) and obs_i denotes the observed data, σ_i is the uncertainty of the corresponding obs_i. The quantities syn_i and obs_i are namely the cumulative SFDs $N(> D)$ or the numbers of families $N_{families}$. More exactly, we calculate χ^2_{sfd} for the 96 points in the cumulative SFDs of the six populations (we verified that this particular choice does not influence our results) and we add χ^2_{fam} for the numbers of families in these populations.[7]

To minimize χ^2 we use a simplex numerical method (Press et al., 1992). Another approach we could use is a genetic algorithm which is not-so-prone to "fall" into a local minimum as simplex.

Table 1
The computed intrinsic collisional probabilities $\overline{p}_i$ and the mutual impact velocities $\overline{v}_{imp}$ (for v_{imp} only if $p_i \neq 0$) between objects belonging to the different parts of the main belt. The uncertainties are of the order 0.1×10^{-18} km⁻² yr⁻¹ for $\overline{p}_i$ and 0.1 km s⁻¹ for $\overline{v}_{imp}$.

Interacting populations	$\overline{p}_i$ (10^{-18} km⁻² yr⁻¹)	$\overline{v}_{imp}$ (km s⁻¹)
Inner–inner	11.98	4.34
Inner–middle	5.35	4.97
Inner–pristine	2.70	3.81
Inner–outer	1.38	4.66
Inner–Cybele	0.35	6.77
Inner–high Inc.	2.93	9.55
Middle–middle	4.91	5.18
Middle–pristine	4.67	3.96
Middle–outer	2.88	4.73
Middle–Cybele	1.04	5.33
Middle–high Inc.	2.68	8.84
Pristine–pristine	8.97	2.22
Pristine–outer	4.80	3.59
Pristine–Cybele	1.37	4.57
Pristine–high Inc.	2.45	7.93
Outer–outer	3.57	4.34
Outer–Cybele	2.27	4.45
Outer–high Inc.	1.81	8.04
Cybele–Cybele	2.58	4.39
Cybele–high Inc.	0.98	7.87
High Inc.–high Inc.	2.92	10.09

Nevertheless, we decided to rather explore the parameter space in a more systematic/controlled way and we start the simplex many times with (729) different initial conditions. We thus do not rely on a single local minimum.

The χ^2 prescribed by Eq. (3) is clearly not a "classical" χ^2, but a "pseudo"-χ^2, because we do not have a well-determined σ_i.[8] Using χ^2 we can only decide, if our model corresponds to the observations within the prescribed uncertainties σ_i. Specifically, we used $\sigma_i = 10\%$, obs_i for the SFDs[9] (similarly as Bottke et al. (2005)) and $\sigma_i = \sqrt{obs_i}$ for the families.

---

[7] We should mention that more sophisticated techniques of assessing the goodness-of-fit (based on bi-truncated Pareto distributions and maximum likelihood techniques) exist, as pointed out by Cellino et al. (1991).

[8] We *cannot* use a usual condition $\chi^2 \approx n$ or the probability function $q(\chi^2|n)$ to asses a statistical significance of the match between the synthetic and observed data.

[9] We prefer to use cumulative values $N(> D)$ instead of differential, even though the bins are not independent of each other. The reason is more-or-less technical: the Boulder code can create new bins (or merge existing bins) in the course of simulation and this would create a numerical artefact in the χ^2 computation.
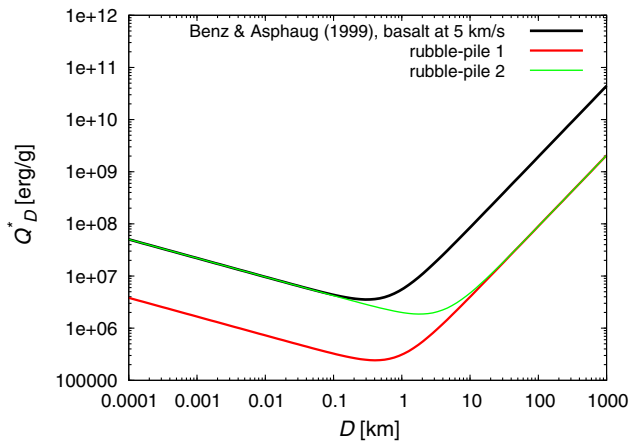
Fig. 4. The scaling law for basaltic material at 5 km/s (black line) according to Benz and Asphaug (1999). The red a green lines represent two scaling laws assumed for rubble-pile bodies (1. with less strength than monoliths at all sizes; 2. with less strength than monoliths at large sizes). Their derivations are described in Section 7. (For interpretation of the references to colour in this figure legend, the reader is referred to the web version of this article.)

We are aware that the observed N_{fam} values do not follow a Poissonian distribution, and that was actually a motivation for us to use a higher value of weighting for families $w_{fam} = 10$ (we multiply χ^2_{fam} by w_{fam}), i.e. we effectively decreased the uncertainty of N_{fam} in the χ^2 sum. The weighting also emphasizes families, because six values of χ^2_{fam} would have only small influence on the total χ^2. Unfortunately, there are still not enough and easily comparable family identifications. Even though there are a number of papers (Parker et al., 2008; Nesvorný, 2012; Masiero et al., 2013; Carruba et al., 2013; Milani et al., 2013), they usually do not discuss parent-body sizes of families.

If a collision between asteroids is not energetic enough (i.e. a cratering event), then only a little of the mass of the target (parent body) is dispersed to the space. In this case, the largest remaining body is called the *largest remnant*. The second largest body, which has a much lower mass, is called the *largest fragment*. If a collision is catastrophic, the first two fragments have comparable masses and in such a case, the largest body is called the *largest fragment*.

In our simulations, we focused on asteroid families with the diameter of the parent body $D_{PB} \geq 100$ km and the ratio of the largest remnant/fragment to the parent body $M_{LF}/M_{PB} < 0.5$ only (i.e. catastrophic disruptions), though the Boulder code treats also cratering events, of course. For that sample we can be quite sure that the observed sample is complete and not biased. This approach is also consistent with the work of Bottke et al. (2005). The numbers of observed families N_{fam} in individual parts are taken from Brož et al. (2013), except for the inner belt, where two additional families were found by Walsh et al. (2013) (i.e. three families in total, see Table 3). Our synthetic families then simply correspond to individual collisions between targets and projectiles — which are energetic enough to catastrophically disrupt the target of given minimum size ($D \geq 100$ km) — as computed by the Boulder code.

In order to avoid complicated computations of the observational bias we simply limit a range of the diameters D_{max} to D_{min} where χ^2 is computed (see Table 4) and we admit a possibility that χ^2 is slightly increased for D approaching D_{min}. We estimated D_{max} and D_{min} for each population separately from the observed SFDs shown in Fig. 2.

5.3. The Boulder code

A collisional evolution of the size–frequency distributions is modeled with the statistical code called Boulder (Morbidelli

Table 2
Parameters of the scaling law according to Benz and Asphaug (1999) (see Eq. (2)). Parameters q_{fact}, Q_0 and B are the normalization parameters, a and b characterize the slope of the corresponding power law. The procedure how we obtained the parameters for rubble-pile bodies is described in Section 7.

	ρ (g/cm³)	Q_0 (erg/g)	a	B (erg/g)	b	q_{fact}
Basalt	3.0	9×10^7	−0.36	0.5	1.36	1.0
Rubble-pile 1	1.84	9×10^7	−0.36	0.5	1.36	13.2
Rubble-pile 2	1.84	118.8×10^7	−0.36	0.5	1.36	13.2

Table 3
The list of asteroid families in individual parts of the main belt according to Brož et al. (2013) and Walsh et al. (2013). Only families with the diameter of the parent body $D_{PB} > 100$ km and the ratio of the largest remnant/fragment to the parent body $M_{LF}/M_{PB} < 0.5$ are listed.

Belt	N_{fam}	Families		
Inner	3	Erigone	Eulalia	Polana
Middle	8	Maria	Padua	Misa
		Dora	Merxia	Teutonia
		Gefion	Hoffmeister	
Pristine	2	Koronis	Fringilla	
Outer	6	Themis	Meliboea	Eos
		Ursula	Veritas	Lixiaohua
Cybele	0			
High Inc.	1	Alauda		

et al., 2009), originally developed for studies of the formation of planetary embryos. Our simulations were always running from 0 to 4 Gyr. The Boulder code operates with particles separated to populations, which can differ in values of the intrinsic impact probability p_i, mutual velocity v_{imp}, in material characteristics, etc. The populations are then characterized by their distribution of mass. The total mass range is divided to logarithmic bins, whose width and center evolve dynamically. The processes which are realized in every time step are:

1. the total numbers of collisions among all populations and all mass bins are calculated according to the mutual p_i's;
2. the mass of the largest remnant M_{LR} and the largest fragment M_{LF} and the slope q of the SFD of fragments are determined for each collision;
3. the largest remnant and all fragments are distributed to the mass bins of the respective population;
4. it is also possible to prescribe a statistical decay of the populations by dynamical processes;
5. finally, the mass bins are redefined in order to have an optimal resolution and an appropriate next time step Δt is chosen.

The relations for M_{LR}, M_{LF} and q, derived from the works of Benz and Asphaug (1999) and Durda et al. (2007), are

$$M_{LR} = \left[-\frac{1}{2}\left(\frac{Q}{Q_D^\star} - 1\right) + \frac{1}{2}\right] M_{tot} \quad \text{for } Q < Q_D^\star, \tag{4}$$

$$M_{LR} = \left[-0.35\left(\frac{Q}{Q_D^\star} - 1\right) + \frac{1}{2}\right] M_{tot} \quad \text{for } Q > Q_D^\star, \tag{5}$$

$$M_{LF} = 8 \times 10^{-3} \left[\frac{Q}{Q_D^\star} \exp\left(-\left(\frac{Q}{4Q_D^\star}\right)^2\right)\right] M_{tot}, \tag{6}$$

$$q = -10 + 7\left(\frac{Q}{Q_D^\star}\right)^{0.4} \exp\left(-\frac{Q}{7Q_D^\star}\right), \tag{7}$$

where M_{tot} denotes the sum of the masses of target and of projectile, $Q_D^\star$ the strength of the asteroid and Q the specific kinetic energy of the projectile

$$Q = \frac{\frac{1}{2} M_{\text{projectile}} v_{\text{imp}}^2}{M_{\text{tot}}}. \tag{8}$$

The disruptions of large bodies have only a small probability during one time step Δt. In such situations the Boulder uses a pseudo-random-number generator. The processes thus become stochastic and for the same set of initial conditions we may obtain different results, depending on the value of the random seed (Press et al., 1992).

The Boulder code also includes additional "invisible" bins of the SFD (containing the smallest bodies) which should somewhat prevent artificial "waves" on the SFDs, which could be otherwise created by choosing a fixed minimum size.

6. Simulations for monolithic objects

We can expect a different evolution of individual populations as a consequence of their different SFDs, collision probabilities and impact velocities. Therefore, in this section we are going to run simulations with a new collisional model with six populations.

6.1. An analysis of an extended parameter space

First, we explored the parameter space on larger scales and started the simplex[10] with many different initial conditions (see Fig. 5). The calculation had 36 free parameters, as explained above. To reduce the total computational time, we change the same parameter in each part of the main belt with every initialisation of the simplex. For example, we increase all parameters q_{a1}, q_{a2}, q_{a3}, q_{a4}, q_{a5}, q_{a6} together and then we search for a neighboring local minimum with the simplex which has all 36 parameters free — we call this one cycle. In total, we run $3^6 = 729$ cycles (i.e. initialisations of the simplex), for each parameter we examined 3 values (within the ranges from Table 4). The maximum permitted number of iterations of the simplex was 300 in one cycle (and we verified that this is sufficient to find a χ^2 value which is already close to a local minimum). In total, we run 218,700 simulations of the collisional evolution of the main belt.

The argument which would (partly) justify simultaneous changes of all parameters in the 6 parts of the main belt is that we use the same scaling law for each of them, therefore we can expect a similar behavior in individual belts and it then seems logical to choose initial conditions (SFDs) simultaneously.

The input parameters are summarized in Table 4. The mid-in-the-range values were derived "manually" after several preliminary simulations of collisional evolution (without simplex or χ^2 calculations). The changes of parameters between cycles and the steps of simplex within one cycle are listed in Table 5.

The minimum value of χ^2, which we obtained, is $\chi^2 = 562$, but we found many other values, that are statistically equivalent (see Fig. 6 as an example). Therefore, we did not find a statistically significant global minimum. The parameters q_{b1-b6} seem to be well-determined within the parameter space, parameters q_{a1-a6}, $d_{1\,1-6}$, $d_{2\,1-6}$ and $n_{\text{norm}\,1-6}$ are slightly less constrained. For the remaining parameters q_{c1-c6} we essentially cannot determine the best values. This is caused by the fact that the 'tail' of the SFD is created easily during disruptions of larger asteroids, so that the initial conditions essentially do not matter. The influence of the initial conditions at the smallest sizes ($D < d_2$) on the final SFDs was carefully checked. As one can see e.g. from the dependence $\chi^2(q_{c1})$, i.e. the resulting χ^2 values as a function of the initial slope of the tail, the outcome is essentially not dependent on the tail slope, but rather on other free parameters of our model.

---

[10] The simplex as well as χ^2 calculation is not a direct part of the Boulder code.

The differences between simulated and observed SFDs and numbers of families for individual populations corresponding to $\chi^2 = 562$ are shown in Figs. 7 and 8. We can see that the largest differences are for the inner and outer belt. Note that it is *not* easy to improve these results, e.g. by increasing the normalization $n_{\text{norm}4}$ of the outer belt, because this would affect all of the remaining populations too.

From Fig. 7, we can also assess the influence of the choice of D_{min} and D_{max} values on the resulting χ^2 — for example, an increase of D_{min} would mean that the χ^2 will be lower (because we would drop several points of comparison this way). However, as this happens in all main belt parts (simultaneously), it cannot change our results significantly. We ran one complete set of simulations with $D_{\text{min}} = 15$ km (i.e. with q_c unconstrained) to confirm it and we found out that the resulting SFDs, at both larger and smaller sizes than D_{min}, are not significantly different from the previous ones.

The parameters of the initial SFDs for the minimal χ^2 are summarized in Table 6. Comparing with Table 4, the best initial slopes q_{a1-6} and q_{c1-6} are both significantly steeper than the mid-in-the-range values (from Table 4) and they exceed the value -3.5 derived by Dohnanyi. We can also see that the SFD of the Cybele zone is significantly flatter than the SFDs of the other populations and is more affected by observational biases (incompleteness) which actually corresponds to our choice of (relatively large) $D_{\text{min}} = 6$ km.

Another approach to the initial conditions we tested is the following: we generated a completely *random* set of 729 initial conditions — generated within the ranges simulated previously — and without simultaneous (i.e. with uncorrelated) changes in the 6 parts of the main belt. We then started the simplex algorithms again, i.e. we computed 729 initial conditions for the simplex $\times 300$ iterations = 218,700 collisional models in total. Results are very similar to the previous ones, with the best $\chi^2 = 544$, which is statistically equivalent to 562, reported above. In Fig. 6, we compare the dependence of the χ^2 on the parameter q_{b2} for simultaneous (correlated) changes of parameters and for the randomized (uncorrelated) sets of initial parameters. Both results are equivalent in terms of residuals and we can conclude that there is no significantly better local minimum on the interval of parameters we studied.

To test the influence of the choice of w_{fam}, we ran simulation with $w_{\text{fam}} = 0$. The resulting SFDs for monoliths were similar (i.e. exhibiting the same problems) and $\chi^2_{\text{sfd}} = 612$ (among $\approx 100,000$ simulations) remained high. We thus think that the choice of w_{fam} is not critical. While this seems like the families do not determine the result at all, we treat this as an indication that the numbers of families and SFDs are consistent.

6.2. A detailed analysis of the parameters space

We also tried to explore the parameter space in detail — with smaller changes of input parameters between cycles and also smaller steps of the simplex. The best χ^2 which we found is however statistically equivalent to the previous value and we did not obtain a significant improvement of the SFDs. Parameters are not well-constrained in this limited parameter space, because the simulations were performed in a surroundings of a local minimum and the simplex was mostly contracting. An even more-detailed exploration of the parameter space thus would not lead to any improvement and we decided to proceed with a model for rubble-pile asteroids.

7. Simulations for rubble-pile objects

The material characteristics of asteroids can significantly influence their mutual collisions. We can modify the Boulder code for
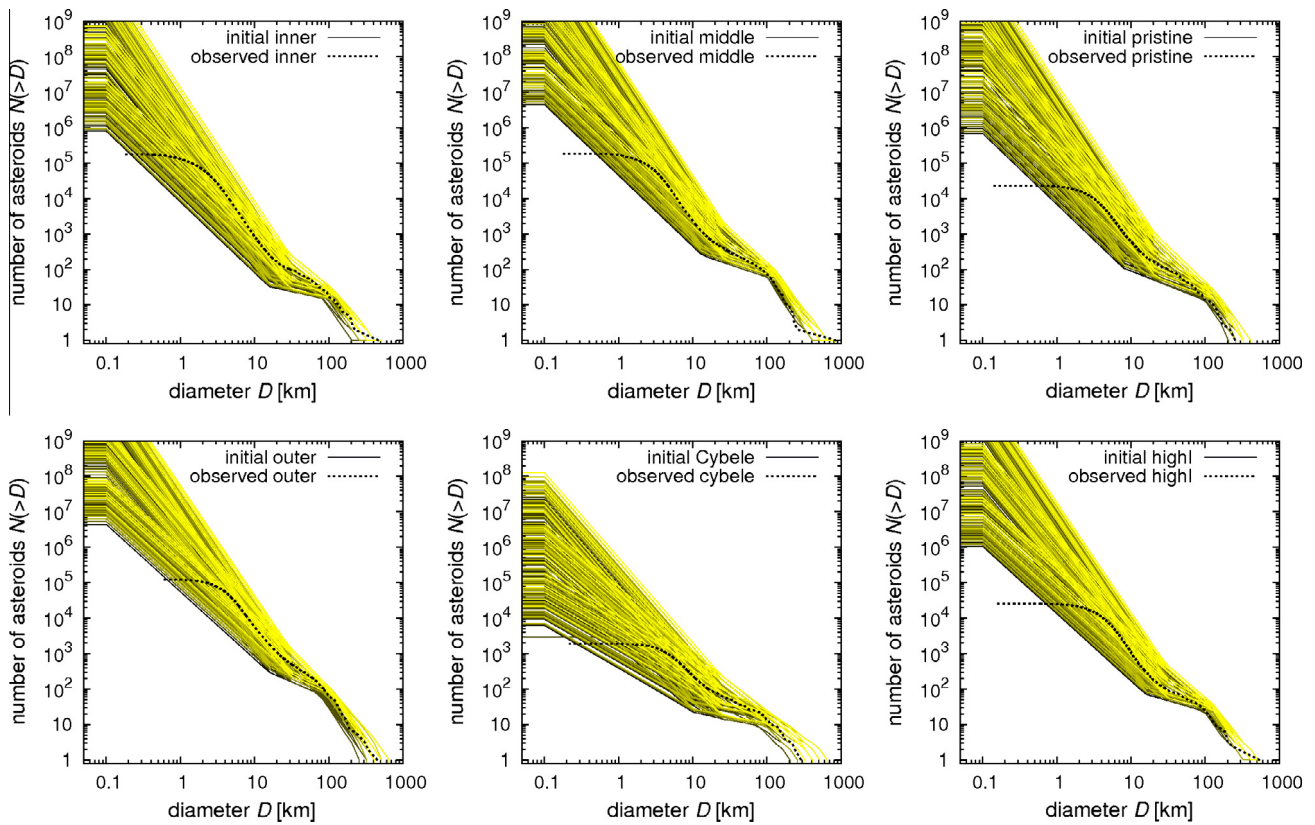
Fig. 5. A set of 729 synthetic size–frequency distributions (for six parts of the main belt), which served as starting points for the simplex algorithm and subsequent simulations of collisional evolution. Thin lines (with various colors) denote the synthetic SFDs, while the thick lines corresponds to the observed SFDs. Note that we tested quite a large range of possible initial conditions. The number of simplex steps was limited to 300 because the convergence to a local minimum is difficult due to the stochasticity of the collisional evolution. The total number of collisional simulations we ran was thus $729 \times 300 = 218,700$. (For interpretation of the references to colour in this figure legend, the reader is referred to the web version of this article.)

Table 4
The ranges of input parameters describing the size–frequency distributions (SFDs) of the six parts of the main belt: q_a denotes the slope of the SFD for asteroids with diameters $D > d_1$, q_b the slope between d_1 and d_2, q_c the slope for $D < d_2$ and n_{norm} is the normalization of the SFD at d_1. N_{fam} denotes the number of observed families and D_{max} and D_{min} the range of diameters in the SFD, where the χ^2 is calculated.

Population	d_1 (km)	d_2 (km)	q_a	q_b	q_c	n_{norm}	N_{fam}	D_{max} (km)	D_{min} (km)
Inner	75 to 105	14 to 26	−3.6 to −4.2	−1.5 to −2.7	−3.0 to −4.2	14 to 26	3	250	3
Middle	90 to 120	12 to 24	−4.0 to −4.6	−1.7 to −2.9	−3.0 to −4.2	60 to 90	8	250	3
Pristine	85 to 115	7 to 19	−3.3 to −3.9	−1.8 to −3.0	−3.0 to −4.2	15 to 27	2	250	5
Outer	65 to 95	14 to 26	−3.4 to −4.0	−1.9 to −3.1	−2.9 to −4.1	75 to 105	6	250	5
Cybele	65 to 95	9 to 21	−2.2 to −2.8	−1.4 to −2.6	−2.2 to −3.4	11 to 23	0	250	6
High-inclination	85 to 115	14 to 26	−3.6 to −4.2	−1.6 to −2.8	−2.9 to −4.1	24 to 36	1	250	5

rubble-pile bodies on the basis of Benavidez et al. (2012) work, who ran a set of SPH simulation for rubble-pile $D_{PB} = 100$ km parent bodies. We used data from their Fig. 8, namely diameters of fragments inferred for simulations with various projectile diameters and impact velocities.

7.1. Modifications of the Boulder code for rubble-pile bodies

We need to modify the parameters of the scaling law first. We were partly inspired by the shape of scaling laws presented in Levison et al. (2009) for icy bodies (Fig. 3 therein). The modified versions used by these authors are all scaled-down by a factor (i.e. q_{fact} in our notation). Thus, the only two parameters we changed are q_{fact} and density. For the density of asteroids, we used $\rho = 1.84$ g cm^{-3} as Benavidez et al. (2012). We determined the specific impact energy Q_D^* required to disperse half of the total mass of a $D = 100$ km rubble-pile target from the dependence of the mass of the largest remnant M_{LR} as a function of the kinetic

Table 5
The changes of input parameters between cycles, and steps of the simplex within one cycle. d_1, d_2, q_a, q_b, q_c and n_{norm} denote the same parameters as in Table 4. For the middle and outer belt, which are more populous, we used $\Delta n_{norm} = 15$ and $\delta n_{norm} = 5$.

	d_1 (km)	d_2 (km)	q_a	q_b	q_c	n_{norm}
Cycles	±15	±6	±0.3	±0.6	±0.6	±6; 15
Steps	5	2	0.1	0.2	0.2	2; 5

energy of projectile Q (see Fig. 9). Q_D^* is then equal to Q corresponding to $M_{LR}/M_{target} = 0.5$. So the result is $Q_D^* = (9 \pm 1) \times 10^7$ erg g^{-1} and the corresponding parameter q_{fact} in the scaling law is then 13.2 ± 1.5 (calculated according to Eq. (2) with $\rho = 1.84$ g cm^{-3}, $r = 5 \times 10^6$ cm, parameters Q_0, a, B and b remain same as for the monolithic bodies). The scaling law for rubble-pile bodies was already shown graphically in Fig. 4 (red line).

We must also derive new dependencies of the slope $q(Q)$ of the fragments' SFD and for the mass of the largest fragment $M_{LF}(Q)$ on

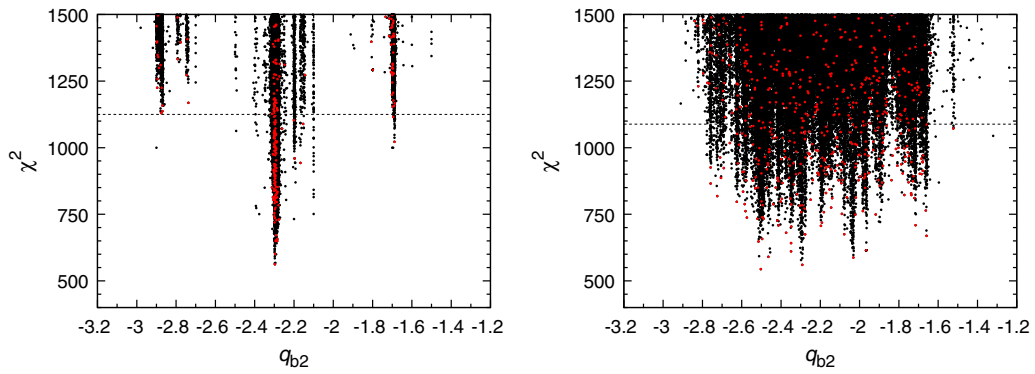**Fig. 6.** The values of χ^2 for all simulations of collisional evolution as a function of the parameter q_{b2} (i.e. the slope of the SFD of the middle belt for asteroids with diameters $D < d_1$ and $D > d_2$). Black points display all initial conditions of the collisional models (within the ranges of the figure), red points display the initial conditions for which simplex converged to a local minimum (i.e. 729 points in total, but less within the ranges of the figure). The dotted line is a value twice larger than the best χ^2. Values below this line we consider statistically equivalent. Left: simultaneous (correlated) changes of parameters in individual parts of the main belt. Right: randomized (uncorrelated) set of initial parameters (as described in the text). (For interpretation of the references to colour in this figure legend, the reader is referred to the web version of this article.)

the specific energy Q of the impact. The cumulative SFDs of the fragments cannot be always described with only one single slope. We thus divided the fragments according to their diameters to small ($D < 10$ km) and large ($D > 10$ km) and we determined two slopes. Then we calculated the mean value and we used the differences between the two values as error bars (see Fig. 10).

For some of the SPH simulations outcomes it can be difficult to determine the largest fragment, in other words, to distinguish a catastrophic disruption from a cratering event, as explained in Section 5.2. The error bars in Fig. 11 correspond to the points, which we would get if we choose the other of the two above-mentioned possibilities.
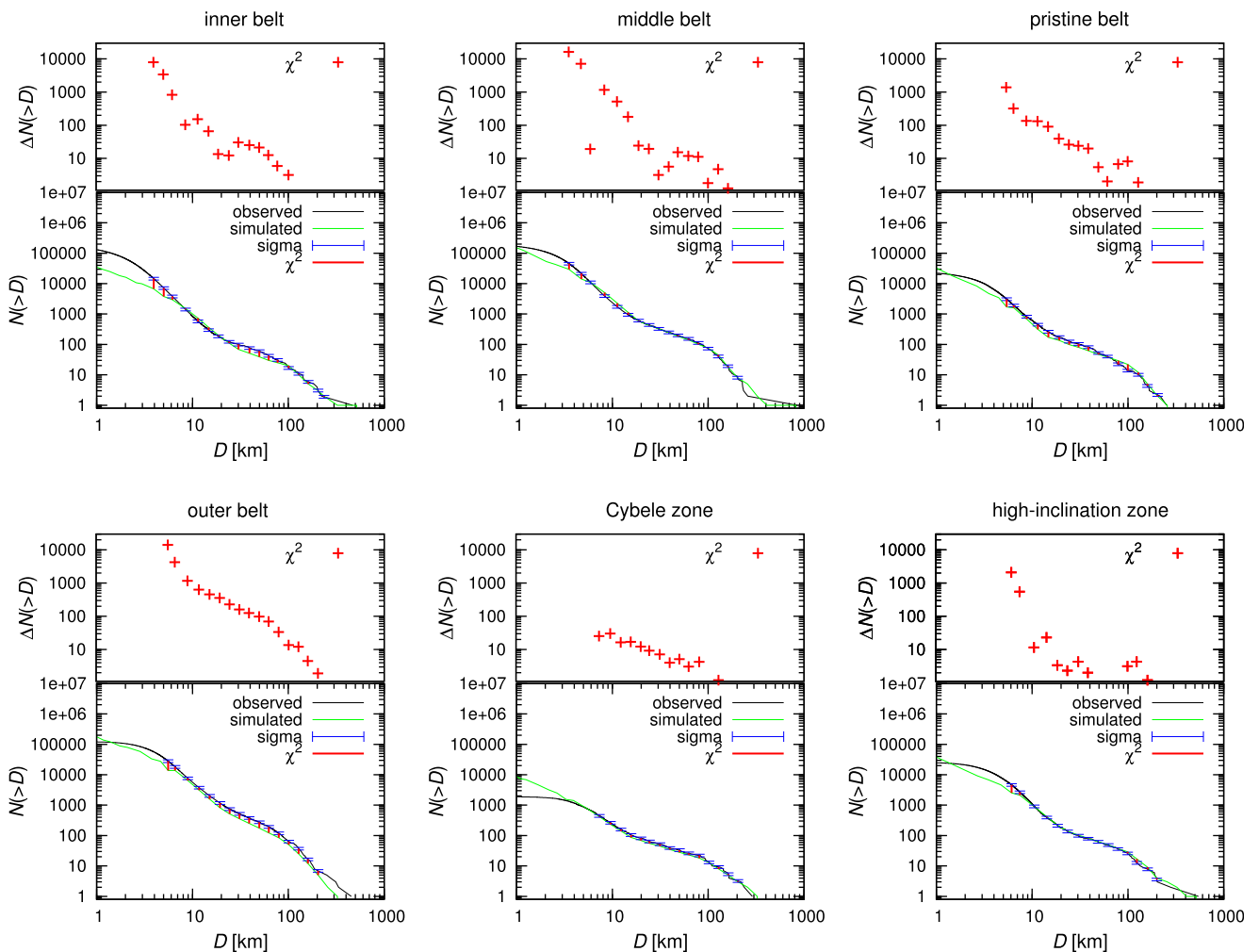

Fig. 7. The observed (black line) and simulated (green line) SFDs and the differences between them for the simulation with $\chi^2 = 562$. Sigma error bars denote the (prescribed) uncertainties of the observed SFDs. This result is for the simulation with monoliths. The largest differences can be seen for the inner and outer belt. (For interpretation of the references to colour in this figure legend, the reader is referred to the web version of this article.)
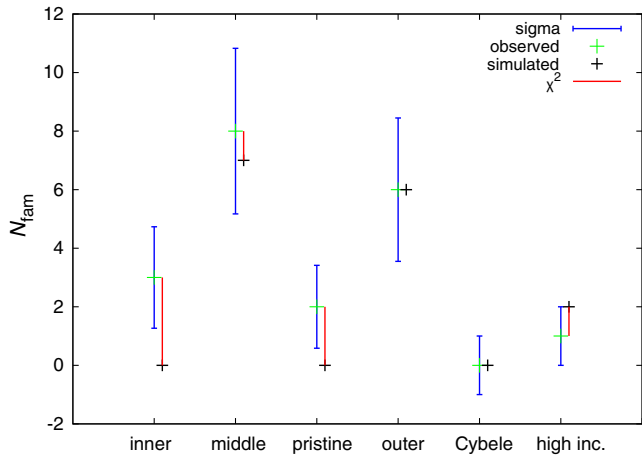
Fig. 8. The differences between simulated and observed numbers of families N_{fam} in individual populations, corresponding to the total $\chi^2 = 562$. Sigma error bars denote the uncertainties of the observed numbers of families. This results is for simulations with monoliths. The simulated and observed numbers of families seem to be consistent within the uncertainties.

The parametric relations we determined for rubble-pile bodies are the following

$$q = -6.3 + 3.16\left(\frac{Q}{Q_D^\star}\right)^{0.01} \exp\left(-0.008\frac{Q}{Q_D^\star}\right), \quad (9)$$

$$M_{\text{LF}} = \frac{0.6}{13\left(\frac{Q}{Q_D^\star}\right)^{-1.2} + 1.5\frac{Q}{Q_D^\star}} M_{\text{tot}}. \quad (10)$$

When we approximate scattered data with functions, we must carefully check their limits. In the case of low-energetic collisions there is one largest remnant and other fragments are much smaller, therefore for decreasing Q we need M_{LF} to approach zero. The slope q we need to stay negative and not increasing above 0 (that would signify an unphysical power law and zero number of fragments). These conditions are the reasons why our functions do not go through all of the data points (not even within the range of uncertainties). This problem is most pronounced for the dependence of $M_{\text{LF}}(Q)$ for small Q (Fig. 11). Nevertheless, we think that it is more important that the functions fit reasonably the data for high Q's, because highly-energetic collisions produce a lot of fragments and they influence the SFD much more significantly.

7.2. A comparison of results for monoliths and rubble-piles with less strength at all sizes

We explored the parameter space in a similar way as for monoliths: with 729 different initial SFDs (i.e. 729 cycles), the maximum permitted number of iterations 300 and 218,700 simulations in total. The changes of parameters between cycles and the steps of

Table 6
The parameters describing the initial SFDs (for time $t = -4$ Gyr) of the six parts of the main belt for which we obtained the best fit ($\chi^2 = 562$) of the observed SFDs and the number of families. d_1, d_2, q_a, q_b, q_c and n_{norm} denote the same parameters as in Table 4 and are rounded to two decimal places.

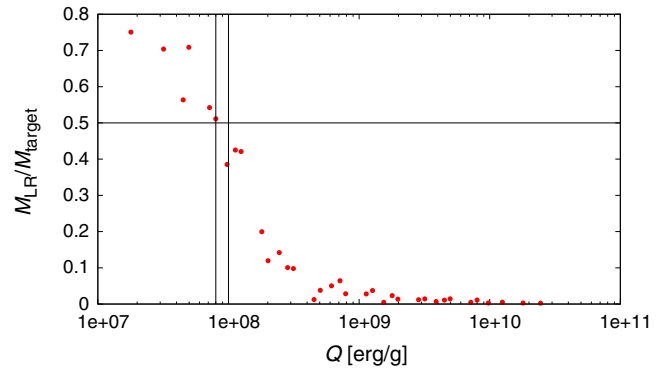| Population	d_1 (km)	d_2 (km)	q_a	q_b	q_c	n_{norm}
Inner	90.07	20.03	−4.20	−2.10	−4.20	20.03
Middle	105.07	18.03	−4.60	−2.30	−4.20	75.07
Pristine	100.07	13.03	−3.90	−2.30	−4.20	21.03
Outer	80.07	20.03	−4.00	−2.50	−4.10	90.07
Cybele	80.07	15.03	−2.80	−2.00	−3.40	17.03
High-inclination	100.07	20.03	−4.20	−2.20	−4.10	30.03

Fig. 9. The dependence of the mass of the largest remnant M_{LR} on the kinetic energy Q of the projectile for rubble-pile bodies. We mark the value $M_{\text{LR}}/M_{\text{target}} = 0.5$ with a horizontal line, according to this value we determine $Q_D^\star$. The uncertainties of the determination of $Q_D^\star$ are denoted by vertical lines. The result is $Q_D^\star = (9 \pm 1) \times 10^7$ erg g^{-1}.
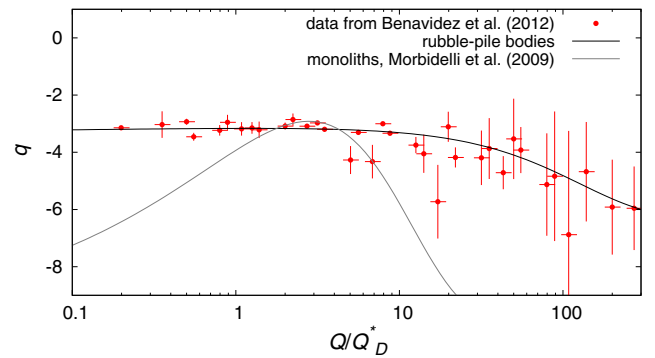

Fig. 10. The slope q of the SFD of fragments as a function of the impact energy $Q/Q_D^\star$ for the rubble-pile parent bodies with $D_{\text{PB}} = 100$ km. The horizontal axis is in a logarithmic scale. The SFD of fragments is characterized by two slopes (for fragments $D < 10$ km and $D > 10$ km) and we calculated the mean value. The displayed uncertainties of q are the differences between real and mean values. The horizontal error bars are given by the uncertainties of $Q_D^\star$. The gray line corresponds to the dependence for monoliths (Morbidelli et al., 2009), which we used in Section 6.
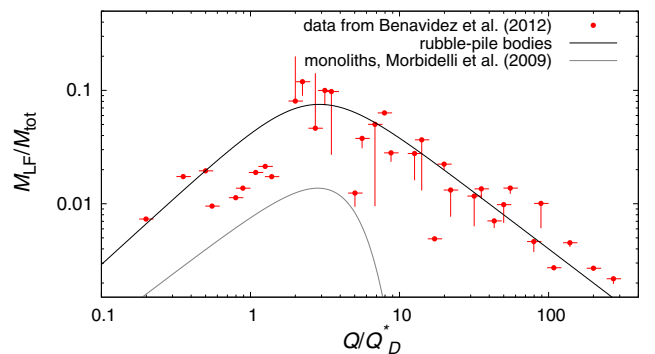

Fig. 11. The ratio $M_{\text{LF}}/M_{\text{tot}}$ (the mass of the largest fragment divided by the sum of the mass of target and the mass of projectile) as a function of the impact energy $Q/Q_D^\star$ for the rubble-pile parent bodies with the diameter $D_{\text{PB}} = 100$ km. The horizontal axis is in a logarithmic scale. The uncertainties of $M_{\text{LF}}/M_{\text{tot}}$ are caused by a problematic determination of the largest fragment and the largest remnant. The horizontal error bars are given by the uncertainties of $Q_D^\star$. The gray line corresponds to the dependence for monoliths (Morbidelli et al., 2009) which we used in Section 6.

the simplex within one cycle are the same as for simulations with monolithic bodies (see Table 5).

The minimum χ^2 which we obtained was 1321. The differences between the simulated and observed SFDs and the numbers of families for individual populations corresponding to $\chi^2 = 1321$ are shown in Figs. 12 and 13. These values are significantly higher than what we obtained for monoliths ($\chi^2 = 562$ at best). Given that the set of initial conditions was quite extensive (refer to Fig. 5), we think that this difference is fundamental and constitutes a major result of our investigation.

It seems that, at least within our collisional model, we can pre-liminarily conclude that the main belt does not contain *only* rub-ble-pile bodies, because otherwise the corresponding fit would not be that worse than for monoliths (see Figs. 7 and 8 for a comparison).

It would be interesting to run a simulation with two different population of the main belt − monolithic and rubble-pile bodies. Also because Benavidez et al. (2012) concluded that some asteroid families were more likely created by a disruption of a rubble-pile parent body: namely the Meliboea, Erigone, Misa, Agnia, Gefion and Rafita. Such simulation remains to be done.

7.3. Simulations for rubble-piles with less strength at large sizes

Large rubble-piles objects can be also assumed to be composed of monolithic blocks with sizes of the order of 100 m. Then, at and below this size, the scaling law $Q_D^\star$ should be a duplicate of the Benz and Asphaug (1999) − see Fig. 4 (green line). We computed a new set of $729 \times 300 = 218{,}700$ collisional simulations with the scaling law modified in this way. The resulting smallest χ^2 is 1393, which should be compared to the previous result $\chi^2 = 1321$ − i.e. no statistically significant improvement.

We thus can conclude that this kind of $Q_D^\star$ modification does not lead to an improvement of the model. We think that the collisional evolution and overall shape of the SFDs are more affected by dis-ruptions of large asteroids.

8. Improvements and extensions of the model

We think that the match between our collisional model and the observational data as presented in Sections 6 and 7 is not entirely convincing. In this section we thus try to improve the model by the following procedures: (i) we use a longer 'tail' of the SFD (down to $D = 0.01$ km), which is a straightforward modification. Neverthe-less, the longer tail means a significant increase of the required CPU time (which is proportional to N_{bins}^2). (ii) We account for the Yarkovsky effect whose time scales for small bodies ($D \lesssim 0.1$ km) are already comparable to the collisional time scales (see Section 8.1). (iii) We do not converge all 36 free parameters at once but we free only 6 of them (d_1, d_2, q_a, q_b, q_c and n_{norm} for one popu-
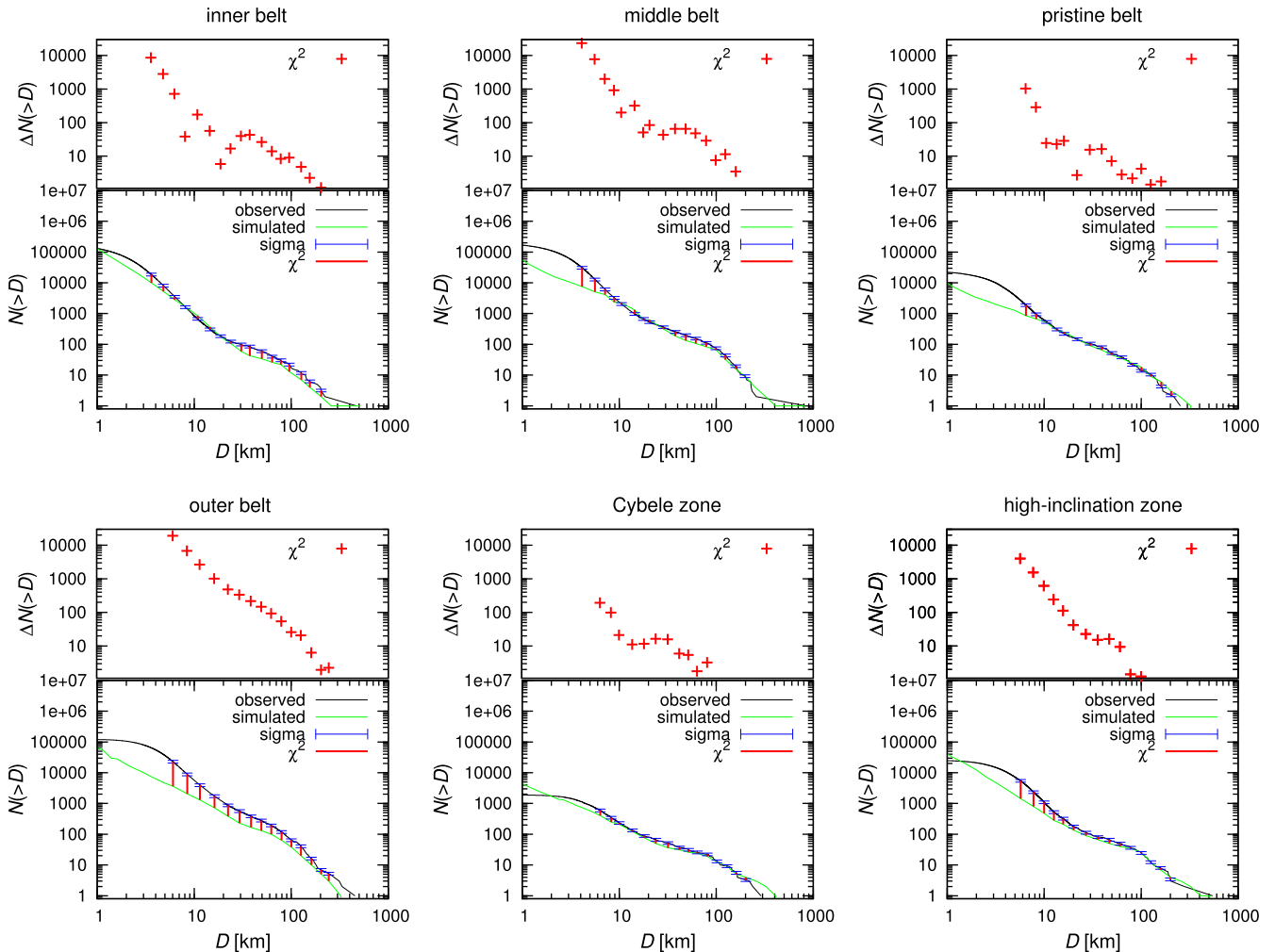

Fig. 12. The observed (black line) and simulated (green line) SFDs and the differences between them for the simulation with rubble-piles with total $\chi^2 = 1321$. Sigma error bars denote the adopted uncertainties of the observed SFDs. (For interpretation of the references to colour in this figure legend, the reader is referred to the web version of this article.)
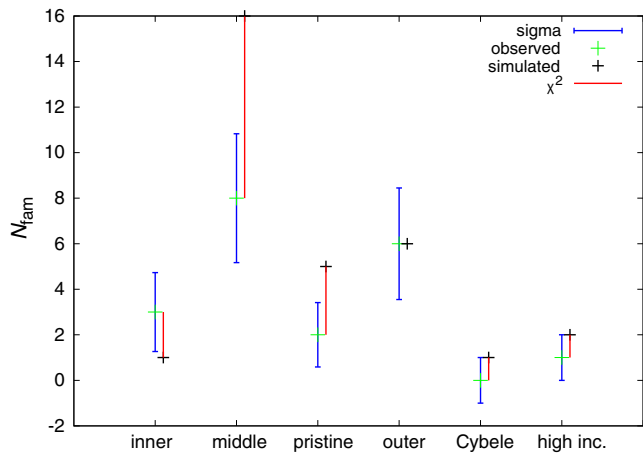
Fig. 13. The simulated and the observed numbers of families N_{fam} in individual populations for the simulation with rubble-piles, corresponding to the total $\chi^2 = 1321$. Sigma error bars denote the uncertainties of the observed numbers of families.

lation only) and proceed sequentially with six parts of the main belt (see Section 8.2). (iv) Finally, we try to use a scaling law different from Benz and Asphaug (1999) (see Section 8.3).

8.1. Dynamical decay caused by the Yarkovsky effect

In order to improve the Boulder code and use a more complete dynamical model, we try to account for the Yarkovsky effect as follows. We assume that the Yarkovsky effect causes a dynamical decay of the population which can be described by the following relation

$$N(t + \Delta t) = N(t) \exp\left(\frac{\Delta t}{\tau_{YE}}\right), \qquad (11)$$

where $N(t)$ denotes the number of bodies at time t, Δt the time step of the integrator and τ_{YE} is the characteristic timescale.

We can compute the semimajor-axis drift rate da/dt, for both the diurnal and seasonal variants of the Yarkovsky effect, using the theory of Vokrouhlický (1998), Vokrouhlický and Farinella (1999) and the (size-dependent) time scale is then

$$\tau_{YE}(D) = \frac{\Delta a}{d} a/dt(D), \qquad (12)$$

where Δa is the range of semimajor axis given by the positions of major mean-motion resonances which are capable to remove objects from the respective populations. It differs for different zones of the main belt, of course (see Table 7).

In the thermal model, we assume the following parameters: the thermal conductivity $K = 0.01$ W m^{-1} K^{-1} for $D > D_{YE}$, i.e. a transition diameter, and 1.0 W m^{-1} K^{-1} for $D \leqslant D_{YE}$. The break in $K(D)$ reflects the rotational properties of small bodies, as seen in Fig. 14 (and Warner et al., 2009): they rotate too fast, above the critical limit of about 11 revolutions/day, to retain low-conductivity regolith on their surfaces. This is also in accord with infrared observations of Delbo' et al. (2007), even though the authors propose a linear relationship between the thermal intertia $\Gamma = \sqrt{K\rho C}$ and size D (their Fig. 6), a step-like function may be also compatible with the data. The thermal capacity was $C = 680$ J kg^{-1} K^{-1}, the infrared emissivity $\epsilon = 0.95$ and the Bond albedo $A_B = 0.02$. The latter value of A_B corresponds to the geometric albedo $p_V = 0.05$, which is typical for C-complex asteroids (e.g. Masiero et al., 2013), with $A_B = p_V q$, where q denotes the phase integral (with a typical value of 0.39; Bowell et al., 1989). If we

assume higher $p_V = 0.15$ (typical of S-complex) and $A_B = 0.06$, the Yarkovsky dynamical time scale would remain almost the same, because it is driven by the factor $(1 - A_B)$. Remaining thermal parameters, namely the densities, are summarized in Table 7.

Table 7
The parameters of the Yarkovsky-driven decay which are dependent on the zone of the main asteroid belt: Δa is half of the zone size (or a typical distance from neighboring strong mean-motion resonances), ρ denotes the (bulk and surface) density assumed for respective bodies.

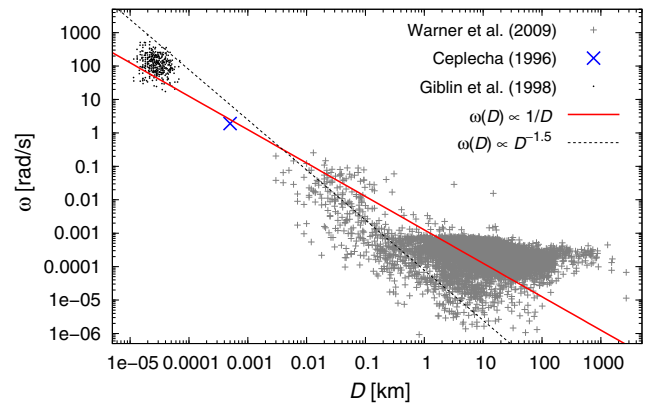| Zone	Δa AU	ρ kg m^{-3}
Inner	0.2	2500
Middle	0.1615	2500
Pristine	0.0665	1300
Outer	0.162	1300
Cybele	0.105	1300
High-I	0.135	1300

Fig. 14. The spin rate ω vs size D dependence for asteroids (observational data from Warner et al. (2009), the Lost City fireball (Ceplecha, 1996) and fragments in laboratory experiments (Giblin et al., 1998). Two approximations are given: $\omega(D) \propto 1/D$, and $\omega(D) \propto D^{-1.5}$, which better fits the observational data in the size range $D \in (0.01, 1)$ km where the Yarkovsky drift is the most important with respect to the collisional model. Nevertheless, we cannot yet exclude a possibility that the observed $\omega(D)$ distribution is still strongly biased for small $D \lesssim 1$ km.

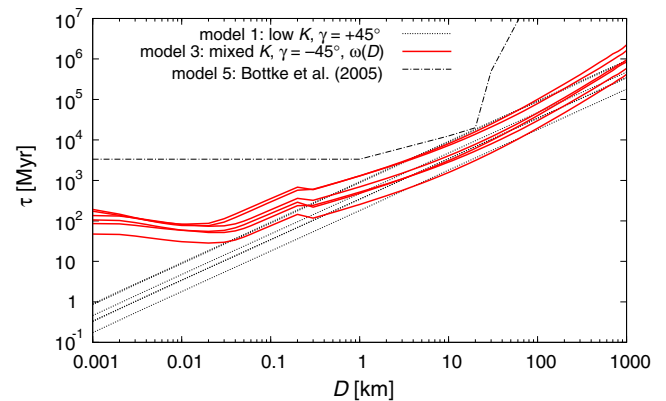**Fig. 15.** The time scale τ_{YE} of the Yarkovsky-driven decay (as defined by Eq. (12)) vs size D for three different models (denoted 1, 3 and 5), or in other words, assumptions of the thermal conductivity $K(D)$ and the spin rate $\omega(D)$, which were described in the text. The obliquities γ of the spin axes were assumed moderate, $|\gamma| = 45°$. Model 2 is quite similar to 1 and model 4 is similar to 3, so we decided not to plot them in order to prevent many overlapping lines. For each model, we plot six lines corresponding to the six zones of the main belt: inner, middle, 'pristine', outer, Cybele and high inclination. Bottke et al. (2005) time scales were used for the whole main belt (regarded as a single population).
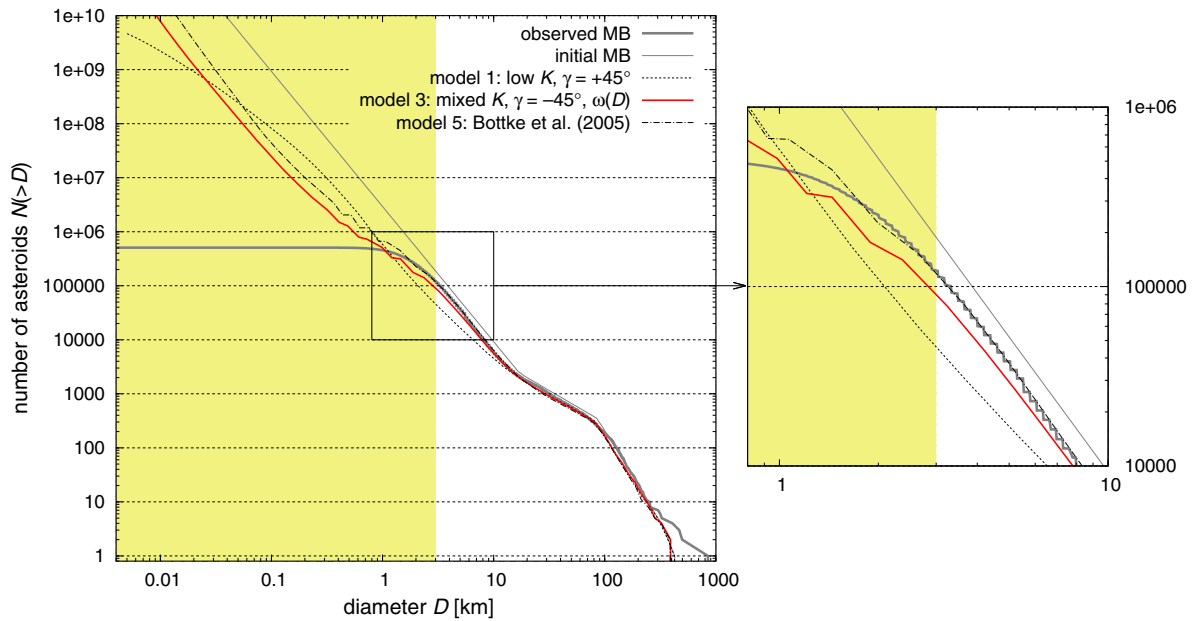
Fig. 16. Resulting synthetic size–frequency distributions of the main belt (regarded as a single population) after 4 Gyr of collisional evolution, as computed by the Boulder code. We show results for three different models of the Yarkovsky-driven decay (denoted 1, 3 and 5 in the text). Model 1 (dotted line) is clearly inconsistent with the observed SFD (thick gray line). The shaded region corresponds to the sizes well below the observational completeness.

We tested five different models (assumptions):

1. low thermal conductivity $K = 0.01\,\mathrm{W\,m^{-1}\,K^{-1}}$ only, i.e. $D_{YE} = 0$ km, fixed rotation period $P = 5$ h;
2. both low/high K with $D_{YE} = 200$ m, again $P = 5$ h;
3. the same $K(D)$ dependence, but size-dependent spin rate $\omega(D) = \frac{2\pi}{P_0}\frac{D_0}{D}$, $P_0 = 5$ h, $D_0 = 5$ km;
4. $\omega(D) = \frac{2\pi}{P_0}\left(\frac{D}{D_0}\right)^{-1.5}$, $P_0 = 2$ h, $D_0 = 0.2$ km (see Fig. 14);
5. we used Bottke et al. (2005) time scales.

It is important to explain that these spin rate dependencies are not meant to describe bigger asteroids but rather smaller ones ($D \lesssim 1$ km) that comprise the majority of impactors but mostly fall below the detection threshold.

We then computed the Yarkovsky time scales $\tau_{YE}(D)$ (Fig. 15) and constructed a 'testing' collisional model in order to check the influence of the dynamical decay on the evolution of the main belt SFD. Note that for small sizes $D \lesssim 1$ km, $\tau_{YE}(D)$ can be even smaller than corresponding collisional time scales $\tau_{col}(D)$.

Regarding the asteroid families, we use the most straightforward approach: we simply count only families large enough (original $D_{PB} > 100$ km, $m_{LR}/m_{PB} < 0.5$) which *cannot* be completely destroyed by a collisional cascade (Bottke et al., 2005) or by the Yarkovsky drift (Bottke et al., 2001). We verified this statement (implicitly) also in our recent work (Brož et al., 2013) in which the evolution of SFDs for individual synthetic families was studied. At the same time, we use *original* parent-body sizes D_{PB} of the observed families − inferred by using methods of Durda et al. (2007) or Tanga et al. (1999); as summarized in Brož et al. (2013) − so that we can directly compare them to synthetic families, as output from the Boulder code.

The results of models 1 and 2 above are clearly not consistent with the observed SFD (see Fig. 16). The results of 3, 4 and 5 seem to be equivalent and consistent with observations, however, we cannot distinguish between them. We can thus exclude 'extreme' Yarkovsky drift rates and conclude that only lower or 'reasonable' drift rates provide a reasonable fit to the observed SFD of the main belt.

8.2. Subsequent fits for individuals parts of the main belt

In order to improve our 'best' fit from Section 6 (and 7), we ran simplex sequentially six times, with only 6 parameters free in each case, namely d_1, d_2, q_a, q_b, q_c, n_{norm} for a given part of the main belt. We included a longer tail ($D_{min} = 0.01$ km) and the Yarkovsky model discussed above.[11] The number of simplex iterations was always limited to 100.

We shall not be surprised if we obtain a χ^2 value which is (slightly) larger than before because we changed the collisional model and this way we moved *away* from the previously-found local minimum. At the same time, we do not perform that many iterations as before (600 vs. 218,700), so we cannot 'pick-up' the deepest local minima.

For monoliths, we tried to improve the 'best' fit with $\chi^2 = 562$. However, the initial value at the very start of the simplex was $\chi^{2\prime} \simeq 803$ (due to the changes in the collisional model) and the final value after the six subsequent fits $\chi^{2\prime\prime} = 520$. This is only slightly smaller than the previous χ^2 and statistically equivalent ($\chi^{2\prime\prime} \simeq \chi^2$). For rubble-piles, a similar procedure for the $\chi^2 = 1321$ fit lead to the initial $\chi^{2\prime} \simeq 1773$ and the final $\chi^{2\prime\prime} = 1470$. Again, a statistically-equivalent result.

We interpret this as follows: our simplex algorithm naturally selects deep local minima. It seems that the lowest χ^2 (for a given set of initial conditions) can be achieved by a 'lucky' sequence of disruptions of relatively large bodies ($D_{PB} \gtrsim 100$ km) which results in synthetic SFDs and the numbers of families best matching the observed properties. Of course, this sequence depends on the 'seed' value of the random-number generator.

To conclude, our improvements of the collisional model do not seem significant and the χ^2 values are of the same order. This can be considered as an indication that we should probably use an even more complicated model. (Nevertheless, there is still a significant

---

[11] This more complicated model runs about 10 times slower, because we have both larger number of bins to account for smaller bodies and a shorter time step to account for their fast dynamical removal. It is thus not easy to run a whole set of simulations from Sections 6 and 7 again.
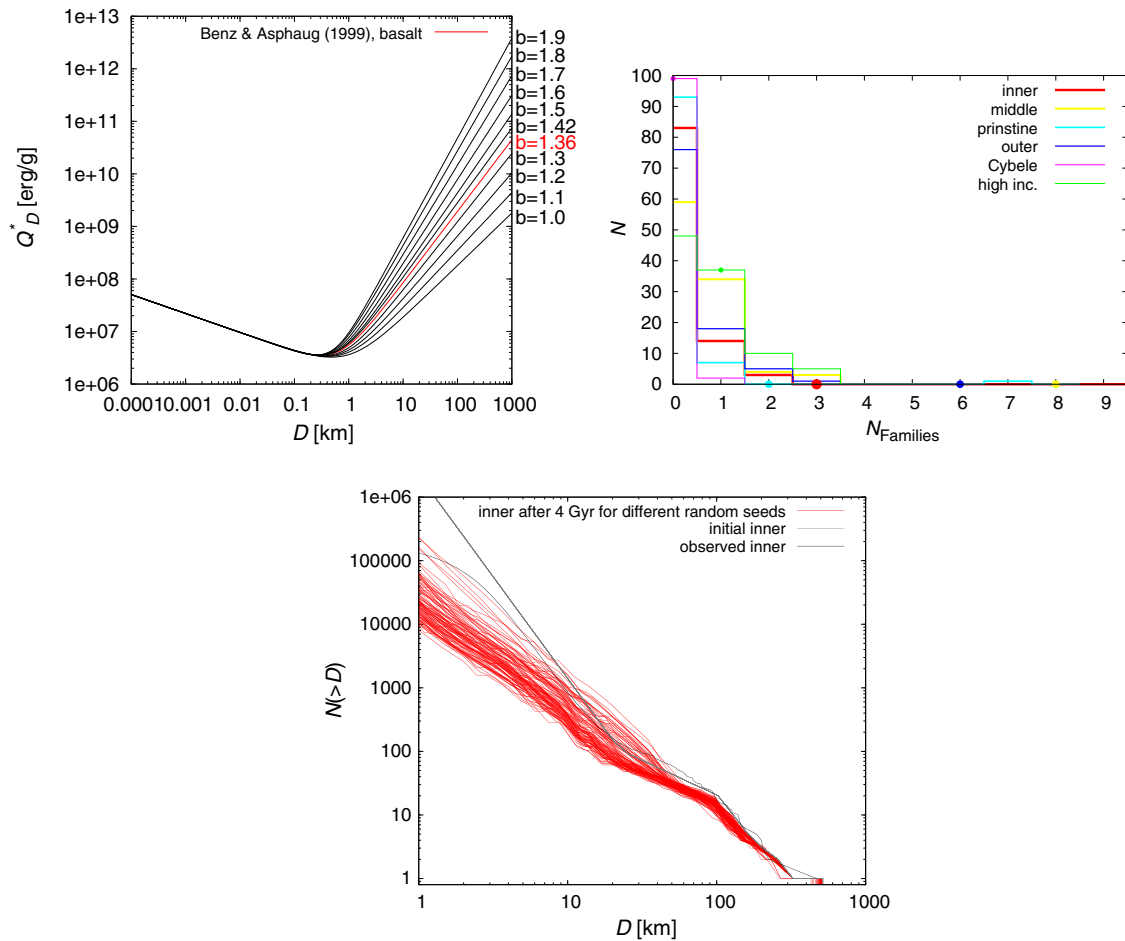
Fig. 17. Left: A number of scaling laws with modified strength of large bodies (a similar set as in Bottke et al. (2005)). The red line represents the nominal scaling law of Benz and Asphaug (1999). Middle: histograms representing the number N of simulations (out of 100) a given number of families $N_{families}$ was created; we assumed the scaling law with an increased strength of large bodies ($b = 1.9$). The observed numbers of families are displayed as filled circles for comparison. Right: the final size–frequency distributions of the inner belt for 100 simulations with different random seeds and for the scaling law with a decreased strength of large bodies ($b = 1.0$). Neither of these two mentioned simulations is consistent with the observations (their χ^2 would be clearly much larger than the best fit from Section 6). (For interpretation of the references to colour in this figure legend, the reader is referred to the web version of this article.)

difference between monoliths and rubble-piles and the assumption of monolithic structure matches the observations better.)

8.3. Simulations with various scaling laws

So far we used the scaling law of Benz and Asphaug (1999) for all simulations. In this section, we are going to test different scaling laws. Similarly as Bottke et al. (2005), we changed the specific impact energy Q_D^* of asteroids with $D > 200$ m (see Fig. 17, left). For each scaling law we ran 100 simulations of the collisional evolution with different random seeds. The initial parameters of SFDs are fixed and correspond to the best-fit initial parameters found in Section 6.

In order to decide which scaling laws are suitable, we can simply compare the resulting synthetic SFDs and the numbers of families to the observed ones. It is clear that if we increase the strength of $D \simeq 100$ km bodies by a factor of 10 or more, the number of synthetic families (namely catastrophic disruptions with $D_{PB} \geqslant 100$ km) is much smaller than the observed number (usually 4 vs 20, see in Fig. 17, middle). On the other hand, if we decrease the strength by a factor of 10, the synthetic SFDs exhibit a significant deficit of small bodies with $D < 10$ km due to a collisional cascade (especially in the inner belt, see Fig. 17, right). Moreover, the number of synthetic families is then significantly larger, of course.

The fact that the number of synthetic families is dependent on the scaling law confirm our statement that families are important observational constraints.

These results lead us to the conclusion, that the 'extreme' scaling laws (i.e. much different from Benz and Asphaug, 1999) cannot be used for the main asteroid belt. This result is also in accord with Bottke et al. (2005).

9. Conclusions

In this work, we created a new collisional model of the evolution of the main asteroid belt. We divided the main belt into six parts and constructed the size–frequency distribution for each part. The observed SFDs differ significantly in terms of slopes and total numbers of asteroids. We then ran two sets of simulations — for monolithic bodies and for rubble-piles.

In the case of monoliths, there seem to be (relatively minor) discrepancies between the simulated and observed SFDs in individual parts of the main belt, nevertheless, the numbers of families (catastrophic disruptions) correspond within uncertainties. On the other hand, the χ^2 value for rubble-pile bodies is more than twice as large because there are systematic differences between the SFDs and the number of families is substantially larger (usually 30 or more) than the observed one (20 in total). We can thus conclude

that within our collisional model, monolithic asteroids provide a better match to the observed data than rubble-piles, even though we cannot exclude a possibility that a certain part of the population is indeed of rubble-pile structure, of course.

We tried to improve our model by: (i) introducing a longer 'tail' of the SFD[12] (down to $D = 0.01$ km); (ii) incorporating the Yarkovsky effect, i.e. a size-dependent dynamical decay; (iii) running many simulations with different random seeds, in order to find even low-probability scenarios. Neither of these improvements provided a substantially better match in *all* parts of the main belt at once.

However, we can think of several other possible reasons, why the match between our collisional model and the observed SFDs is not perfect:

1. There are indeed different scaling laws for different parts of the main belt. This statement could be supported by the observed distribution of albedo, which is not uniform in the main belt, and by the diverse compositions of asteroids (DeMeo and Carry, 2014). This topic is a natural continuation of our work (and a detailed analysis is postponed to a forthcoming paper).
2. The scaling of the SPH simulations from $D_{PB} = 100$ km by one or even two orders of magnitude is likely problematic. Our work is thus a motivation to study disruptions of both smaller ($D_{PB} \simeq 1$ km) and larger (400 km) targets. Similar sets of SPH simulations as in Durda et al. (2007) and Benavidez et al. (2012) would be very useful for further work.
3. To explain the SFD of the inner belt, namely its 'tail', we would need to assume a recent disruption (during the last ~100 Myr) of a large parent body ($D_{PB} \gtrsim 200$ km). In that case the SFD is temporarily steep — and may be closer to the observed SFD in the particular part of the main belt — but only for a limited period of time which is typically about 200 Myr. After that time, the collisional cascade eliminates enough bodies and consequently the SFD becomes flatter. On the other hand, there must not have occurred a recent large disruption in the middle or the outer belt, otherwise the synthetic SFD is more populous than the observed one. It is not likely, that all such conditions are fulfilled together in our model, in which collisions occur randomly.
4. When we split the main belt into 6 parts, the evolution seems too stochastic (the number of large events in individual part is of the order of 1). It may be even useful to prepare a 'deterministic model', in which large disruptions are *prescribed*, according to the observed families and their ages. Of course, the completeness of the family list and negligible bias are then crucial.
5. Our model does not yet include an YORP-induced fission (Marzari et al., 2011), even though there are indications that these 'additional' disruptions might affect the tail of the SFD if they are frequent enough as stated by Jacobson et al. (2014).
6. We can improve the modeling of the Yarkovsky/YORP effect, e.g. by assuming a more realistic distribution of spin rates (not only the $\omega(D)$ dependence, Fig. 14) and performing an N-body simulation of the orbital evolution to get a more accurate estimate of the (exponential) time scale $\tau_{YE}(D)$. It may be difficult to estimate biases in the $\omega(D)$ plot, because the respective dataset is heterogeneous. Luckily, the Gaia spacecraft is expected to provide a large homogeneous database of asteroid spin properties (Mignard et al., 2007).

7. May be, the intrinsic collisional probabilities p_i were substantially different (lower) in the past, e.g. before major asteroid families were created (as suggested by Dell'Oro et al. (2001)).
8. Some of the mutual impact velocities v_{imp}, especially with high-inclination objects, are substantially larger than the nominal 5 km s^{-1}, so the outcomes of these collisions are most-likely different. On the other hand, these collisions are usually of lower probability and the high-inclination region is not that populous, so that this effect has likely a minor contribution only. One should properly account for observational biases acting against discoveries of high-inclination objects, thought (Novaković et al., 2011).
9. Collisions occur not only at the mean impact velocity v_{imp}, but there is rather a distribution of velocities. It would be then useful and logical to use a *velocity-dependent* scaling law (Leinhardt and Stewart, 2012; Stewart and Leinhardt, 2009).
10. There might be several large undiscovered families, or in other words, the lists of $D_{PB} \leqslant 100$ km families (Brož et al., 2013, or Masiero et al., 2013) might be strongly biased, because comminution is capable to destroy most of the fragments.[13]
11. Possibly, parent-body sizes D_{PB} of the observed families are systematically underestimated or their mass ratios M_{LR}/M_{PB} of the largest remnant to parent body are offset, even though they were determined by best available methods (Durda et al., 2007; Tanga et al., 1999).

The topics outlined above seem to be good starting points for (a lot of) further work.

Acknowledgments

References

Benavidez, P.G., Durda, D.D., Enke, B.L., Bottke, W.F., Nesvorný, D., Richardson, D.C., Asphaug, E., Merline, W.J., 2012. A comparison between rubble-pile and monolithic targets in impact simulations: Application to asteroid satellites and family size distributions. Icarus 219, 57–76. http://dx.doi.org/10.1016/j.icarus.2012.01.015.

Benz, W., Asphaug, E., 1999. Catastrophic disruptions revisited. Icarus 142, 5–20. http://dx.doi.org/10.1006/icar.1999.6204.

Bottke, W.F. et al., 2005. The fossilized size distribution of the main asteroid belt. Icarus 175, 111–140. http://dx.doi.org/10.1016/j.icarus.2004.10.026.

Bottke, W.F., Greenberg, R., 1993. Asteroidal collision probabilities. Geophys. Res. Lett. 20, 879–881. http://dx.doi.org/10.1029/92GL02713.

Bottke, W.F., Vokrouhlický, D., Broz, M., Nesvorný, D., Morbidelli, A., 2001. Dynamical spreading of asteroid families by the Yarkovsky effect. Science 294, 1693–1696. http://dx.doi.org/10.1126/science.1066760.

Bottke, W.F., Morbidelli, A., Jedicke, R., Petit, J.-M., Levison, H.F., Michel, P., Metcalfe, T.S., 2002. Debiased orbital and absolute magnitude distribution of the near-Earth objects. Icarus 156, 399–433. http://dx.doi.org/10.1006/icar.2001.6788.

Bottke Jr, W.F., Vokrouhlický, D., Rubincam, D.P., Nesvorný, D., 2006. The Yarkovsky and Yorp effects: Implications for asteroid dynamics. Annu. Rev. Earth Planet. Sci. 34, 157–191. http://dx.doi.org/10.1146/annurev.earth.34.031405.125154.

Bowell, E., Hapke, B., Domingue, D., Lumme, K., Peltoniemi, J., Harris, A.W., 1989. Application of photometric models to asteroids. In: Binzel, R.P., Gehrels, T.,

---

[12] Plus the 'invisible' tail implemented in the Boulder code to prevent artificial waves on the SFD.

[13] It seems that the late heavy bombardment is indeed capable to destroy $D_{PB} \leqslant 100$ km families, as concluded by Brož et al. (2013), but in this paper we focus on the last ~ 4 Gyr only and we do not simulate the LHB.

Matthews, M.S. (Eds.), Asteroids II, University of Arizona Press, Tucson, AZ, pp. 524–556.

Brož, M., Morbidelli, A., Bottke, W.F., Rozehnal, J., Vokrouhlický, D., Nesvorný, D., 2013. Constraining the cometary flux through the asteroid belt during the late heavy bombardment. Astron. Astrophys. 551, 16. http://dx.doi.org/10.1051/0004-6361/201219296. Article Id: A117.

Carruba, V., Domingos, R.C., Nesvorný, D., Roig, F., Huaman, M.E., Souami, D., 2013. A multidomain approach to asteroid families' identification. Mon. Not. R. Astron. Soc. 433, 2075–2096. http://dx.doi.org/10.1093/mnras/stt884.

Carry, B., 2012. Density of asteroids. Planet. Space Sci. 73, 98–118. http://dx.doi.org/10.1016/j.pss.2012.03.009.

Cellino, A., Zappala, V., Farinella, P., 1991. The size distribution of main-belt asteroids from IRAS data. Mon. Not. R. Astron. Soc. 253, 561–574.

Ceplecha, Z., 1996. Luminous efficiency based on photographic observations of the Lost City fireball and implications for the influx of interplanetary bodies onto Earth. Astron. Astrophys. 311, 329–332.

Dahlgren, M., 1998. A study of Hilda asteroids. III. Collision velocities and collision frequencies of Hilda asteroids. Astron. Astrophys. 336, 1056–1064.

Davis, D.R., Chapman, C.R., Greenberg, R., Weidenschilling, S.J., Harris, A.W., 1979. Collisional Evolution of Asteroids – Populations, Rotations, and Velocities, In: Asteroids. (A80-24551 08-91), University of Arizona Press, NASA-supported research, Tucson, Ariz., pp. 528–557.

Delbo', M., dell'Oro, A., Harris, A.W., Mottola, S., Mueller, M., 2007. Thermal inertia of near-Earth asteroids and implications for the magnitude of the Yarkovsky effect. Icarus 190, 236–249. http://dx.doi.org/10.1016/j.icarus.2007.03.007.

Dell'Oro, A., Paolicchi, P., 1998. Statistical properties of encounters among asteroids: A new, general, purpose, formalism. Icarus 136, 328–339. http://dx.doi.org/10.1006/icar.1998.6025.

Dell'Oro, A., Paolicchi, P., Cellino, A., Zappalà, V., Tanga, P., Michel, P., 2001. The role of families in determining collision probability in the asteroid main belt. Icarus 153, 52–60. http://dx.doi.org/10.1006/icar.2001.6621.

DeMeo, F.E., Carry, B., 2014. Solar System evolution from compositional mapping of the asteroid belt. Nature 505, 629–634. http://dx.doi.org/10.1038/nature12908.

Dohnanyi, J.S., 1969. Collisional model of asteroids and their debris. J. Geophys. Res. 74, 2531. http://dx.doi.org/10.1029/JB074i010p02531.

Durda, D.D., Bottke, W.F., Nesvorný, D., Enke, B.L., Merline, W.J., Asphaug, E., Richardson, D.C., 2007. Size–frequency distributions of fragments from SPH/N-body simulations of asteroid impacts: Comparison with observed asteroid families. Icarus 186, 498–516. http://dx.doi.org/10.1016/j.icarus.2006.09.013.

Giblin, I., Martelli, G., Farinella, P., Paolicchi, P., di Martino, M., Smith, P.N., 1998. The properties of fragments from catastrophic disruption events. Icarus 134, 77–112. http://dx.doi.org/10.1006/icar.1998.5937.

Greenberg, R., 1982. Orbital interactions – A new geometrical formalism. Astron. J. 87, 184–195. http://dx.doi.org/10.1086/113095.

Hodapp, K.W. et al., 2004. Design of the Pan-STARRS telescopes. Astron. Nachrichten 325, 636–642. http://dx.doi.org/10.1002/asna.200410300.

Jacobson, S.A., Marzari, F., Rossi, A., Scheeres, D.J., Davis, D.R., 2014. Effect of rotational disruption on the size-frequency distribution of the main belt asteroid population. Mon. Not. R. Astron. Soc. 439, L95–L99. http://dx.doi.org/10.1093/mnrasl/slu006.

Knežević, Z., Milani, A., 2003. Proper element catalogs and asteroid families. Astron. Astrophys. 403, 1165–1173. http://dx.doi.org/10.1051/0004-6361:20030475.

Leinhardt, Z.M., Stewart, S.T., 2012. Collisions between gravity-dominated bodies. I. Outcome Regimes and scaling laws. Astrophys. J. 745 (1), 27. http://dx.doi.org/10.1088/0004-637X/745/1/79. Article Id: 79.

Levison, H.F., Bottke, W.F., Gounelle, M., Morbidelli, A., Nesvorný, D., Tsiganis, K., 2009. Contamination of the asteroid belt by primordial trans-Neptunian objects. Nature 460, 364–366. http://dx.doi.org/10.1038/nature08094.

Mainzer, A. et al., 2011. Thermal model calibration for minor planets observed with wide-field infrared survey explorer/NEOWISE. Astrophys. J. 736 (2), 9. http://dx.doi.org/10.1088/0004-637X/736/2/100. Article Id: 100.

Marzari, F., Rossi, A., Scheeres, D.J., 2011. Combined effect of YORP and collisions on the rotation rate of small main belt asteroids. Icarus 214, 622–631. http://dx.doi.org/10.1016/j.icarus.2011.05.033.

Masiero, J.R., Mainzer, A.K., Grav, T., Bauer, J.M., Cutri, R.M., Dailey, J., Eisenhardt, P.R.M., McMillan, R.S., Spahr, T.B., Skrutskie, M.F., Tholen, D., Walker, R.G., Wright, E.L., DeBaun, E., Elsbury, D., Gautier IV, T., Gomillion, S., Wilkins, A., 2011. Main belt asteroids with WISE/NEOWISE.I. Preliminary albedos and diameters. Astrophys. J. 741 (2), 20. http://dx.doi.org/10.1088/0004-637X/741/2/68. Article Id: 68.

Masiero, J.R., Mainzer, A.K., Bauer, J.M., Grav, T., Nugent, C.R., Stevenson, R., 2013. Asteroid family identification using the hierarchical clustering method and WISE/NEOWISE physical properties. Astrophys. J. 770 (1), 22. http://dx.doi.org/10.1088/0004-637X/770/1/7. Article Id: 7.

Michel, P., Jutzi, M., Richardson, D.C., Benz, W., 2011. The asteroid veritas: An intruder in a family named after it? Icarus 211, 535–545. http://dx.doi.org/10.1016/j.icarus.2010.10.01.

Mignard, F. et al., 2007. The Gaia mission: Expected applications to asteroid science. Earth Moon Planets 101, 97–125. http://dx.doi.org/10.1007/s11038-007-9221-z.

Milani, A., Cellino, A., Knezevic, Z., Novakovic, B., Spoto, F., Paolicchi, P., 2013. Asteroid families classification: Exploiting very large data sets. ArXiv e-prints.

Morbidelli, A., Bottke, W.F., Nesvorný, D., Levison, H.F., 2009. Asteroids were born big. Icarus 204, 558–573. http://dx.doi.org/10.1016/j.icarus.2009.07.011.

Nesvorný, D., Jedicke, R., Whiteley, R.J., Ivezić, Ž., 2005. Evidence for asteroid space weathering from the Sloan Digital Sky Survey. Icarus 173, 132–152. http://dx.doi.org/10.1016/j.icarus.2004.07.026.

Nesvorný, D., 2010. Nesvorný HCM Asteroid Families V1.0, NASA Planetary Data System 133.

Nesvorný, D., 2012. Nesvorný HCM Asteroid Families V2.0, NASA Planetary Data System 189.

Novaković, B., Cellino, A., Knežević, Z., 2011. Families among high-inclination asteroids. Icarus 216, 69–81. http://dx.doi.org/10.1016/j.icarus.2011.08.016.

Parker, A., Ivezić, Ž., Jurić, M., Lupton, R., Sekora, M.D., Kowalski, A., 2008. The size distributions of asteroid families in the SDSS moving object catalog 4. Icarus 198, 138–155. http://dx.doi.org/10.1016/j.icarus.2008.07.002.

Press, W.H., Teukolsky, S.A., Vetterling, W.T., Flannery, B.P., 1992. Numerical Recipes in FORTRAN. The Art of Scientific Computing.

Stewart, S.T., Leinhardt, Z.M., 2009. Velocity-dependent catastrophic disruption criteria for planetesimals. Astrophys. J. 691, L133–L137. http://dx.doi.org/10.1088/0004-637X/691/2/L133.

Stuart, J.S., 2001. A near-Earth asteroid population estimate from the LINEAR survey. Science 294, 1691–1693. http://dx.doi.org/10.1126/science.1065318.

Tanga, P., Cellino, A., Michel, P., Zappalà, V., Paolicchi, P., dell'Oro, A., 1999. On the size distribution of asteroid families: The role of geometry. Icarus 141, 65–78. http://dx.doi.org/10.1006/icar.1999.6148.

Tedesco, E.F., Noah, P.V., Noah, M., Price, S.D., 2002. The supplemental IRAS minor planet survey. Astron. J. 123, 1056–1085. http://dx.doi.org/10.1086/338320.

Tedesco, E.F., et al., 2005. Albedo distributions of near-Earth and intermediate source region asteroids. In: AAS/Division for Planetary Sciences Meeting Abstracts #37. Bulletin of the American Astronomical Society, vol. 37, pp. 643.

Vokrouhlický, D., 1998. Diurnal Yarkovsky effect as a source of mobility of meter-sized asteroidal fragments. I. Linear theory. Astron. Astrophys. 335, 1093–1100.

Vokrouhlický, D., Farinella, P., 1999. The Yarkovsky seasonal effect on asteroidal fragments: A nonlinearized theory for spherical bodies. Astron. J. 118, 3049–3060. http://dx.doi.org/10.1086/301138.

Walsh, K.J., Delbó, M., Bottke, W.F., Vokrouhlický, D., Lauretta, D.S., 2013. Introducing the Eulalia and new Polana asteroid families: Re-assessing primitive asteroid families in the inner main belt. Icarus 225, 283–297. http://dx.doi.org/10.1016/j.icarus.2013.03.005.

Warner, B.D., Harris, A.W., Pravec, P., 2009. The asteroid lightcurve database. Icarus 202, 134–146. http://dx.doi.org/10.1016/j.icarus.2009.02.003.

Zappalà, V., Bendjoya, P., Cellino, A., Farinella, P., Froeschlé, C., 1995. Asteroid families: Search of a 12,487-asteroid sample using two different clustering techniques. Icarus 116, 291–314. http://dx.doi.org/10.1006/icar.1995.1127.

Paper 2

Astronomy & Astrophysics

Distribution of spin-axes longitudes and shape elongations of main-belt asteroids

H. Cibulková[1], J. Ďurech[1], D. Vokrouhlický[1], M. Kaasalainen[2], and D. A. Oszkiewicz[3, 4]

[1] Institute of Astronomy, Faculty of Mathematics and Physics, Charles University, V Holešovičkách 2, 180 00 Prague 8, Czech Republic
e-mail: cibulkova@sirrah.troja.mff.cuni.cz
[2] Department of Mathematics, Tampere University of Technology, PO Box 553, 33101 Tampere, Finland
[3] Lowell Observatory, 1400 W Mars Hill Rd, Flagstaff, 86001 AZ, USA
[4] Astronomical Observatory Institute, Faculty of Physics, Adam Mickiewicz University, Słoneczna 36, 60-286 Poznań, Poland

ABSTRACT

Context. Large all-sky surveys provide us with a lot of photometric data that are sparse in time (typically a few measurements per night) and can be potentially used for the determination of shapes and rotational states of asteroids. The method generally used to derive these parameters is the light curve inversion. However, for most asteroids their sparse data are not accurate enough to derive a unique model and the light curve inversion method is thus not very efficient.
Aims. To fully utilize photometry sparse in time, we developed a new simplified model and applied it on the data from the Lowell photometric database. Our aim was to derive spin axis orientations and shape elongations of asteroids and to find out if there are some differences in distributions of these parameters for selected subpopulations.
Methods. We modeled asteroids as geometrically scattering triaxial ellipsoids. Observed values of mean brightness and the dispersion of brightness were compared with computed values obtained from the parameters of the model, i.e., the ecliptical longitude λ and latitude β of the pole and the ratios a/b, b/c of axes of the ellipsoid. These parameters were optimized to get the best agreement with the observation.
Results. We found that the distribution of λ for main-belt asteroids is not uniform and is dependent on the inclination of the orbit. Surprisingly, the nonuniformity of λ distribution is larger for asteroids residing on low-inclination orbits. We also studied distributions of a/b for several groups of asteroids and found that small asteroids ($D < 25$ km) are on average more elongated than large ones.

Key words. minor planets, asteroids: general – methods: statistical – techniques: photometric

1. Introduction

The amount of photometric data of asteroids has been growing rapidly in recent years. These data are a source of information about shapes and rotational states of asteroids. Currently, the main method for determination of spin states and shapes of asteroids from photometry is the inversion of light curves, which was developed by Kaasalainen & Torppa (2001) and Kaasalainen et al. (2001). Models obtained with this method are stored in the Database of Asteroid Models from Inversion Techniques (DAMIT; Ďurech et al. 2010), which now contains models for 907 asteroids. The photometric data can be formally divided into two groups: (i) data dense in time that sample the rotational period well and that are typically used for the light curve inversion method, and (ii) data sparse in time (few measurements per night) that are produced by all-sky surveys, such as Pan-STARRS, Catalina, or LONEOS. Kaasalainen (2004) and Ďurech et al. (2005, 2007) showed that it is possible to get the solution of the inverse problem from sparse photometry if the data are of good quality (noise ≲5%). New asteroid models were also derived with a combination of dense and sparse photometry (Ďurech et al. 2009; Hanuš et al. 2011, 2013, 2016).

In the first statistical study of pole orientation of asteroids (based on 20 bodies), Magnusson (1986) revealed the lack of poles close to the ecliptic plane. That was later confirmed in

analyses by Pravec et al. (2002), Skoglöv & Erikson (2002), and Kryszczyńska et al. (2007) for slightly less than 100 asteroids. Hanuš et al. (2011), using a sample of 206 main belt asteroids, found the dependence of the distribution of ecliptical latitudes β on the diameter D. They found basically isotropic distribution of β value with only a slight excess of prograde rotators for $D \gtrsim 60$ km, while the distribution of β value for $D \lesssim 30$ km asteroids was found to have a strong preference for either low or high values indicating pole orientation near the pole of the ecliptic. The lack of poles near the ecliptic is most probably due to the Yarkovsky-O'Keefe-Radzievskii-Paddack (YORP) effect, which can alter the direction of the spin axes of asteroids smaller than ≈40 km on a timescale shorter than their collisional lifetime (e.g., Pravec & Harris 2000; Rubincam 2000). The distribution of ecliptical longitudes λ of spin axes was, however, supposed to be rather uniform. For instance, Davis et al. (1989) came to this conclusion from the simulations of the collisional evolution of asteroids. With the growing number of asteroids for which pole orientation have been determined, a reliable statistics could be achieved and this hypothesis could be tested. However, even for a sample of 206 asteroids, Hanuš et al. (2011) did not reveal any nonuniformity in distribution of λ, but at the same time the data sample was too small to indicate meaningful nonuniformities. On the contrary, Slivan (2002) and Slivan et al. (2003) revealed a nonuniform pole distribution for 20−35 km size members in the

Koronis family. In particular, the prograde-rotating asteroids all had ecliptic longitude between 24° and 73°. This conundrum was resolved by Vokrouhlický et al. (2003), who showed that these objects underwent a 2−3 Gyr long dynamical evolution during which the YORP effect tilted their spin axis near the ecliptic pole. Since YORP also continued to decrease the rotation frequency in their model, the spin state was captured in the Cassini resonance between the pole precession owing to solar torque and orbit precession from Jupiter-Saturn perturbations. The stationary point of this particular secular, spin-orbit resonance is currently at ≃35° ecliptic longitude. Thus all bodies whose spin axes librate about this point must have λ near this value. More recently, Bowell et al. (2014) estimated the ecliptical longitudes λ for more than 350 000 asteroids of the main belt using the magnitude method (Magnusson 1986), based on the variation of brightness with the ecliptical longitude: the maximum of brightness corresponds with the spin axis pointing either toward or opposite from the Earth. Surprisingly, the resulting distribution is clearly nonuniform with an excess of asteroids with λ from 30° to 110° and with minimum for 120° to 160°.

The success of getting a unique solution of the inverse problem with currently available sparse photometric data (which are not accurate enough) is low. Nevertheless, using the distributed computing project Asteroids@home (Ďurech et al. 2015), which significantly reduces the computational time of the period search, Ďurech et al. (2016) derived 328 new models from the analysis of Lowell photometric data. This is an impressive, but still small increase in number to enable a population-wide study. For this reason, we describe a new method for the determination of the orientations of spin axes and shapes of asteroids to utilize photometric data sparse in time. The uncertainties of spin vectors are large for individual bodies, therefore we work with groups of asteroids and construct distributions of tested parameters because working with large samples of bodies should smear uncertainties of individual solutions and, if uncorrelated, the results should hold in a statistical sense.

The structure of this paper is as follows: in Sect. 2, we describe our model and test its reliability on synthetic data; in Sect. 3, we apply the model to the photometric data from the Lowell Observatory database and construct the distributions of ecliptical longitudes for main-belt asteroids and for several groups of asteroids; Sect. 4 deals with distributions of the ratio a/b of axes of asteroids and, in Sect. 5, we summarize the main results.

2. Model

In the light curve inversion method, all parameters describing the rotational state (i.e., the rotational period and orientation of the spin axis), shape, and light scattering on the surface are fitted, and the unique sidereal rotational period P has to be determined. In the case of dense photometric data, we can substantially reduce the computational time necessary for the determination of P by only searching the interval around the value estimated from dense light curves. For sparse data, we usually do not have any estimate of P and we have to search the interval of all possible values, which is time consuming. Moreover, for the majority of asteroids we currently do not have sparse data that is accurate enough to derive a unique rotational period. Therefore, to fully utilize sparse photometry, we developed a new model, which does not allow us to determine the rotational period, but provides an approximate solution for the orientation of the spin axis and the shape parameters of the asteroid.

We model asteroids as geometrically scattering triaxial ellipsoids ($a \geq b \geq c = 1$) rotating about the shortest axis of the inertia tensor. The parameters of the model are the ecliptic longitude λ and latitude β of the pole and the ratios of axes a/b and b/c of the ellipsoid, alternatively axes a and b. The advantage of this model is that the brightness L, which is proportional to the projected area of the illuminated and visible part of the surface, can be computed analytically (Connelly & Ostro 1984) as follows:

$$L \propto \frac{\pi abc}{2}\left(\sqrt{\boldsymbol{e}^{\mathrm{T}}M\boldsymbol{e}} + \frac{\boldsymbol{e}^{\mathrm{T}}M\boldsymbol{s}}{\sqrt{\boldsymbol{s}^{\mathrm{T}}M\boldsymbol{s}}}\right), \tag{1}$$

where $\boldsymbol{e}$, $\boldsymbol{s}$ are unit vectors defining the position of the Earth and the Sun in the asteroid coordinate system of principal axes of the inertia tensor, and

$$M = \begin{pmatrix} 1/a^2 & 0 & 0 \\ 0 & 1/b^2 & 0 \\ 0 & 0 & 1/c^2 \end{pmatrix}. \tag{2}$$

In a special case of opposition $\boldsymbol{e} = \boldsymbol{s}$, the Eq. (1) simplifies to

$$L \propto \pi abc \sqrt{\boldsymbol{e}^{\mathrm{T}}M\boldsymbol{e}}. \tag{3}$$

The direction toward Earth can be described by the rotational angle ϕ and aspect angle θ (i.e., angle between $\boldsymbol{e}$ and the direction of the spin axis),

$$\boldsymbol{e} = [\sin\theta\cos\phi, \sin\theta\sin\phi, \cos\theta]^{\mathrm{T}}. \tag{4}$$

Having set $c = 1$, the squared brightness L^2 normalized by the maximal possible value πab is

$$L^2 = \frac{\sin^2\theta\cos^2\phi}{a^2} + \frac{\sin^2\theta\sin^2\phi}{b^2} + \cos^2\theta. \tag{5}$$

The mean quadratic brightness over one rotational period is then

$$\langle L^2 \rangle = \frac{1}{2\pi}\int_0^{2\pi} L^2 \mathrm{d}\phi = 1 + \frac{1}{2}\sin^2\theta\left(\frac{1}{a^2} + \frac{1}{b^2} - 2\right), \tag{6}$$

and the normalized dispersion of squared brightness is

$$\begin{aligned}
\eta &= \frac{\sqrt{\mathrm{var}(L^2)}}{\langle L^2 \rangle} = \frac{\sqrt{\langle(L^2 - \langle L^2\rangle)^2\rangle}}{\langle L^2 \rangle} \\
&= \frac{a^2 - b^2}{\sqrt{8}}\left[\frac{a^2 b^2}{\sin^2\theta} + \frac{1}{2}\left(a^2 + b^2 - 2a^2 b^2\right)\right]^{-1}. \tag{7}
\end{aligned}$$

We used Eqs. (6) and (7), to compute $\langle L^2_{\mathrm{model}}\rangle$ and η_{model} for each asteroid and for each of its apparition; we defined apparitions as sets of observations with the gap between these sets of at least 100 days.

For the observational data, we used the following procedure:

1. We remove the dependence on solar phase angle. The changes in brightness in the light curve of an asteroid are not only due to the rotation but also the geometry of observation. In the model, we assume the case of opposition, which means the solar phase angle $\alpha = 0$. For the observational data, we fitted the dependence of the brightness on the solar phase angle α by a linear-exponential dependence similar to Hanuš et al. (2011), i.e.,

$$g\left(h\exp^{-\alpha/d} - k\alpha + 1\right)\frac{1 + \cos\alpha}{2}, \tag{8}$$

where g, h, d, k are parameters fitted for each asteroid, and we divided the observed brightness by that function. As an example, the corrected data for asteroid (511) Davida are shown in Fig. 1.
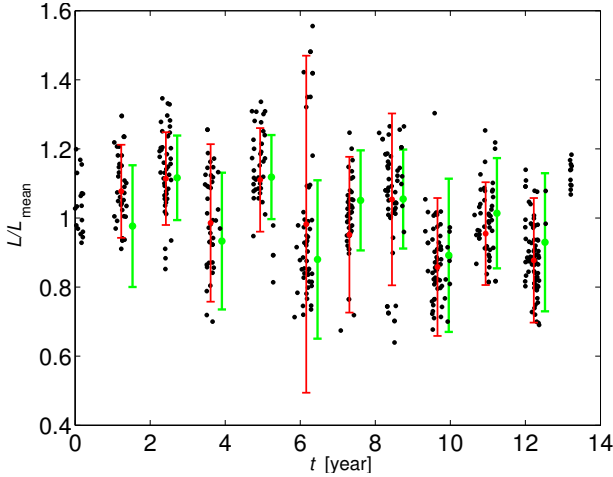
Fig. 1. Photometric data of the asteroids (511) Davida corrected by the influence of the solar phase angle (black points). Red points with vertical lines denote the observed mean brightness and its dispersion in individual apparitions, green color denotes the same but calculated quantities for the best-fit model. To normalize L, we divided each value by mean value of L calculated over all apparitions.

2. Then, we required that there were enough data for each asteroid: at least 20 points in one apparition and at least five apparitions for one asteroid (in Fig. 1 there are data from ten apparitions that can be used).

Computed theoretical values of the mean brightness $\langle L^2 \rangle$ and of the dispersion of the brightness η can be compared with observation by χ^2 that we define as:

$$\chi^2 = \chi^2_\eta + w\chi^2_{L^2} = \sum_{\text{apparitions}} \frac{(\eta_{\text{model}} - \eta_{\text{obs}})^2}{\sigma^2_\eta}$$
$$+w \sum_{\text{apparitions}} \frac{(\langle L^2_{\text{model}} \rangle / \overline{\langle L^2_{\text{model}} \rangle} - \langle L^2_{\text{obs}} \rangle / \overline{\langle L^2_{\text{obs}} \rangle})^2}{\sigma^2_{L^2}}, \quad (9)$$

where σ denotes the standard deviation and w denotes the weight for χ^2 of brightness. To normalize values of calculated and observed mean quadratic brightness, we divided them by $\overline{\langle L^2_{\text{model}} \rangle}$ and $\overline{\langle L^2_{\text{obs}} \rangle}$, respectively, which are mean values calculated over all apparitions. The value of w is not set in advance and has to be found by testing on known data. Since $\langle L^2 \rangle$ and η are not Gaussian random variables, the χ^2 in relation (9) is not χ^2 distributed. Nevertheless, we use this χ^2 formalism to define the best solution, which has the minimum χ^2.

In passing we note that in combining Eqs. (6) and (7) we obtain, for a given asteroid, the relation between $\langle L^2 \rangle$ and η,

$$\eta = \frac{1}{\sqrt{2}} \frac{a^2 - b^2}{a^2 + b^2 - 2a^2b^2} \left[1 - \frac{1}{\langle L^2 \rangle} \right]. \quad (10)$$

This implies that for larger $\langle L^2 \rangle$ the model predicts smaller dispersion η. This is in accord with the intuition that a larger brightness corresponds to the pole-on geometry of view (i.e., smaller aspect angle θ).

To find a model with the best agreement (the lowest χ^2) between the calculated values and the observation, we computed model values on a grid in parameter space: the ecliptical longitude of the pole from 0° to 360°; the latitude from 0° to 90°, both with a 5° step, and the axes a and b, from 1.1 to 4 and from 1 to a, respectively, both with a 0.1 step (an elongation larger than

4:1 would be unrealistic). As mentioned above, we corrected the observed brightness to the solar phase angle $\alpha = 0$, however, the geometry remained unchanged and the aspect angle θ, which appears in Eqs. (6) and (7), was calculated for each apparition as a mean value as follows:

$$\cos \theta_{\text{mean}} = \boldsymbol{v} \cdot \boldsymbol{e}_{\text{mean}}, \quad (11)$$

where $\boldsymbol{v} = [\cos\beta \cos\lambda, \cos\beta \sin\lambda, \sin\beta]^T$ is the vector defining the direction of the spin axis and $\boldsymbol{e}_{\text{mean}}$ is the mean vector defining the position of the Earth during one apparition. From the relation (11) we can see that we obtain the same aspect angle for λ, β and $\lambda \pm 180°$, $-\beta$, which is the reason why we test β only in the interval from 0° to 90°. Relation (11) also indicates that, for most asteroids, there is only a slightly worse second minimum of χ^2 for $\lambda \pm 180°$. For zero inclination of orbit ($e_z = 0$), the aspect angle would be the same for λ and $\lambda \pm 180°$. Owing to this ambiguity in λ, we constructed distributions of λ only in the interval 0°–180° and for $\lambda > 180°$ we used modulo 180°.

2.1. Testing of the model on synthetic data

To test our model and confirm its reliability, we created synthetic data. We computed the brightness of asteroids using the models from DAMIT database and the Hapke scattering model (Hapke 1981, 1993) with randomly chosen parameters, and we assigned these new (synthetic) values to asteroids contained in the Lowell database (to the time of observation and the appropriate geometry). The distribution of poles for this synthetic data was isotropic.

We added the Gaussian noise (we tested noise $\sigma_L = 0.15$ and 0.2), which was then subtracted according the relation

$$\eta_{\text{obs}} = \sqrt{\eta^2 - \sigma^2_{L^2}} = \sqrt{\eta^2 - 4\sigma^2_L} \quad (12)$$

if $\eta \geq 2\sigma_L$, else $\eta_{\text{obs}} = 0$. For the real data, we only have an estimate of the noise level and we attempt to subtract different values from the data to find the best results. We also tested synthetic data without any noise ($\sigma_L = 0$).

After applying our model on these data, we should obtain uniform distributions of the ecliptical longitudes λ and latitudes $\sin\beta$. This was satisfied for the resulting distribution of λ, however, the distribution of latitudes showed a preference for high β. The possible explanation is that we did not include the uncertainties from the Hapke model and from the assumption that asteroids are triaxial ellipsoids. That means, for example, that for synthetic data without any noise and for an asteroid with $\beta = 0$, there are still some changes in brightness that our model interprets as nonzero β. To improve the model we added a new parameter that we called model noise σ_{model}. Then Eq. (12) had to be changed to

$$\eta_{\text{obs}} = \sqrt{\eta^2 - 4\sigma^2_L - \sigma^2_{\text{model}}} \quad (13)$$

if $\eta \geq \sqrt{4\sigma^2_L + \sigma^2_{\text{model}}}$, else $\eta_{\text{obs}} = 0$.

We tested values $\sigma_{\text{model}} = 0.05$, 0.06, 0.07 and 0.1. The resulting distributions of λ were uniform independently on σ_{model}. This is probably because λ is principally determined from the mean brightness $\langle L^2 \rangle$, which is comparatively more stable than the dispersion of brightness η from which β is determined. In the left panel of Fig. 2, there are shown distributions of $\sin\beta$ for the two best values of σ_{model} and for the data noise $\sigma_L = 0$. The distributions are clearly nonuniform, nevertheless this is the best
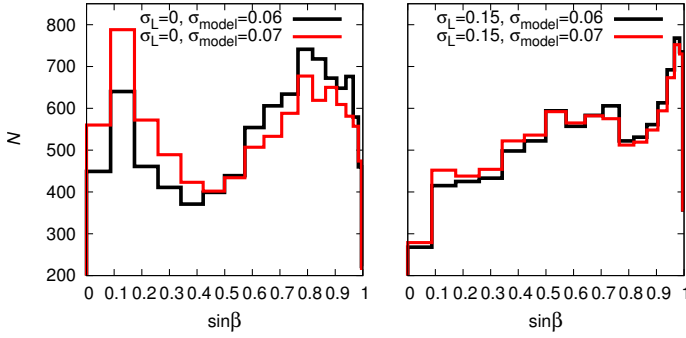
Fig. 2. Distributions of ecliptical latitudes β calculated from synthetic data with noise $\sigma_L = 0$ (*left*) and $\sigma_L = 0.15$ (*right*) for two best values of $\sigma_{\rm model}$.

result we obtained. When we added noise to the synthetic data, we found that there is no significant difference between distributions of $\sin\beta$ for $\sigma_{\rm model} = 0.06$ and 0.07 (see Fig. 2 on the right) and, therefore, we decided to use the value 0.06 for the real data.

The takeaway message from our tests is that (i) determination of λ is reliable in a statistical sense, while (ii) determination of β is subject to systematic bias that needs to be corrected before interpreting the results.

3. The distribution of ecliptical longitudes

Having tested our approach and calibrated its parameters, we now construct the distribution of ecliptical longitudes for the real data from the Lowell Observatory photometric database (Bowell et al. 2014). This database contains data from 11 observatories, which are stored in the Minor Planet Center. The data were calibrated using the broadband accurate photometry of the Sloan Digital Sky Survey; the accuracy is ∼0.1−0.2 mag. For more information about the data reduction and calibration, see Oszkiewicz et al. (2011).

First, we applied our model to 765 asteroids included in DAMIT database (from the first 10 000 numbered asteroids, which are included in the Lowell Observatory database and satisfy the conditions on the number of apparitions and the number of measurements in one apparition) and tried different values of noise σ_L (0.08, 0.1, 0.12, 0.15) and weight w (1, 5, 25); the value of model noise was 0.06. To decide on the best noise level and weight, we compared the calculated λ and β with $\lambda_{\rm DAMIT}$ (values from DAMIT derived with the light curve inversion) and $\beta_{\rm DAMIT}$, respectively. From the distributions of $\Delta\lambda = |\lambda - \lambda_{\rm DAMIT}|$, we found the best value of weight as $w = 5$ and from the distributions of $\Delta\beta$ we found the best value of noise level as $\sigma_L = 0.08$. However, we revealed that with this assumed data noise, the model produces hardly any spheroidal asteroids $a/b \sim 1$. This is because the photometric data for less bright asteroids have higher noise level than for brighter asteroids. In DAMIT, there are preferentially brighter asteroids, hence the noise level 0.08 works for them, but for less bright asteroids, such noise level is underestimated. To estimate the dependence of σ_L on L we used the amplitudes $A_{\rm mag}$ of light curves stored in the Asteroid Lightcurve Database (LCDB)[1] compiled by Warner et al. (2009). For $A_{\rm mag}$ we can write

$$A_{\rm mag} = 2.5 \log \frac{L_{\rm max}}{L_{\rm min}} = 2.5 \log \frac{L_{|\phi=0}}{L_{|\phi=\pi/2}} , \tag{14}$$

---
[1] http://www.minorplanet.info/lightcurvedatabase.html
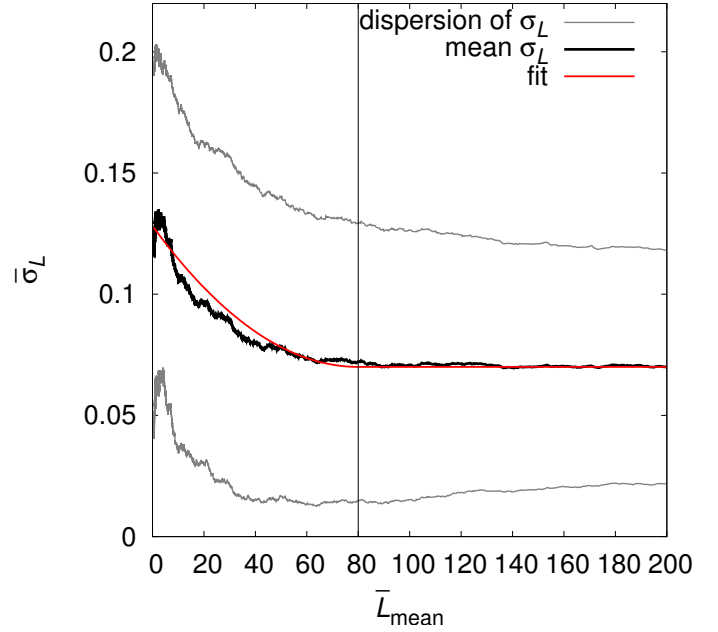
Fig. 3. Dependence of the mean value of noise level σ_L on the mean value of $L_{\rm mean}$; $L_{\rm mean}$ is mean brightness over all apparitions. Each mean value was calculated from a sample of 500 asteroids (as described in the main text). Gray lines denote dispersions of σ_L among corresponding 500 bodies. The red line denotes the fit that was applied in the model.

where L is given by Eq. (5). The normalized dispersion of brightness η, defined by Eq. (7), is then related with amplitude as

$$\eta_A = \frac{1}{\sqrt{8}} \left(\frac{1}{1 - A^2} - \frac{1}{2} \right)^{-1} , \tag{15}$$

where $A = L_{\rm min}/L_{\rm max} = 10^{-0.4A_{\rm mag}}$. For 9698 asteroids included in LCDB, we calculated η_A according Eq. (15) and then the appropriate noise level in data for each asteroid is written as:

$$\sigma_L = \left(\sqrt{\eta^2 - \eta_A^2 - \sigma_{\rm model}^2} \right)/2 \tag{16}$$

if $\eta > \sqrt{\eta_A^2 + \sigma_{\rm model}^2}$, else $\sigma_L = 0$. We calculated the running mean of σ_L for the sample of 500 bodies to obtain the dependence of σ_L on the mean brightness over all apparitions $L_{\rm mean}$. The resulting dependence, with dispersion of σ_L among corresponding 500 bodies, is shown in Fig. 3. We applied this dependence in our model as follows: we assumed the noise level $\sigma_L = 0.07$ for asteroids with $L_{\rm mean} > 80$; the brightness here is a dimensionless quantity calculated from magnitude M as $L = 10^{-0.4(M-15)}$. For asteroids less bright than 80, we calculated the noise level according to the equation of parabola,

$$\sigma_L = 0.07 + \frac{(L_{\rm mean} - 80)^2}{2 \times 55\,000} . \tag{17}$$

The appropriate curve is shown in Fig. 3 (red line). We can see it does not fit the data perfectly, nevertheless, considering the dispersion of values of σ_L (gray lines), such deviation is insignificant.

The Lowell Observatory database contains, in total, data for 326 266 asteroids. For 69 053 asteroids, there were enough apparitions and data points to calculate ecliptical longitude λ and latitude β; the vast majority of these asteroids belong to the first 100 000 numbered asteroids. For this sample, we used our model
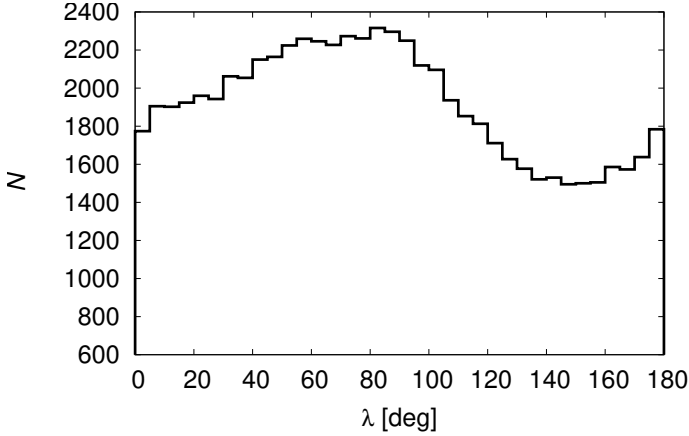
Fig. 4. Distribution of λ derived for 69 053 asteroids from the Lowell Observatory photometric database with model noise $\sigma_{model} = 0.06$ and weight $w = 5$. The values of λ larger than $180°$ map to the values $\lambda - 180°$, because of the symmetry of the model.

with weight $w = 5$, model noise 0.06, and data noise calculated for each asteroid according to the rule described above. The resulting distribution of the ecliptical longitude λ of asteroid pole orientation, shown in Fig. 4, is clearly nonuniform. As we can see, there is an excess of asteroids with λ from $40°$ to $100°$ and a minimum for $\lambda \sim 150°$. We calculated the Kolmogorov-Smirnov (KS) test of this distribution with a uniform one. The probability that they belong to the same parent distribution Q_{KS} is almost zero. A similar result was obtained by Bowell et al. (2014), who determined λ from the maximum of a sinusoid curve fitting the variation of brightness.

The distribution of ecliptical latitudes β shows strong preference for $\sin\beta \gtrsim 0.9$, however, since the distribution of $\sin\beta$ for the synthetic data was not uniform (Fig. 2), the determined ecliptical latitudes are affected by biases and uncertainties that are not properly modeled here; therefore, in the following text we mainly study the distribution of ecliptical longitudes λ.

3.1. Searching for an explanation

Up to now, there is no satisfactory explanation of such nonuniformity in the distribution of ecliptical longitudes λ. We considered the observational and method biases described in Marciniak et al. (2015) and Santana-Ros et al. (2015), nevertheless, we found these do not influence our results; therefore, we searched for some other observational biases and geometrical and dynamical effects as well.

3.1.1. Galactic plane bias

First, we tested the influence of the measurements near Galactic plane, where the stellar background is more dense and thus the measurements may have higher uncertainties. We eliminated the observations with Galactic latitude $|b| < 10°$ and repeated the analysis; for one asteroid there were on average about 6% less points. The differences between computed λ and λ from the DAMIT database were comparable with values for the model with the Galactic plane, however, the nonuniformity in λ was even larger. This result could suggest that, on the contrary, the shortage of observations near the Galactic plane could cause the nonuniformity of λ. However, if such a bias could influence our results, it would have also been seen in our test with synthetic data, since the geometry of observations was kept unchanged.
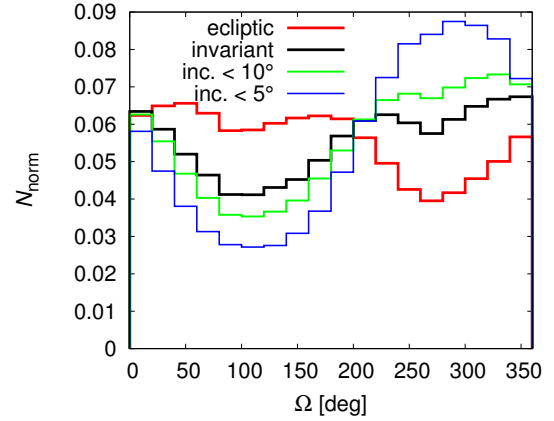

Fig. 5. Distribution of the longitudes of ascending node Ω (from AstOrb catalog) for the asteroid main belt. The red curve represents the distribution in the ecliptic plane; the black curve indicates the distribution in the invariant (Laplace) plane. The green and blue lines represent the distribution in the invariant plane for asteroids with the inclination of the orbit $I < 10°$ and $I < 5°$, respectively.

Nevertheless, the resulting distribution of ecliptical longitudes was uniform, therefore, we believe our results are not influenced by such bias and we had to look for another explanation.

3.1.2. Correlation with longitude of ascending node

Next, we studied the role of the orbital longitude of node Ω by examining a possible correlation between asteroid's pole longitude λ and Ω. The orbital data were taken from the AstOrb catalog[2]. Figure 5 shows distribution of Ω values for 566 089 multi-opposition orbits of main-belt asteroids.

Focusing first on the data in the ecliptic reference system, we note that Ω values show overpopulation centered at $\simeq100°$ value, and underpopulation shifted by about $180°$, i.e., centered at $\simeq270°$ value. This result is not new (see, e.g., JeongAhn & Malhotra 2014, and references therein). The reason for this nonuniformity in Ω is due to planetary perturbations. The distribution of Ω transformed to the Laplace plane shows similar nonuniformity, only shifted by $\sim180°$; this is due to a slight but significant $\simeq1.58°$ tilt between the ecliptic plane and invariant plane of planets. For small-inclination orbits (i.e., whose proper inclination value is small), this effect becomes larger, as also shown in Fig. 5. Having learned about the nonuniformity of osculating nodal longitudes of asteroids in the main belt we should now examine, whether the nonuniform distribution of their pole longitudes λ is not a simple implication of the primary effect in nodes.

First, we ran the following experiment. We divided the asteroid population according to their value of Ω to 18 equal bins (each $20°$ wide). We found the bin that contains the smallest number N of asteroids, and from all other bins we randomly selected N objects. That way, we had a sample of asteroids whose distribution of nodes was uniform. We examined distribution of rotation poles of this subsample, in particular the distribution of their λ values, and we found it is still nonuniform, resembling that in Fig. 4. The KS test of compatibility of the λ distributions obtained from our subsample and the whole sample of asteroids gave us a likelihood $Q_{KS} \simeq 0.90$ that they have the same parent distribution. We repeated our experiment several times, creating new subsamples, and obtained the same results. We also ran the
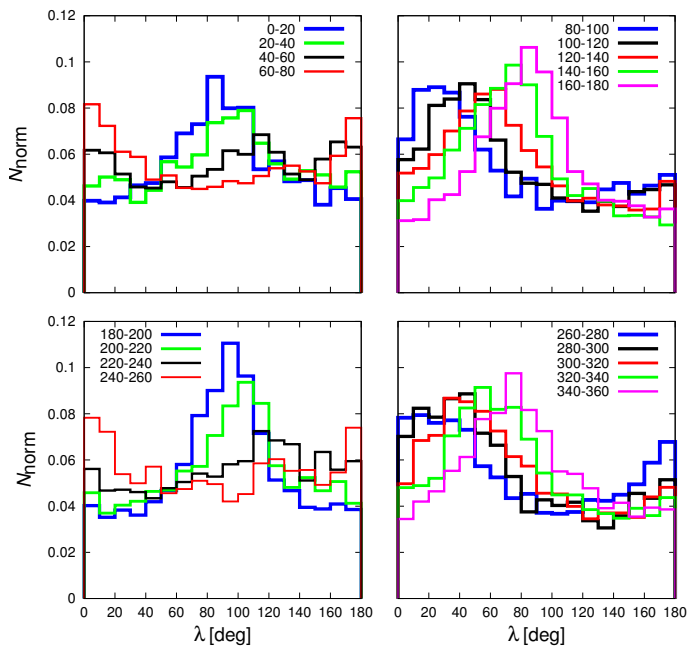
---

[2] ftp://ftp.lowell.edu/pub/elgb/astorb.html

Fig. 6. Distributions of ecliptical longitudes λ of poles for different longitudes of ascending node Ω.

same experiment in the Laplace reference system, but the choice of reference plane does not influence the results. These experiments suggest that nonuniformity in the distribution of orbital nodes does not play fundamental role in the nonuniform distribution of pole longitudes of asteroid spins.

Yet, we would expect some relation between Ω and λ should exist. For instance, plotting λ distributions for asteroids in each of the Ω bins described above, we obtained data shown in Fig. 6. The results indicate that in each of the bins of restricted Ω values, distribution of pole longitude peaks at $\simeq(\Omega - 90°)$. This is actually understandable in the simplest model, in which the spin axis of each asteroid just uniformly precesses about the normal to its osculating orbit due to solar gravitational torque. We have quantitatively tested how much a simple geometrical effect of such precession could contribute to the observed dependence of ecliptical longitude λ on node Ω. To that goal we assumed the pole position in the moving orbital plane is set with the obliquity ϵ and we chose the inclination of orbit I and the longitude of ascending node Ω. This initial set up was changed several times, specifically, we tested values of inclination $\sin I = 0.10$, 0.15, 0.30, values of node $\Omega = 10°$, $170°$, $250°$ and values of obliquity $\epsilon < I$, $\epsilon > I$. Assuming a simple regular precession, we randomly picked many values of longitude φ, uniform in $0°$ to $360°$. We then transformed poles to the ecliptic system, determined appropriate λ and construct a model distribution of the ecliptical longitudes. Results of these simple simulations satisfied our hypothesis of geometrical effect; for $\epsilon < I$, the distribution of λ was only a tight interval of values near $\simeq(\Omega - 90°)$, and for $\epsilon > I$, the λ values ranged the whole interval from $0°$ to $360°$, but with a peak at $\simeq(\Omega - 90°)$. However, when we summed distributions of λ for values of ϵ from assumed distribution $n(\cos \epsilon)$ for a fixed I and Ω, we reached an almost uniform final distribution, which is far from the distributions shown in Fig. 6. We tested $n(\cos \epsilon)$ uniform and also some unrealistic distributions, for example, we assumed there were ten times more bodies with $\epsilon < 45°$ than with $\epsilon > 45°$, but with insignificant effect on the final distribution.

Therefore, using two lines of evidence we show that the nonuniformity of the ecliptic Ω values together with only simple geometric (projection) effects cannot explain the nonuniformity in the distribution of pole ecliptic longitudes. However, the flow of pole orientation in the orbit frame may be much more complicated than just a simple steady precession about the orbital angular momentum vector. This is because of a possibility of resonant, spin-orbit effects described by Cassini dynamics (e.g., Colombo 1966; Henrard & Murigande 1987; Vokrouhlický et al. 2006). In fact, the large-asteroid subgroup in the Koronis family, the Slivan sample, has actually been identified as being captured in the most prominent s_6 Cassini resonance resulting in a common orientation of their pole longitudes near the stationary point at ecliptic longitude $\simeq 35°$ (e.g., Vokrouhlický et al. 2003). Therefore, we examined whether such resonant effects could help us to explain the nonuniformity in the λ distribution.

However, we found the answer is negative. First, if the capture in the aforementioned Cassini resonance played a dominant role population wise, the pole longitude distribution would be peaked at the stationary point of the resonance (shifted by some $35°-40°$ from the maximum seen in Fig. 4). Next, Vraštil & Vokrouhlický (2015) have shown that the capture in this resonance is generally unstable (especially in the inner part of the main belt), and that its phase volume is small (few percent at maximum). The latter implies that expecting the spin pole located in this resonance by chance is very small. In order to verify these preliminary conclusions, we used the software described in Vraštil & Vokrouhlický (2015) to probe the expected effect. This is basically much more sophisticated variant of our previous Monte Carlo experiment in which we assumed a steady precession in the orbit frame. Here we propagated orbit and spin evolution of the first 10 000 main belt asteroids, giving them random initial rotation state parameters, such as rotation period, pole orientation, and dynamical ellipticity. We then numerically propagated orbit and spin evolution for tens of millions of years and monitored distribution of simulated ecliptic longitudes of the sample. We found the sample quickly forgets given initial conditions and fluctuates about a steady-state situation with basically uniform distribution of ecliptic longitudes of rotation poles. We repeated the numerical experiment several times with different initial conditions but always obtained very similar results.

3.2. Distributions of λ for groups of asteroids

Our next step was to study the distributions of λ for various groups of asteroids, specifically for asteroids with different sizes, different spectral types, dynamical families, and asteroids in different parts of the main belt. Distributions were again compared using the KS test.

3.2.1. Asteroids with different sizes

We divided asteroids into eight groups according their diameters: 0–3; 3–6; 6–9; 9–12; 12–15; 15–25; 25–50; and 50–1000 km; the number of asteroids decrease with higher diameters, therefore, we chose wider ranges of bins. We preferentially used diameters derived from the observations of the WISE satellite (Masiero et al. 2011)[3]. For asteroids not included there, we used diameters from AstOrb catalog. We compared distributions with each other and found that the differences are not significant, which means that the data do not reveal any dependence of λ on size.

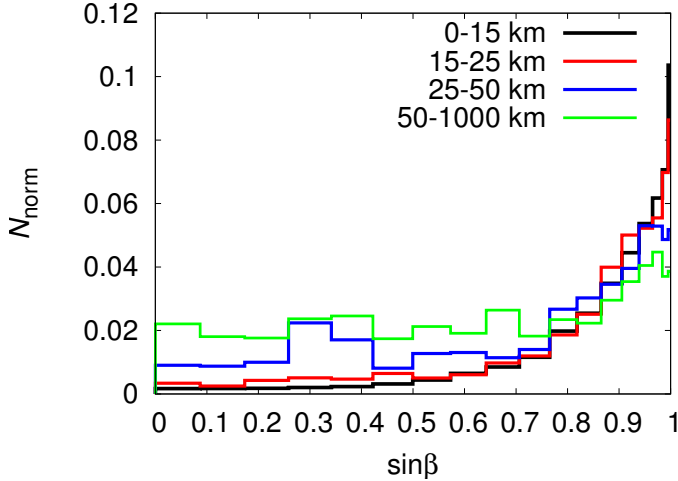[3] http://wise2.ipac.caltech.edu/staff/bauer/NEOWISE_pass1/

Fig. 7. Distribution of ecliptical latitudes β for groups of asteroids with different sizes. All distributions are divided by the distribution for synthetic data with noise 0.15 and model noise 0.06 (Fig. 2 on the right, black curve). This is the simplest debiasing procedure we can use.

We also studied the dependence of ecliptical latitude β on size and tried to confirm the result from Hanuš et al. (2011). In Fig. 7, we can see that, even though the distributions show preference for $\sin\beta \gtrsim 0.9$, with decreasing diameter D, there is a visible depopulation of spin axes close to the ecliptic plane, which is in agreement with findings of Hanuš et al. (2011).

This is yet another interesting hint about the origin of the nonuniformity of λ distribution. The affinity of latitudes toward extreme values for small asteroids clearly shows that the YORP effect has been affecting the population in a size selective way exactly predicted by the theory. However, the distribution of the longitudes does not indicate this size-selectivity, implying the YORP effect is not the primary mechanism in the longitude story. Indeed, the theory of the YORP effect so far has not predicted any significant effects for the pole longitude.

3.2.2. Taxonomic classes

We compared distributions of λ between asteroids belonging to the taxonomic class C and S (using the AstOrb catalog), which are the largest groups. The result of KS test, $Q_{KS} = 0.45$, indicates that there is no significant difference. The fact that the distribution of λ is independent of the sizes and taxonomic classes simplified tests with other subpopulations.

3.2.3. Different parts of the main belt

We also studied the distributions of λ for groups of asteroids located in different parts of the main belt. Specifically, asteroids with different inclinations $\sin I$, eccentricities e, and semimajor axes a of their orbits. We found that the distribution of λ is not dependent on the eccentricity, however it is strongly dependent on the inclination (see Fig. 8). For $\sin I < 0.02$ there is a huge excess of asteroids with λ from $60°$ to $100°$, there are more than four times more bodies than for $\lambda \sim 150°$. With increasing I the distributions are closer to the uniform distribution. This result is surprising and it actually goes against the ideas about simple geometrical (projection) effects discussed in Sect. 3.1.2, suggesting that perhaps some unidentified yet dynamical effects are at play.

We also studied the dependence of the distribution of λ on the inclination of orbit in the invariant plane. Although the
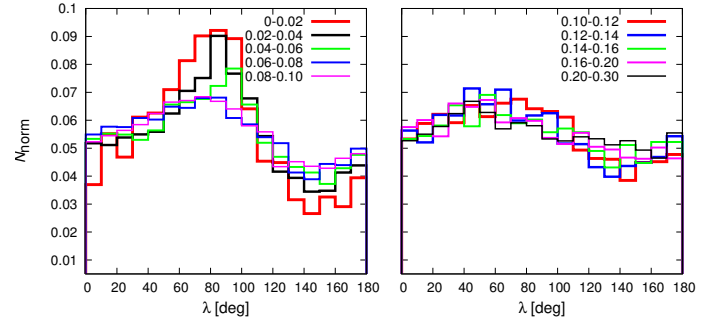

Fig. 8. Distributions of ecliptical longitudes for asteroids with different inclinations $\sin I$ of their orbits.
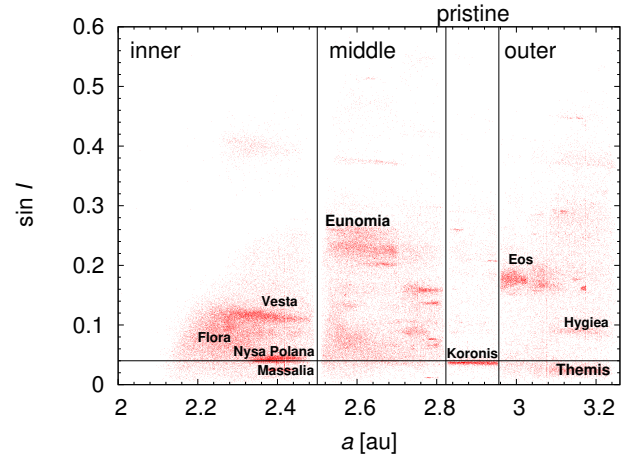

Fig. 9. Four parts of the main asteroid belt defined according to the proper semimajor axis a (we used proper values of a and I from Asteroids Dynamic Site; Knežević & Milani 2003). The number of objects plotted here is 100 000. The horizontal line separates the region $\sin I < 0.04$, for which the maximum of distributions of λ for $\lambda \sim 80°$ is highest. The locations of some more populous asteroid families are emphasized.

maximum of distribution for $\sin I < 0.02$ is slightly lower, there is still strong dependence on the inclination.

We constructed distributions of λ for individual Ω bins (as in Fig. 6) for asteroids with $\sin I < 0.04$. The peaks of all distribution were for λ from $60°$ to $100°$, which corresponds with the distribution of λ for small inclinations. This means that for orbits with small inclination, the dependence of λ on Ω is suppressed.

We then constructed distributions for asteroids with different semimajor axes a. We separated the main belt into four parts (see Fig. 9), the inner, middle, pristine[4], and outer belt, which are separated by mean-motion resonances with Jupiter. To eliminate the dependence on the inclination of orbit we divided asteroids of each part into bins with different inclination (we used the same bins as in Fig. 8) and we randomly chose such number of asteroids to have the same number of asteroids in corresponding bins of two populations. In other words, the distributions of inclination of orbit for the compared populations were the same. The results of KS tests show that only the pristine zone, bracketed by the powerful mean motion resonances 5/2 and 7/3 with Jupiter at $\simeq 2.82$ au and $\simeq 2.96$ au, has significantly different distribution from the middle and outer belt ($Q_{KS} < 3\times 10^{-6}$); specifically, the nonuniformity is more significant in pristine zone than in other parts. For the pair inner belt and pristine zone, the KS test gives $Q_{KS} = 0.00013$.

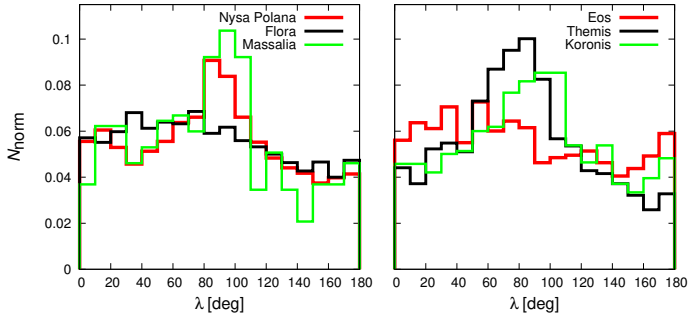[4] We adopted the word pristine from Brož et al. (2013).

Fig. 10. Distributions of λ for Flora, Nysa Polana, and Massalia (*left*). The distributions of λ for Eos, Themis, and Koronis (*right*).

3.2.4. Dynamical families

Finally, we studied dynamical families. The family membership of asteroids was taken from Nesvorný et al. (2015). Distributions of individual families were compared with the distribution of corresponding background formed with asteroids from the same part (inner, middle, pristine, and outer) as the family and with inclinations of orbit from the interval defined by the members of the family. The KS test did not reveal any significant difference between any family and its background. We also compared families located approximately in the same interval of inclination (see Fig. 9) with each other, specifically: Themis with Massalia; Vesta with Eos, Hygiea and Flora; Hygiea with Flora; and Koronis with Nysa Polana. Again, the KS test showed no difference for these pairs of families. The distributions of λ for six selected families are shown in Fig. 10. The differences we can see between the distributions are caused only due to the dependence on the inclination of orbit.

The strong maximum of the λ distribution between $\simeq (80°-110°)$ in the Koronis family does not fit the interval of expected librators in Slivan states described by Vokrouhlický et al. (2003) which would be shifted by about 40° to 50° degrees toward lower values.

3.3. The bootstrap method

Formally, it is always possible to find the best ecliptical longitude λ and latitude β of the pole, i.e., the lowest χ^2. However, the minimum can be flat and in that case λ is not well determined. To estimate the errors of determined longitudes we applied the bootstrap method (Davison & Hinkley 1997) on the set of measurements for each asteroid; we used the first 10 000 numbered asteroids from the Lowell Observatory database, of which for 9774 there were enough data points. From the set we randomly selected data to get the same number of measurements, but some of them were chosen more than once and some of them were missing. We repeated this ten times, therefore, we obtained ten modified sets of measurements and thus ten possible longitudes for each asteroid. We considered that the longitude was well determined when the maximum difference among ten values of λ was $\leq 50°$. This was satisfied for 3930 from 9774 asteroids; the mean value of the largest differences for these bodies is 30°. The dependences of λ on the longitude of ascending node Ω and on the inclination of orbit I for this new sample of 3930 asteroids did not significantly change, which means that the poorly constrained models did not cause any systematic effect to distribution of λ.
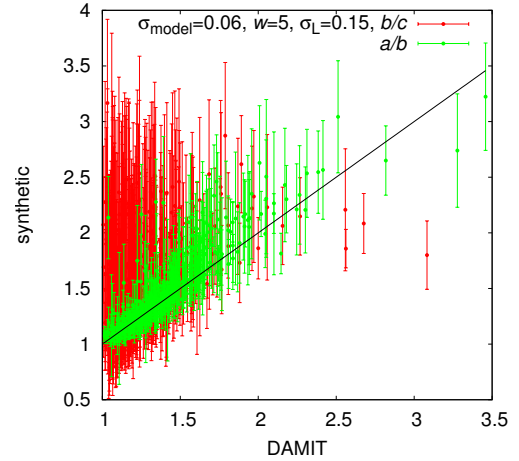
Fig. 11. Comparison of the values of a/b and b/c from DAMIT database with values calculated from synthetic data based on the models from DAMIT. One model was used more than once. The error bars are calculated as the dispersion from the mean value for one model from DAMIT.

4. Distributions of the ratio of axes *a/b*

In this section, we study shapes of asteroids (specifically the ratios of axes a/b and b/c) derived from our model. We tested our model on synthetic data as described above in Sect. 2.1, the assumed noise was 0.15. The values of ratios a/b and b/c obtained with our model are compared with values from DAMIT models derived from the principal moments I_1, I_2, I_3 of the inertia tensor (assuming uniform density),

$$\frac{a}{b} = \sqrt{\frac{I_3 - I_1 + I_2}{I_3 + I_1 - I_2}}, \frac{b}{c} = \sqrt{\frac{I_1 - I_2 + I_3}{I_1 + I_2 - I_3}}. \qquad (18)$$

Since the values of ratios computed from our model were obtained from synthetic data based on DAMIT, they should be the same as values derived from the inertia tensor. The result is shown in Fig. 11. We calculated the linear (Pearson) correlation and Spearman correlation for both ratios, the coefficients ρ are summarized in Table 1. We obtained a good correlation for the ratio a/b, while the ratio b/c is not so well determined.

For the real data, the setup was the same as described in Sect. 3: weight $w = 5$; model noise $\sigma_{model} = 0.06$; and data noise $\sigma_L = 0.07$, respectively, σ_L was calculated according Eq. (17) for asteroids less bright than 80. We compared resulting ratios a/b and b/c of 765 asteroids included in DAMIT with a/b_{DAMIT} and b/c_{DAMIT} and calculated correlation coefficients (see Table 1 and also Fig. 12). The correlation coefficients for the ratio b/c are lower than 0.1, which implies that b/c is not well determined and in following tests we will study only the ratio a/b. The problem to determine the ratio b/c is linked with our previous result that the distribution of ecliptical latitudes β, especially for small bodies (see Fig. 7), shows a preference for high values of β because for a spin axis with high latitude (small obliquity) we have observations only from limited range of polar aspect angles. The determination of b/c, however, requires observations from wide range of aspect angles.

As in Sect. 3.3 we used the bootstrap method to estimate errors of the ratio a/b. The allowed maximum difference among ten calculated values of a/b was 0.25, 3819 remain from 9774 asteroids, and the mean value of the largest differences is 0.18.
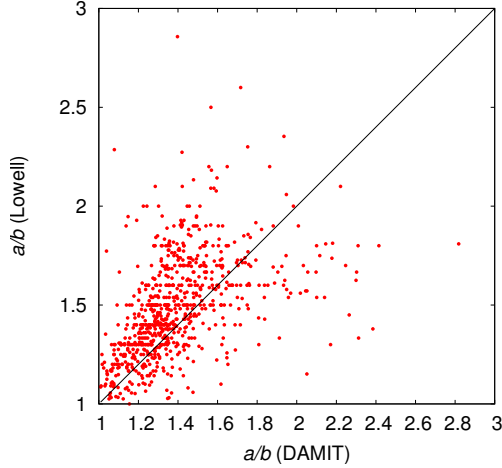
Fig. 12. Comparison of the values of ratio a/b calculated from the real data from the Lowell database with values from DAMIT database.

Table 1. Linear (Pearson) and Spearman coefficients ρ of correlation.

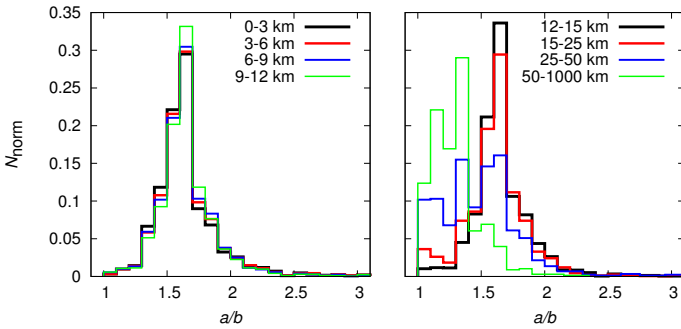|	ρ_{linear}	ρ_{Spearman}
Synthetic data, a/b	0.88	0.91
Synthetic data, b/c	0.35	0.38
Real data, a/b	0.48	0.61
Real data, b/c	0.053	0.088

Fig. 13. Distributions of a/b for groups of asteroids with different sizes (from 0 to 12 km on the *left*; from 12 to 1000 km on the *right*).

4.1. Distributions of a/b for asteroids with different sizes

As in the case of the ecliptic longitude λ, we studied distributions of a/b for several groups of asteroids. The test for asteroids with different diameters showed that larger asteroids ($D > 25$ km) are more spheroidal (values of a/b closer to 1) and smaller asteroids are more elongated ($a/b \sim 1.6$) as is shown in Fig. 13. The differences between distributions in Fig. 13 on the right are much bigger than the uncertainties estimated from bootstrap method 0.18.

This dependence of a/b on D also remained for a smaller sample of 3570 asteroids, which were obtained from the bootstrap method as having well-determined a/b. Since such dependence on diameter can influence the comparison of distributions of a/b of other populations of asteroids, we have to eliminate it in the following tests.

McNeill et al. (2016) determined an average axial ratio for asteroids with diameter $D < 8$ km from PanSTARRS 1 survey as 1:0.85, i.e., $a/b = 1.18$, which is not in agreement with our findings. For the corresponding range of diameters, we calculated the average value of a/b for asteroids in DAMIT (derived from the principal moments of the inertia tensor). The average

value is $a/b_{\text{DAMIT}} = 1.47$, however, the sample of asteroids from DAMIT with $D < 8$ km is biased. The DAMIT sample contains preferentially more elongated asteroids, for which is easier to find the solution of the light curve inversion method. We also checked our result, that larger asteroids are more often spheroidal, against the asteroids in DAMIT; for $D > 50$ km we obtained the average value of $a/b_{\text{DAMIT}} = 1.23$ (our model gives $a/b = 1.29$). We can conclude that the dependence of a/b on diameter is real, however our model gives higher values of a/b for asteroids with $D < 25$ km. Considering the dispersion of values σ_L in Fig. 3, this could be because of the underestimated data noise for smaller and less bright asteroids.

4.2. Different parts of the main belt

Next, we studied distribution of a/b for asteroids with different inclinations of their orbits. To remove the dependence of a/b on diameter, we used only asteroids with $D < 20$ km. The differences between resulting distributions of a/b are not so distinct as when we studied the dependence on diameter, and they are comparable with the uncertainties in a/b.

We also compared distributions of a/b for asteroids with different semimajor axes, specifically inner, middle, pristine, and outer belt, using only asteroids with diameters $D < 20$ km. The differences between distributions of a/b are not significant and are again comparable with the uncertainties in a/b.

4.3. Dynamical families and taxonomic classes

As in Sect. 3.2.4, we compared dynamical families with their backgrounds, using again only asteroids with $D < 20$ km. We did not reveal any significant differences between distributions of a/b of families and corresponding backgrounds. Also the comparison of families with each other did not show any differences larger than uncertainties in a/b.

Szabó & Kiss (2008) derived distributions of a/b for eight asteroids families using data from the Sloan Digital Sky Survey (SDSS). However, their distributions are different from ours; they are often bimodal (Figs. 4–6 therein) and the maximum is for $a/b \sim 1.2$ (our distributions have maximum around 1.6). They also suggest a possible dependence on the age of families (old families contain more spheroidal members), but we do not observe that in our distributions. We believe that they used an assumption that could influence the results. First they assumed that the rotational axes of all asteroids are perpendicular to the line of sight. Then they also tested fixed value $\beta = 50°$ for all asteroids.

The last populations of asteroids we compared were different taxonomic classes, specifically C and S types. The result of KS test, $Q_{\text{KS}} = 0.17$, did not show any difference between these two groups.

5. Conclusions

We developed a new method that allows us to determine the orientation of rotational axes and equatorial axes ratio a/b, assuming a triaxial shape model, using sparse data obtained by all sky surveys. The goal of our approach is to provide a distribution function of the solved-for parameters for a large sample of main belt asteroids rather than detailed rotational state of individual objects. A limitation of our method is that it provides, first, longitude λ of the rotation pole in the interval $(0°, 180°)$ only, with values in $(180°, 360°)$ transformed to $(0°, 180°)$ by $\lambda = \lambda - 180°$

rule; and second, absolute value of the ecliptic latitude β, instead of β itself. The latter means that we cannot determine whether the asteroid rotates in a prograde or retrograde sense. Additionally, our model also does not provide rotational period.

We first justified our method by applying it to a synthetic sample of asteroids and also to a known sample of objects with rotational states resolved by more detailed methods that can be found in the DAMIT database. We observed that our method reproduces well the distribution of the ecliptic longitudes and the equatorial axes ratio a/b in a statistical sense. The uncertainties, estimated using the bootstrap method, are $\simeq 30°$ in λ and $\simeq 0.2$ in a/b without systematic effects on the mean value. The determination of ecliptical latitudes β shows bias toward finding preferentially spin axes near the ecliptic pole. Our tests may, however, provide a rough approximation of the bias function.

We then applied our method to 69 053 main belt asteroids for which a suitably rich and good quality set of observations were obtained from the Lowell Observatory database. The main results are as follows:

1. The distribution of λ is nonuniform, with an excess of asteroids with λ values between 60° and 100°. Similarly, there is a deficiency of asteroids with λ values between 130° and 160°. Curiously, our tests revealed a correlation of this nonuniformity with orbital inclination: asteroids with very low-inclination orbits ($\sin I \leq 0.04$) show the effect more significantly than asteroids with higher inclination orbits.
2. While not a primary result from our paper, we also determined distribution of the absolute value of sine of ecliptic latitude $|\sin \beta|$. We confirm previously reported results that asteroids with size $D \leq 25$ km have their pole latitude tightly clustered about the poles of ecliptic. This is due to the YORP effect that makes the pole latitude to approach the extreme values asymptotically.
3. We also found that small main belt asteroids ($D \leq 25$ km) are more elongated, with a median of ratio $a/b \simeq 1.6$, compared to the large asteroids ($D \geq 50$ km), which have a median of ratio $a/b \simeq 1.3$.
4. We also analyzed our results for populations in different asteroid families. As to the λ distribution, they mainly derive from their inclination value of the aforementioned inclination dependence. For instance, the low-inclination families such as Massalia or Themis have the strongest nonuniformity of the λ distribution in our results.

Using a more detailed method, we confirmed the previously reported unexpected nonuniformity in distribution of ecliptic longitude of spin axes of the main belt asteroids. We tested various hypotheses of its origin, but we had to reject them, proving that the proposed processes would not lead to a significant enough nonuniformity. Therefore, this result remains enigmatic and requires further analysis. In particular, it would be very useful if more detailed methods of spin state and shape inversion from astronomical data confirmed this result and provided more details. We note, for instance, that methods both in Bowell et al. (2014) and here are not able to discriminate between the prograde- and retrograde-rotating asteroids. It would be important to see, if the excess in λ values at about 80° concerns equally well both classes, or whether it is preferentially associated with one of them. This could hint about the underlying processes that cause the effect. In the same way, all methods used so far fold the whole range of ecliptic λ values to a restricted interval $(0°, 180°)$. This

is because of their intrinsic drawback of not distinguishing data for λ and $\lambda + 180°$ cases. Yet, breaking this uncertainty may also help to disentangle the underlying physical causes of the nonuniformity.

Justifications of reliability of our method, by running blind tests against synthetic populations of asteroids and limited datasets for which complete models are already available, make our method a solid tool for further studies. It would be interesting to apply it to more accurate photometric data provided by Large Synoptic Survey Telescope (LSST).

References

Bowell, E., Oszkiewicz, D. A., Wasserman, L. H., et al. 2014, Meteor. Planet. Sci., 49, 95
Brož, M., Morbidelli, A., Bottke, W. F., et al. 2013, A&A, 551, A117
Colombo, G. 1966, AJ, 71, 891
Connelly, R., & Ostro, S. J. 1984, NASA STI/Recon Technical Report A, 85, 87
Davis, D. R., Weidenschilling, S. J., Farinella, P., Paolicchi, P., & Binzel, R. P. 1989, in Asteroids II, eds. R. P. Binzel, T. Gehrels, & M. S. Matthews, 805
Davison, A. C., & Hinkley, D. V. 1997, Boostrap methods and their applications (New York: Cambridge University Press)
Ďurech, J., Grav, T., Jedicke, R., Denneau, L., & Kaasalainen, M. 2005, Earth Moon Planets, 97, 179
Ďurech, J., Scheirich, P., Kaasalainen, M., et al. 2007, in IAU Symp. 236, eds. G. B. Valsecchi, D. Vokrouhlický, & A. Milani, 191
Ďurech, J., Kaasalainen, M., Warner, B. D., et al. 2009, A&A, 493, 291
Ďurech, J., Sidorin, V., & Kaasalainen, M. 2010, A&A, 513, A46
Ďurech, J., Hanuš, J., & Vančo, R. 2015, Astron. Comput., 13, 80
Ďurech, J., Hanuš, J., Oszkiewicz, D., & Vančo, R. 2016, A&A, 587, A48
Hanuš, J., Ďurech, J., Brož, M., et al. 2011, A&A, 530, A134
Hanuš, J., Ďurech, J., Brož, M., et al. 2013, A&A, 551, A67
Hanuš, J., Ďurech, J., Oszkiewicz, D. A., et al. 2016, A&A, 586, A108
Hapke, B. 1981, J. Geophys. Res., 86, 4571
Hapke, B. 1993, Theory of reflectance and emittance spectroscopy (UK: Cambridge University Press)
Henrard, J., & Murigande, C. 1987, Celest. Mech., 40, 345
JeongAhn, Y., & Malhotra, R. 2014, Icarus, 229, 236
Kaasalainen, M. 2004, A&A, 422, L39
Kaasalainen, M., & Torppa, J. 2001, Icarus, 153, 24
Kaasalainen, M., Torppa, J., & Muinonen, K. 2001, Icarus, 153, 37
Knežević, Z., & Milani, A. 2003, A&A, 403, 1165
Kryszczyńska, A., La Spina, A., Paolicchi, P., et al. 2007, Icarus, 192, 223
Magnusson, P. 1986, Icarus, 68, 1
Marciniak, A., Pilcher, F., Oszkiewicz, D., et al. 2015, Planet. Space Sci., 118, 256
Masiero, J. R., Mainzer, A. K., Grav, T., et al. 2011, ApJ, 741, 68
McNeill, A., Fitzsimmons, A., Jedicke, R., et al. 2016, MNRAS, 459, 2964
Nesvorný, D., Brož, M., & Carruba, V. 2015, Identification and Dynamical Properties of Asteroid Families, eds. P. Michel, F. E. DeMeo, & W. F. Bottke, 297
Oszkiewicz, D. A., Muinonen, K., Bowell, E., et al. 2011, J. Quant. Spectr. Rad. Transf., 112, 1919
Pravec, P., & Harris, A. W. 2000, Icarus, 148, 12
Pravec, P., Harris, A. W., & Michalowski, T. 2002, in Asteroids III (Tucson: Univ. Arizona Press), 113
Rubincam, D. P. 2000, Icarus, 148, 2
Santana-Ros, T., Bartczak, P., Michałowski, T., Tanga, P., & Cellino, A. 2015, MNRAS, 450, 333
Skoglöv, E., & Erikson, A. 2002, Icarus, 160, 24
Slivan, S. M. 2002, Nature, 419, 49
Slivan, S. M., Binzel, R. P., Crespo da Silva, L. D., et al. 2003, Icarus, 162, 285
Szabó, G. M., & Kiss, L. L. 2008, Icarus, 196, 135
Vokrouhlický, D., Nesvorný, D., & Bottke, W. F. 2003, Nature, 425, 147
Vokrouhlický, D., Nesvorný, D., & Bottke, W. F. 2006, Icarus, 184, 1
Vraštil, J., & Vokrouhlický, D. 2015, A&A, 579, A14
Warner, B. D., Harris, A. W., & Pravec, P. 2009, Icarus, 202, 134

Abbreviations

A – amplitude
α – solar phase angle
AstOrb – The Asteroid Orbital Elements Database
β – ecliptical latitude of the spin axis
$\beta^\star$ – pole co-latitude
CDF – cumulative distribution function
D – diameter
DAMIT – Database of Asteroid Models from Inversion Techniques
DF – distribution function
ϵ – obliquity
η – dispersion of squared brightness
KS – Kolmogorov-Smirnov
λ – ecliptical longitude of the spin axis
L – brightness
LCDB – The Asteroid Lightcurve Database
LEADER – Latitudes and Elongations of Asteroid Distributions
 Estimated Rapidly
LONEOS – Lowell Observatory Near-Earth Object Search
LSST – Large Synoptic Survey Telescope
MBAs – main-belt asteroids
MMR – mean motion resonance
NEAs – near-Earth asteroids
Ω – longitude of ascending node
P – rotation period
Pan-STARRS – Panoramic Survey Telescope & Rapid Response System
Q_{KS} – probability that two distributions belong to the same parent distribution
ρ – density
σ – noise
SDSS – Sloan Digital Sky Survey
SFD – size-frequency distribution
WISE – Wide-field Infrared Survey Explorer
YORP – Yarkovsky-O'Keefe-Radzievskii-Paddack